Optothermal Microfluidics

Franz M. Weinert

Dissertation

Munich 2009

Optothermal Microfluidics

Franz M. Weinert

Dissertation

submitted by
Franz Michael Weinert
from
Munich

Written at the
Ludwig-Maximilians-Universität München
Systems Biophysics
at
Prof. Dr. Dieter Braun

Munich 2009

First referee:	Prof. Dr. Dieter Braun
Second referee:	Prof. Dr. Joachim Rädler
Date of the defense:	July 21st, 2009

Table of Contents

I. Summary

The cell is the structural and functional unit of all known living organisms. The inside of cells consists of an aqueous solution, containing all kind of interacting molecules and complex molecular machineries. Precise methods to control properties of fluids, like flow fields or the concentration of solutes would be a powerful tool for the controlled manipulation and investigation of cellular processes.

A prominent technical example for a fluidic system is the so-called Lab-on-a-chip technology (Fig. 1). These microchips miniaturize chemical or biological analyses down to a few millimeters to obtain fast results with only little amount of substrates. A major advantage is the possibility to perform multi parallel analyses [1,2]. But controlling fluids at these small scales is a difficult task. Fluid flow is laminar and the implementation of valves, mixing fluids and driving the flow require complex chip designs and need many connections to external macroscopic pumps.

In this thesis, I will present a new approach to drive and control fluid flow in such small systems (See chapter II. Light Driven Microfluidics). Instead of applying pressure from outside in order to generate the flow, it is locally induced by a focused laser. This method allows to control fluid flows in closed compartments like vesicles or living cells.

Fluid flows transport solved particles together with the surrounding liquid. To move solved particles and molecules relative to the surrounding fluid, temperature gradients can be used. This effect is called Thermophoresis or Ludwig-Soret effect. Although this effect has been understood in gases for more than 100 years [3,4], their microscopic origin in aqueous solution is still under debate [5,6]. The observation and investigation of particle-particle interactions, an interesting side effect of thermophoresis, should shed light into this debate (See chapter III. Slip Flow in Thermophoresis).

Thermophoresis moves micrometer sized particles. However, this effect is weak for small molecules. Currently used methods like Optical Tweezers [7,8,9] require prohibitively large optical powers to trap objects much smaller than 100 nm [10]. In the last part of my thesis I will present a method to trap (or likewise concentrate) particles down to the size of small DNA molecules solely by optical means by combining the thermo-viscous fluid pump with thermophoresis (See chapter IV. An Optical Conveyor for Molecules).

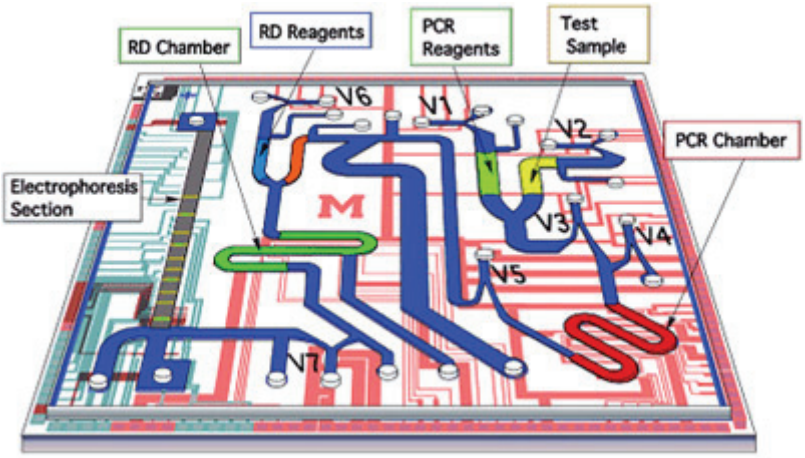

Figure 1: Simplified sketch of a Lab-on-a-chip device. Controlling the fluid flow and mixing fluids typically requires much more complexity of both, the chip design and the interfacing to external pumps.

II. Light Driven Microfluidics

Basic Priciple

Heat propagation is a diffusive process and relaxation times decrease quadratically with the spacial dimension of the system. This implies two properties which plays an important role in all projects:

I. The size of spacial temperature changes can be reduced down to the size of the system.

II. Temperature oscillations can be performed very fast.

In all projects I present in this thesis, we use a laser to generate temperature changes in micrometer thin water layers (Fig. 2a). In these systems we can generate temperature spots with the diameter of only a few micrometers and we can change temperature with rates faster than 10 kHz. When the heating laser spot is moved through the layer, the water in the wake of the spot cools down very fast. For moderate velocities, the result is a moving warm spot. Consider this spot is moving towards the left (Fig. 2b). The water in front of the spot heats up while the water in the wake of the spot cools down to ambient temperature again. The resulting density changes of the water lead to divergent flows due to mass conservation [11]. In front of the spot the water expands, while in the wake it contracts again. At constant viscosity the system is symmetric and the contraction exactly cancel out the previous expansion. However, including the temperature dependence of the viscosity breaks the symmetry. A lower viscosity at higher temperatures for example increases the velocities in the warm spot between the expansion and contraction (see bottom of Fig 2b). Result is a net flow against the spot direction. When the spot passed over once, the net shift of the water after

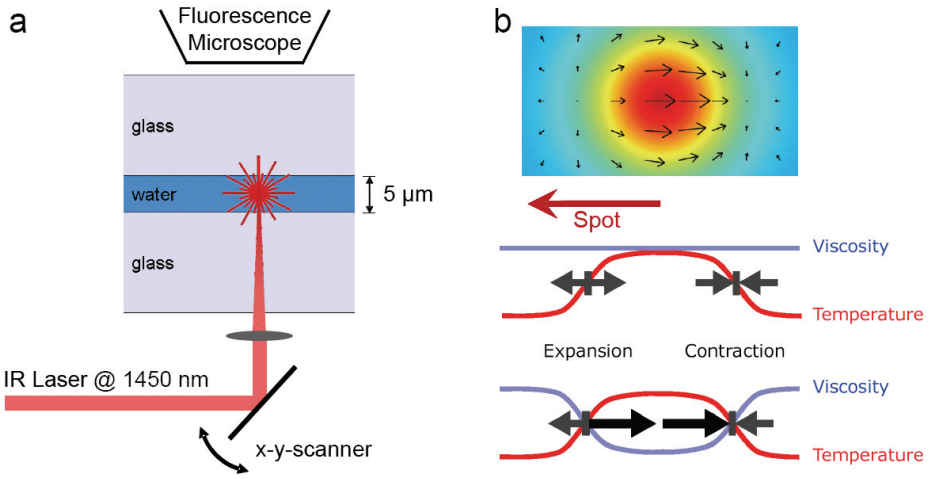

Figure 2: (a) Schematic view of the experimental setup. An infrared laser is deflected by a Acousto-Optical Deflector and focused into a thin water layer between two glass windows. The water absorbs a part of the light. Result is a spot of raised temperature localized at the optical focus of the laser. (b) Moving the warm spot generates local fluid flows due to density changes of the water. The water expands in the front of the spot and contract again in the wake. At constant viscosity both movements cancel out one another. However, a lower viscosity in the warm spot increases the velocities inside the warm spot. Result is a net flow against the spot direction.

expansion and successive contraction is in the tens of nanometer scale. However, the laser movement can be repeated in the kHz regime due to the fast thermal coupling to the close glass windows. Therefore rather fast pump velocities in the order of 100 µm/s can be achieved.

Using the nonlinear effect described here, we can, for example, move water along the letters “LASER PUMP” without lateral walls to guide the flow (Fig. 3). In the example, we sandwich a 10µm thin sheet of water between glass slides and move an infrared laser focus along the letters with a laser scanning microscope. The water is locally heated by direct absorption of the laser irradiation. The spot movement along the letters is repeated in the kilohertz regime. As a result, the fluid flows the reverse path of the warm spot movement.

Finite Element Simulations and Theory

To test this model, a finite element simulation of the three dimensional Navier-Stokes equation was performed (Fig. 4a). The system of interest allows to do a set of approximations. We can for example assume the flow to be laminar and therefore neglect the inertia terms. Furthermore dimensions parallel to the surface are much greater than the width of the water layer, which allows to do a thin film approximation and describe the system as a two-dimensional flow (Fig. 4b). By further approximation, which were tested by the finite element simulations (for details see VII.4), it was possible to obtain an analytical formula, which describe the pump velocity under a set of parameters:

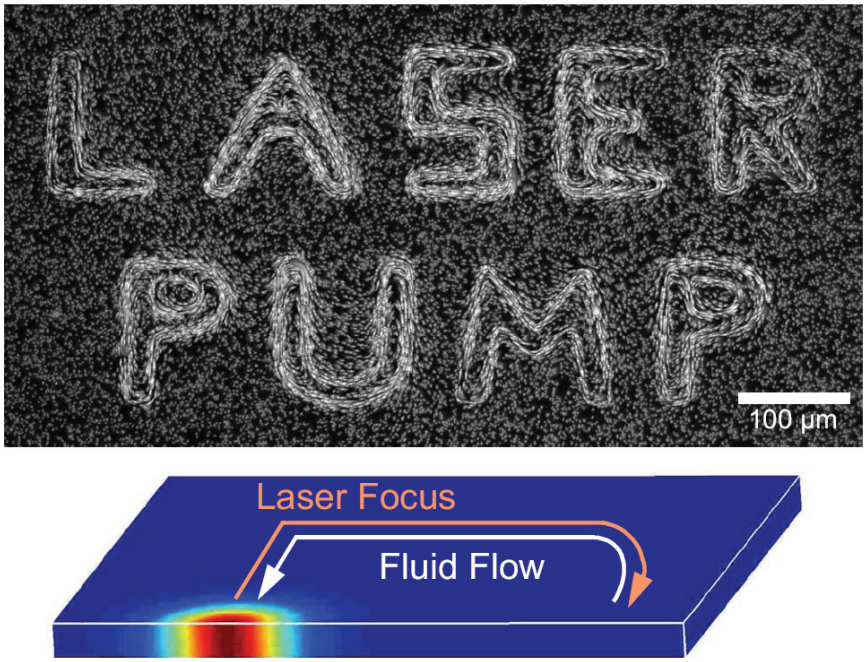

Figure 3: Pumping water optically along arbitrary patterns. Fluid flow along the letters "LASER PUMP" is driven by dynamically heating a thin fluid film with a laser scanning microscope. As seen, complex flow patterns are easily accomplished. No channels restrict the fluid flow. Local pumping of the fluid film is the result of thermoviscous fluid movements for each passage of the laser focus. We visualize the water flow by fluorescent tracer particles.

$$v_{\text{pump}} = -\frac{3\sqrt{\pi}}{4} f \alpha \beta b \Delta T^2 , \qquad (1)$$

where f is the repetition frequency of the laser, α is the expansion coefficient, β is the temperature dependence of the viscosity and ΔT is the amplitude of the temperature spot. The temperature can can be obtained by imaging a temperature sensitive fluorescent dye solved in the water. The shape of the moving warm spot is measured by stroboscopic illumination with a LED with a 10 µs long rectangular light pulse each time the laser spot passes by.

Experimentally we can measure all of the parameters shown in (1) and compare the theoretical formula with measured pump velocities. We have argued that every passage of the warm spot results in a liquid step Δx opposite to the spot movement direction. The pump speed is therefore expected to increase in a linear fashion with repetition frequency of the laser spot as given by equation (1). This behavior was predicted by the theory and verified by measurements in the low frequency regime $f \ll 1\,\text{kHz}$ as shown in the inset of figure 5a. The repetition rate f in this experiment was adjusted by moving the laser spot with increased velocity along a fixed circular pump geometry. For slow frequencies, the spot temperature distribution remains in its Gaussian shape. A further increase in the spot velocity results in a considerable elongated temperature spot geometry along the pump direction which enhanced

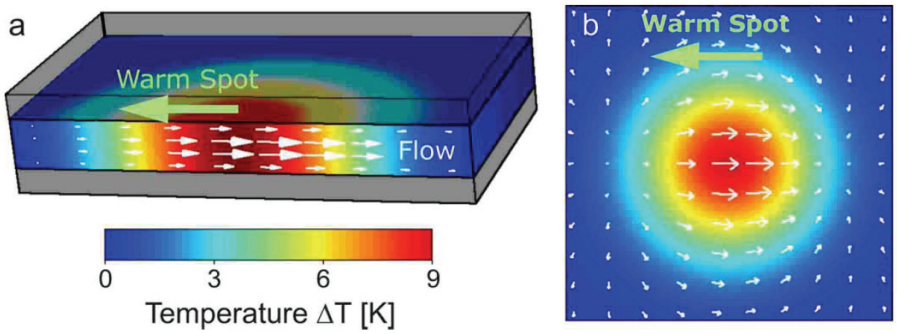

Figure 4: Finite Element Simulation of the Navier-Stokes equation in reference of the moving spot. (a) Three dimensional calculation. (b) The model can be reduced to 2 dimensions by making a thin film approximation.

the pump speed beyond the linear estimate using constant spot width b (Fig. 5a). Examples of spot geometries as measured with stroboscopic temperature imaging are given as color coded insets. Interestingly, the nonlinear pump velocity could still be described when the elongated temperature spot geometry was taken into account with a spatial integral of equation (1) for each repetition rate (Fig. 5a, solid line).

The analytical theory predicts a linear response of the pump velocity to both the thermal expansion $\alpha \Delta T_0$ and the change in the temperature dependent viscosity $\beta \Delta T_0$ for a similar shape of the temperature spot. If the spot temperature is enhanced by higher laser power, the pump velocity increases proportionally to ΔT_0^2. The experiments fully confirmed this parabolic dependence as shown in figure 5b. The solid line results from equation (1) without additional fitting parameters and matches the experimental data within the error bars.

We test the proportionality to the parameters α and β by changing the ambient temperature T_{ch} of the chamber. In figure 5c we changed T_{ch} by cooling the microscope stage with an external heat bath. The experiments reveal a reversal of the pump direction at fluid temperatures below 4 °C. We attribute this reversal to the sign change of the volume expansion coefficient α. The theoretical expectation of equation (1) again fits the experimental pump velocities as plotted against the fluid temperature within the experimental errors.

Microfluidics using Gels

While the dynamic control of fluid flow on the micrometer scale is an interesting subject by itself, the capability to transport dissolved molecules is crucial for microfluidic applications. Traditional microfluidics use micromachined channels to hinder diffusion of molecules perpendicular to the pump direction. While our technique can also pump along such optically transparent channels, we aim at more flexible and previously impossible settings. For example, the method allows the usage of unstructured and disposable chambers. To show that

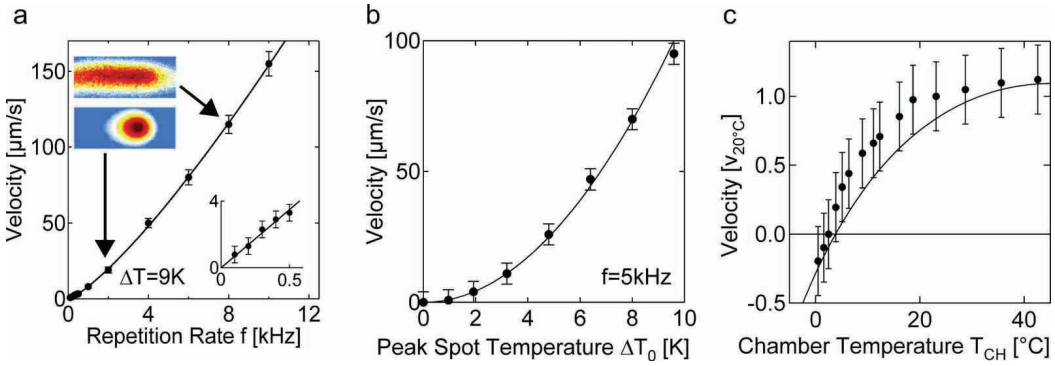

Figure 5: Testing and comparing the analytical formula with measured pump velocities. (a) The pump velocity is a linear function of the repetition rate for f=1 kHz when the spot geometry remains Gaussian. (inset: temperature image). At faster rates, the warm spot becomes elongated due to the finite thermal equilibration time of cooling. Accordingly, the pump velocity is enhanced beyond the linear prediction as the spot width b increases from 10 to 20 µm in the 5 µm thin fluid film. The solid line predicts the pump velocities based on extrapolated temperature profiles for each repetition rate f. (b) The pump velocity rises with the square of the spot temperature, confirming the linear dependence on both the thermal expansion and the temperature dependence of the viscosity (Fig. 5b). Pump velocities are predicted by Eq. (1) without fitting parameters at a spot width b=25 µm. (c) By changing the overall chamber temperature T_{ch}, we can probe the dependence on $\alpha(T_{ch})$ and $\beta(T_{ch})$. For $T_{CH}<4\,°C$, the water contracts upon heating. As expected from Eq. (1), pump velocity reverses its direction (solid line). In all plots, error bars show standard errors from particle tracking.

light driven pumping can be used in microfluidic applications, we demonstrate a purely light driven fluid mixer for small biomolecules.

The initial condition is prepared by sandwiching two droplets containing initially warm low melting temperature agarose gel between glass slides. One droplet additionally contains a fluorescent labeled biomolecule (Fig. 6). The fluorescent molecules are pumped into three pockets of different areas and mixed with the surrounding dark liquid with volume ratios of 4:1, 1:1 and 1:4.

Light Driven Microfluidics in Ice

While this approach works well for particles or long bio-molecules, small molecules can still diffuse through the gel and can not be confined by the channels. In the following we will show that ice sheets can be used instead of gels to hinder diffusion. The infrared laser could be used to melt liquid channels into the ice. This system becomes even more interesting, when not the whole channel is molten at once and freezes again behind the heating laser spot. By repeating the laser spot movement with high frequencies, the water undergoes a series of melting and freezing circles. Here considerably faster pump velocities can be archived.

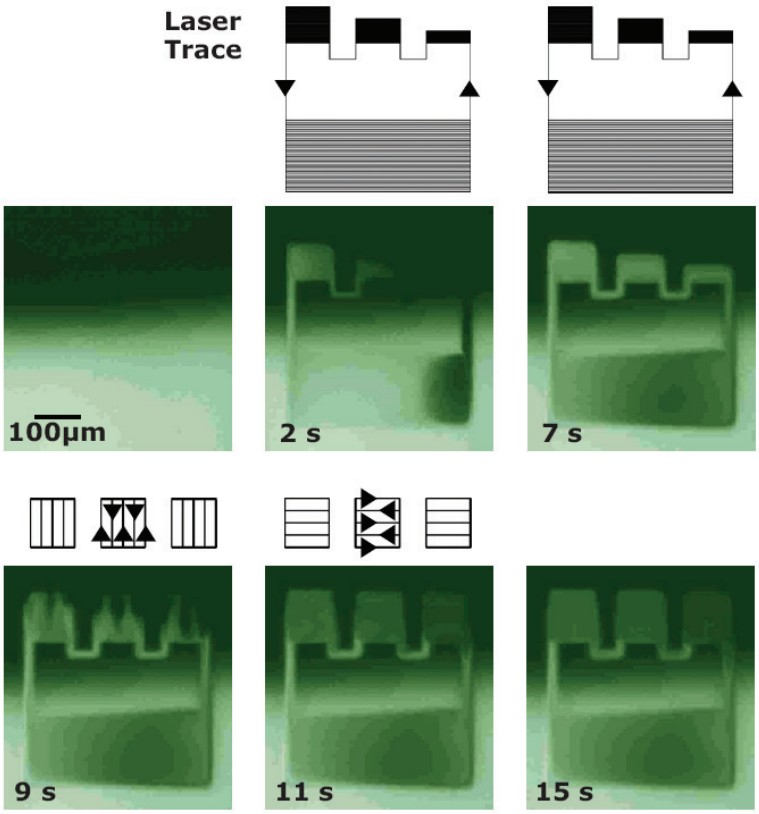

Figure 6: Fast light driven creation of a dilution series. Biomolecules are aliquoted and mixed from an interface of two neighboring gels. First, three volumes of 65, 40, and 20 pl are created. In a second step the fluid is mixed by repeatedly pumping rectangular ring flows with perpendicular orientation. The result is a dilution series with volume ratios of 4:1, 1:1, and 1:4 in equal volumes.

Consider a spot of enhanced temperature moving through a thin ice sheet (Fig. 7). The ice thaws at the front of the spot and freezes in its wake. The density change during the phase transition induces divergent flows due to mass conservation, with a sink ($\mathrm{div}\,\boldsymbol{v} > 0$) at the front and a source ($\mathrm{div}\,\boldsymbol{v} < 0$) at the back. The solid ice boundaries confine the liquid flow such that movement is from the back of the molten spot to its front. We assume a parabolic flow profile perpendicular to the glass/silicon boundaries with $v_{avg} = 2/3\, v_{\mathrm{water}}$, where v_{water} is the peak velocity in the center of the fluid sheet. The continuity equation $\dot{\rho} + \mathrm{div}\,\boldsymbol{j} = 0$ at the water-ice boundary is given by

$$\frac{\rho_{\mathrm{water}} - \rho_{\mathrm{ice}}}{\Delta t_M} - \frac{2}{3}\frac{v_{\mathrm{water}}\,\rho_{\mathrm{water}}}{\Delta x_M} = 0\,. \tag{2}$$

With the velocity of the water-ice boundary $v_{\mathrm{spot}} = \Delta x_M / \Delta t_M$ we find

$$v_{\mathrm{water}} = \frac{3}{2}\frac{\rho_{\mathrm{water}} - \rho_{\mathrm{ice}}}{\rho_{\mathrm{water}}} v_{\mathrm{spot}}\,. \tag{3}$$

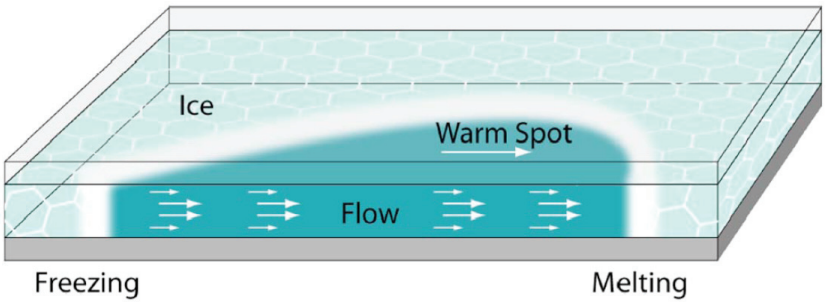

Figure 7: An optically created temperature spot is moved to the right in a sheet of ice. The ice melts in front of the spot (right) and freezes behind it (left) and moves the fluid due to the difference in specific volume.

The water is molten during the passage of the spot for the time interval $\Delta t = d_{\text{spot}}/v_{\text{spot}}$, where d_{spot} is the end to end distance of the molten area and moves by the distance $\Delta x = v_{\text{water}} \Delta t$. If the spot movement is repeated with frequency f, we expect a pump velocity

$$v_{\text{pump}} = \Delta x \; f = \frac{3}{2} \frac{\rho_{\text{water}} - \rho_{\text{ice}}}{\rho_{\text{water}}} d_{\text{spot}} f . \qquad (4)$$

It is possible to image the length of the moving spot d_{spot} by stroboscopic white light imaging. A typical image of the drop-shaped molten area with $d_{\text{spot}} = 120\,\mu\text{m}$ is shown in figure 8d. Pumping is performed with a repetition rate of $f = 650\,\text{Hz}$ and a chamber temperature of $T_0 = -10\,°\text{C}$. With densities $\rho_{\text{water}} = 1000\,\text{kg/m}^3$ and $\rho_{ice} = 917\,\text{kg/m}^3$ we expect $v_{\text{pump}} = 9.5\,\text{mm/s}$. Experimentally, we find $11\,\text{mm/s}$, which is inferred from tracer particles with 1 µm diameter, in agreement with the theoretical expectations.

The length of the molten spot depends on the temperature of the ice sheet (Fig. 8c). At low ice temperatures, only a short spot is molten. At higher ice temperatures, the molten spot can reach lengths beyond $500\,\mu\text{m}$ with the pump velocity exceeding $50\,\text{mm/s}$ (Fig. 8a). We inserted the spot lengths into equation (4), shown as a solid line in figure 8a. Theory and experiment match quantitatively. For further increased chamber temperatures, the front of the thawed spot catches up with the back of the previous heating cycle. The fluid flow is not confined solely toward the front in this case and pumping stalls. A residual negative pump velocity is attributed to the previously shown thermoviscous flow in liquids and matches theoretical predictions with a temperature spot width of $b = 60\,\mu\text{m}$ and a temperature raise of $\Delta T = 15\text{K}$ given by equation (1).

We expect that the repetitive melting-freezing cycles are not very stressful to biomolecules since ice, if cooled on the millisecond time scale, remains amorphous and without grain boundaries.

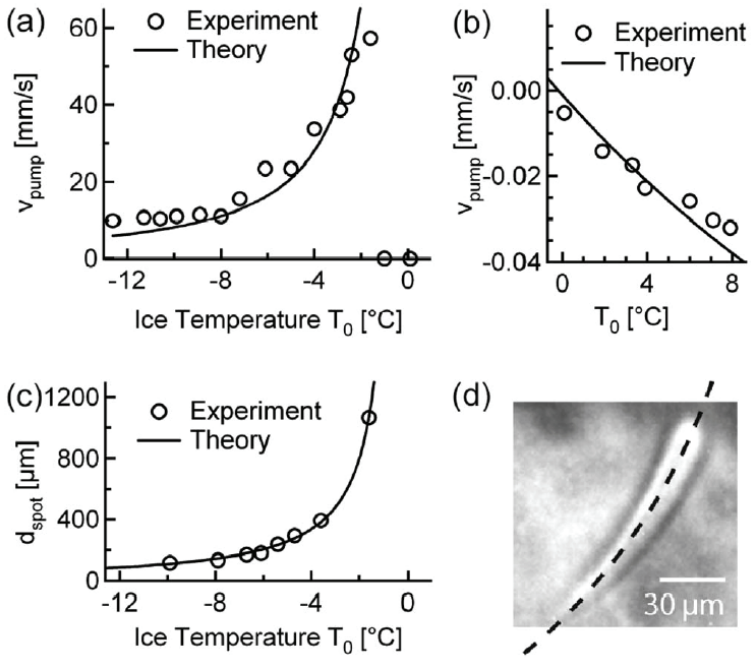

Figure 8: (a) Pump velocities depend on the ice temperature T_0 (open circles). Equation (4) predicts the pump velocity. (b) When the fluid does not freeze along the channel, the residual negative pump velocities can be described by the theory of thermoviscous flow (Eq. (1)). (c) The length of the thawed spot becomes more elongated for higher T_0. (d) Stroboscopic image of the molten spot along a circular path, shown by the broken line.

III. Slip Flow in Thermophoresis

By controlling the laminar movement of the liquid, it is only possible to transport particles together with the containing liquid to different places. The particle stays still in respect to the surrounding liquid. At best diffusion can be reduced using fluids with high viscosity or solid boundaries. However, there are several possibilities to move particles relative to the surrounding fluid. Electric fields, optical pressure or inertia forces could for example be used to move or concentrate solved particles.

Thermophoresis

Most particles tend to move along temperature gradients. This effect is called thermophoresis, the Soret effect or thermodiffusion. For diluted concentrations, it is generally assumed [12] that the thermodiffusive drift velocity $\vec{v}$ depends linearly on the temperature gradient ∇T with a proportionality constant which equals the thermodiffusion coefficient D_T: $v = -D_T \nabla T$. In steady state, thermodiffusion is balanced by ordinary diffusion. Constant diffusion and thermodiffusion coefficients both lead to an exponential depletion law [13] $c/c_0 = \exp[-(D_T/D)(T-T_0)]$, with the concentration c depending on the

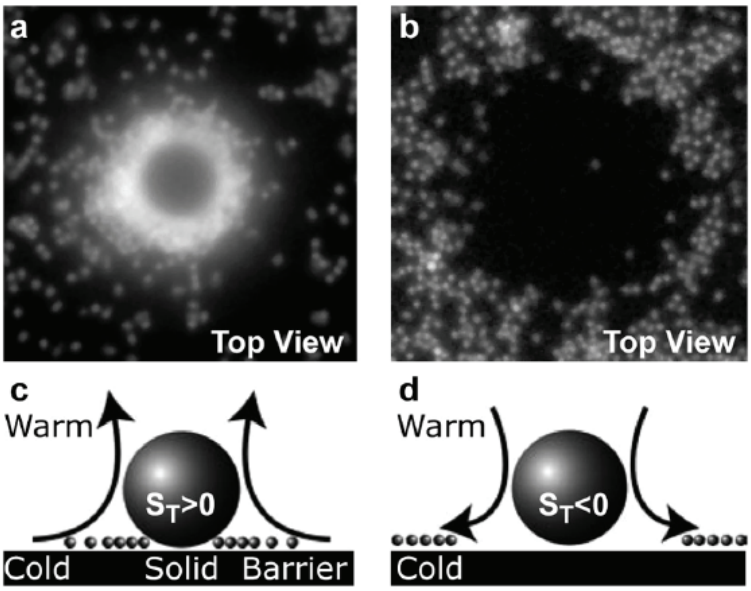

Figure 9: The slip flow induced by a temperature gradient across particles with a diameter of 10 µm attracts or repels tracer particles of diameter 0.5 µm. The direction of the flow depends on the sign of the Soret coefficient of the large particle. (a) Polystyrene beads with $S_T>0$ attract the tracer particles. (b) Silica spheres with $S_T<0$ repel them. (c),(d) Schematic side view of the flow induced accumulation (depletion) of the tracer particles.

temperature difference $T-T_0$ only. The concentration c is normalized by the boundary condition of the concentration c_0 with temperature T_0. The Soret coefficient is defined as the ratio $S_T=D_T/D$, which determines the magnitude of thermodiffusion in the steady state.

Although thermodiffusion has been known for a long time [3,4], its theoretical foundation for particles in liquids is the subject of a long-standing debate. Arguments that the movement is the result of local equilibration driven by the thermal fluctuations of the particles [5,6,13,14,15,16] seem to contradict a proposed Marangoni-like quasislip on the particle surface [17,18,19]. In the following I will show evidence for fluid flow near the surface of particles exposed to a strong temperature gradient.

Observation of Slip Flow

A strong thermal gradient was applied by heating water homogeneously in a thin chamber (10–25 µm) by scanning the infrared laser uniformly across a rectangular area using a moderately focused beam (diameter 80 µm). While the temperature is uniform along the fluid film, a vertical thermal gradient is derived from thermal conductivities of the chamber materials: insulating plastic on top (Heatconductivity $\lambda=0.16\,\mathrm{W/mK}$) and cooling sapphire at the bottom ($\lambda=34\,\mathrm{W/mK}$). Typically, thermal gradients in the range of 0.2 to 0.7 K/µm are generated at the sapphire surface, and the fluid temperature is increased by less than 5 K. The temperature along the z direction is plotted in figure 10b.

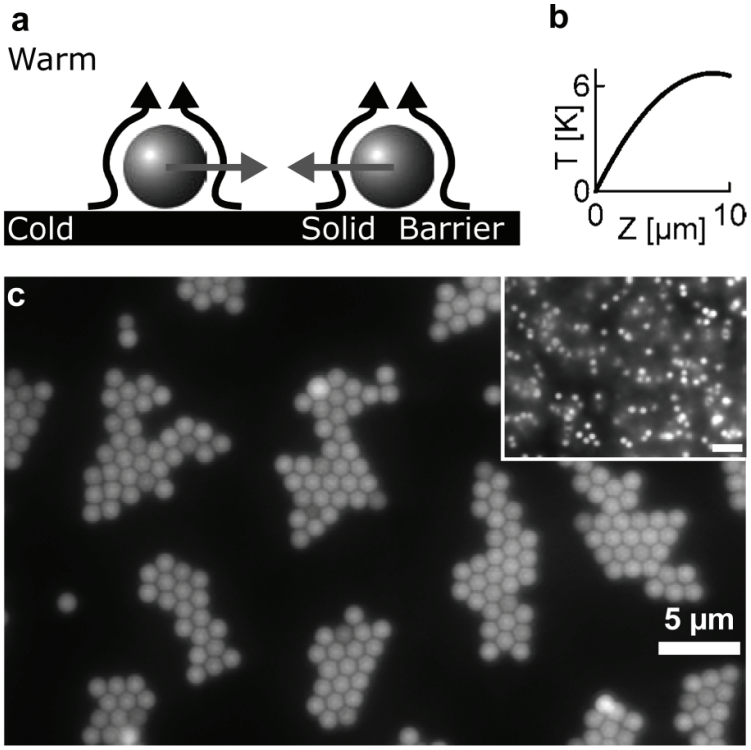

Figure 10: (a) In a strong temperature gradient, particles move ballistically to the cold surface (side view). The persisting slip flow is deflected by the surface and leads to mutual hydrodynamic attraction. (b) Temperature profile. (c) Colloidal crystals of 1 µm polystyrene particles on a cold surface for positive Soret coefficients (view from the top after 20 s of heating). Inset: Before temperature application.

Particles in solution move against the temperature gradient towards the cold for $S_T > 0$ and towards warm temperatures for $S_T < 0$. No movement perpendicular to the gradient is expected. We use this situation to probe the possible fluid flow in the vicinity of larger particles (10 µm diameter) by using small tracer particles (0.5 µm diameter). The big particles were made from either polystyrene or silica which show a positive and negative Soret coefficient under these conditions, respectively.

The tracer particles $(S_T = 8.9\,K^{-1})$ are also subjected to downward thermophoresis in a thermal gradient of $\nabla T = 0.24\,K/\mu m$ in a 25 µm thick chamber (Fig. 9). Tracer particles accumulated near a 10 µm polystyrene particle, where an upward directed slip flow was expected. The tracer particles were depleted from the area around the 10 µm silica particles, which had a negative Soret coefficient, thus indicating a downward slip flow (Figs. 9c and 9d).

Thermophoretic Crystallization

In the above experiment, the 10 µm particles sedimented due to their weight. Smaller particles with a positive Soret coefficient can be moved to the cold surface by the thermal gradient. As

a result of their surface-generated slip flows, the particles subsequently attract one another (Fig. 10a). To probe this, we imaged 1 µm diameter polystyrene particles, which normally experience repulsive interactions with each other. Without thermal gradients, the particles diffused freely with a sedimentation length of $L = kT / F_{pot} = 15\mu m$, where F_{pot} is the gravitational force (Fig. 10c, inset). After switching on a thermal gradient of $0.65\,K/\mu m$ (Fig. 10b), the thermophoretic drift decreased the sedimentation length to below $L = 1/(S_T \nabla T) = 100nm$. As the particles reached the surface, they were attracted to one another within inter-particle distances of several micrometers and formed two-dimensional crystals (Fig. 10c).

Inter-particle Potential

In a thermal gradient of $0.28\,K/\mu m$, we determined the attractive potential of a particle pair by tracking the inter-particle distance distribution parallel to the surface. Figure 11a shows an image of the isolated 2 µm polystyrene particles, which were tracked ($S_T = 43 K^{-1}$) and found to fluctuate in close proximity. We obtained the potential difference ΔV of the attraction from the Boltzmann distribution. The number of particles ΔN found within the distance interval $[d, d + \Delta d]$ is given by

$$\Delta N(d) = 2\pi d \bar{N} \exp(-\Delta V(d)/kT)\, \Delta d, \qquad (5)$$

with average particle density $\bar{N}$ [20]. Particle distances were recorded over 1300 s and included stochastic binding and unbinding processes of the particle pair. The resulting potential $\Delta V(d)$ from N = 8300 pair distance values is plotted in figure 11b. The potential is shifted to zero potential at a distance of 8 µm. Beyond this distance, we did not obtain enough data to statistically evaluate the shape of the curve. The attraction well reaches a depth of 5 kT.

Slip Flow Model

To compare the measured particle attraction to possible slip flow induced by the temperature gradient, we set up a slip flow model using Marangoni forces. Slip flow can be assumed in the Debye layer close to the surface of the particles [17,18,19]. The Marangoni force tangential to the surface counterbalances the off-diagonal components of the hydrodynamic surface stress [19]. The temperature dependence of the surface energy is set to match the thermophoretic mobility D_T in free solution within the pseudo-slip condition framework.

We carried out a simulation using an industrial finite element solver in 3D. The particle was located above the bottom sapphire at the sedimentation length kT/F with a downward force F from thermophoresis and gravitation. We iteratively adapted the surface slip-flow condition to match the calculated hydrodynamic surface stress. The flow lines and the thermal gradient for a solution with a particle distance of $4.6\mu m$ are depicted in figure 11c. A

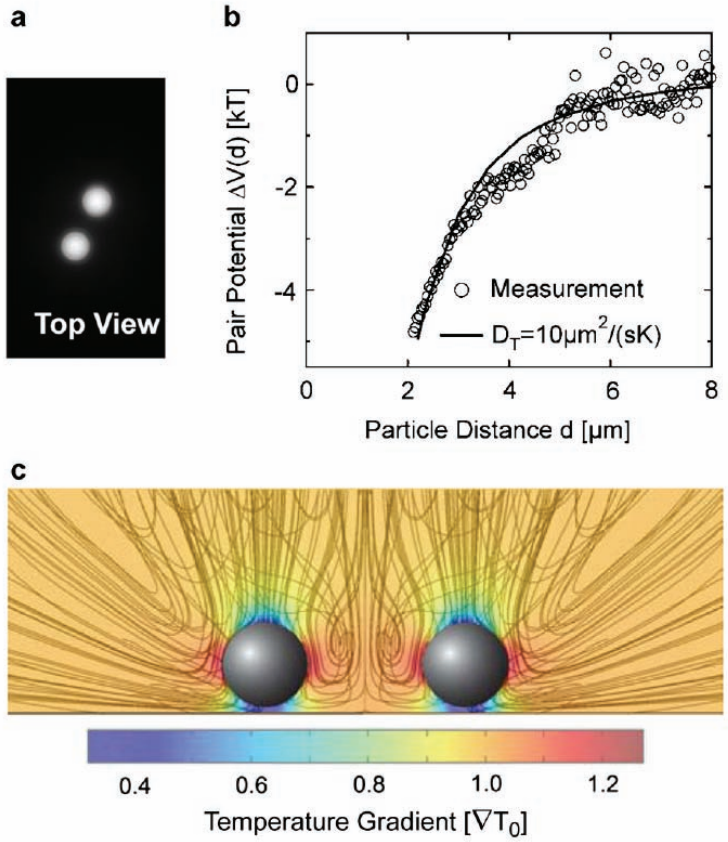

Figure 11: Particle attraction from thermophoretic slip flow. (a),(b) The distance distribution of a single particle pair is measured by particle tracking. The effective pseudo pair potential $\Delta V(d)$ was determined using Boltzmann statistics (open circles) and fits quantitatively to the slip flow model. (c) The three-dimensional flow around the particles was calculated using finite elements. A projection of the flow lines is shown in gray; the thermal gradient is color coded and given in units of the free solution temperature gradient ∇T_0. The calculated pair potential is plotted as a solid line in (b).

simulation of a single particle without nearby surfaces reproduced the temperature dependence of the surface energy to match D_T.

We calculated the total hydrodynamic forces on the surfaces of one particle, which is subjected to the fluid flow, induced by a second particle. By integrating the forces in direction of the second particle for a set of particle distances d, we obtained the pseudopotential of the particle attraction $V(d)$.

Both the experimentally and theoretically obtained pseudo-potentials flatten out into noise levels for distances beyond $8\mu m$. As shown in figure 11b, the calculated pseudo-potential fits the experimentally determined potential in ample detail without fitting parameters. Thus the particle attraction can be quantitatively understood based on the hydrodynamic interaction induced by thermophoretic slip flows.

Slip flow can only be observed in the regime of

$$S_T \, a \nabla T > 1 \,, \tag{6}$$

where the particle's energy vary by more than 1 kT for a translation of his own diameter along the temperature gradient. For weaker gradients, the particles are not located at the cold surface and no inter-particle attraction is found.

Particle attraction is not expected from a thermodynamic viewpoint of thermophoresis, since no sufficient thermal gradients parallel to the surface exist. However, the finding of slip flow in thermophoresis does not contradict an explanation of thermophoresis by a thermodynamic model since the local equilibrium is expected to break down when the thermal gradient reach the condition of equation (6) [5,13,14].

IV. An Optical Conveyor for Molecules

Large particles with sizes in the micrometer scale can be trapped by structuring steady temperature patterns. For moderate temperatures the influence on smaller particles towards the size of molecules becomes small compared to their thermal fluctuations.

In the following chapter I will show that the thermophoretic accumulation can be amplified by combining thermophoresis and perpendicular liquid flows. This method allows to trap even small DNA molecules in solution.

Basic Principle

The principle is based on a bidirectional flow of the fluid perpendicular to a thermal gradient [21,22]. As a result, the molecules are pushed by thermophoresis into one side of the flow and are transported preferentially in one direction. Applied to an axially symmetric geometry, freely diffusing molecules in a fluid film are expected to accumulate to a single spot from all directions (Fig. 12a). In effect, thermophoresis pushes the molecules upward where the water flow shuttles them to the center.

Interestingly, this intricate situation of counterflow and thermal gradient can be created solely by optical means. The thermal gradient is applied by focused infrared absorption of a Cr-film below the water (Fig. 12b). The bidirectional flow is generated by a moving laser spot, based on the shown thermo-viscous fluid pump which uses thermal expansion in thermally created viscosity gradients. We impose an outward flow near the bottom warm side by a radial laser pattern. The counterflow at the top is ensured by mass conservation.

Trapping DNA

This situation allows the generation of a bidirectional flow in very thin fluid layers of only 2 µm. With a mean temperature difference of 15 K and a diameter of 200 µm this conveyor belt becomes very efficient even for small polymers with lengths down to 1.5 nm. Figure 12c

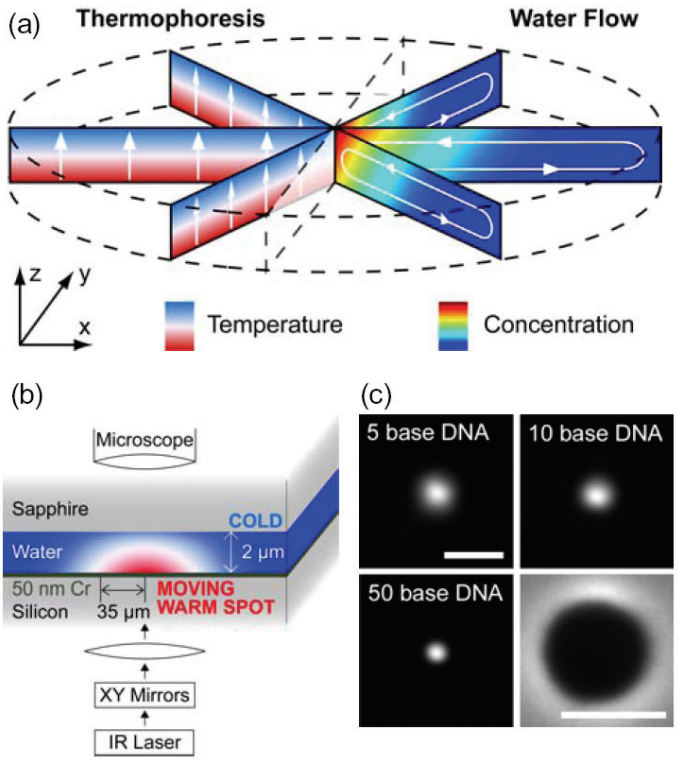

Figure 12: Conveyor trap. (a) Bio-molecules are efficiently accumulated by a combination of a temperature gradient and perpendicular bidirectional flow. Since thermophoresis predominantly locates the molecules at the colder top, the conveyor-like water flow transports the molecules to the center. (b) Both the temperature gradient and the water flow is generated by a spot of enhanced temperature at the bottom, induced by the laser absorption in a thin metal layer. The water flow is the result of the co-axial thermo-viscous pumping in radial direction. (c) Short DNA is trapped from a diameter of 200 µm within 3 seconds. Longer DNA shows a stronger confinement. The single stranded DNA oligos with lengths of 5, 10 and 50 bases are labeled with the fluorescent dye 6-carboxy-2',4,4',5',7,7'-hexachlorofluorescein,succinimidyl ester (HEX) to visualize the concentration. By reversing the fluid flow, the molecules are transported off the conveyor, shown by 1000 base pair DNA stained with the intercalating dye TOTO-1. Scalebars are 100µm.

shows single stranded oligonucleotides with lengths of 5, 10 and 50 bases, trapped within 3 seconds. The longer DNA molecules are accumulated to higher concentrations and are more tightly confined in the center, with an $1/e$ decay at a radius of 14 µm. By inverting the flow, the conveyor transports the molecules equally efficiently in outward direction as shown for 1000 base pair DNA in Figure 12c, 4th image.

Finite Element Simulation

The physics of the conveyor belt can be simulated using finite elements. In an axial symmetric geometry we model a bidirectional flow with a maximal speed $v_{max} = 200\,\mu m/s$ within the trapping region $r < 100\mu m$. We add the thermophoretic drift $v = S_T D \nabla T$ into the diffusion equation with a temperature gradient ∇T matching temperature imaging

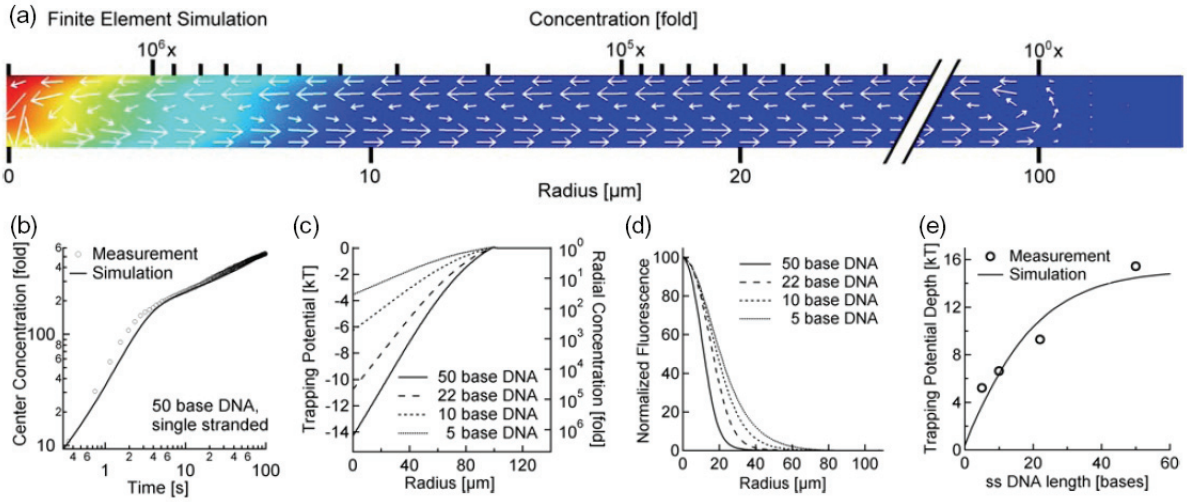

Figure 13: Theory (a) Finite Element Simulation in an axial symmetry confirms the experimental observations and predicts a steady state concentration of 2 million fold for single stranded 50 base DNA. Arrows represent the fluid flow. (b) Molecules in the trap are shuffled to the center within 3 seconds as shown by the time trace of the center concentration with $c \propto t^{1.2}$. The successively slower concentration increase ($c \propto t^{0.4}$) refers to diffusion into the region of the trap. The simulation (solid line) confirms the experimental behavior (open circles) (c) Radial distribution of the simulated trapping potential for 5, 10, 22 and 50 base DNA. (d) Measured concentration distribution of the conveyor belt. (e) Measured trapping potential depths for the DNA oligomers (open circles) match finite element simulations (solid line).

measurements using the temperature sensitive dye Cy5. The optical conveyor is simulated for various DNA lengths. Values for the diffusion coefficient D and the Soret coefficient S_T are phenomenologically interpolated to match measurements. Figure 13a shows the simulated concentration for 50 base DNA (color scale). The simulation predicts a two million fold increase of the center concentration in the steady state.

The trapping mechanism transports the particles into the center within 3 seconds. After that period the relative concentration profile inside the trap is equilibrated. To further increase the absolute value of the center concentration, molecules have to diffuse into the region of the trap. To fill the trap up to its steady state concentration, all molecules within a radius of 10 mm would be needed to enter the trap. Figure 13b shows the measured time trace of the center concentration, compared to the simulation prediction. The two different regimes can be clearly distinguished.

The effective potential depth of the trap can be calculated by assuming a Boltzmann distribution of the DNA molecules in steady state: $U(r) = -kT \ln(c/c_0)$. Figure 13c shows the simulated shapes of the potentials for 50, 22, 10 and 5 base DNA. 5 base DNA is expected to be trapped with a potential of 5 kT referring to a 200-fold accumulation. The linear shaped potential results in an exponential distribution of the concentration over the radius of the trap.

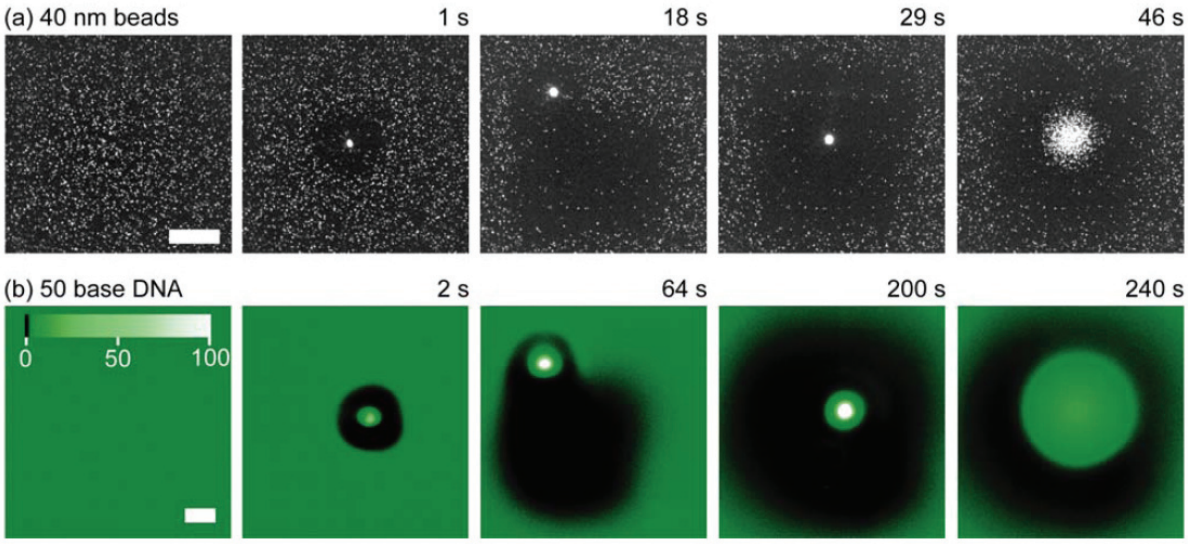

Figure 14: Moving trap. (a) Since the conveyor belt is driven entirely optically, it can be moved arbitrarily through the solution to collect polystyrene beads with a diameter of 40 nm. After the trap has switched off, the particles diffuse freely. (b) The same processing works for single stranded 50 base DNA. The color scale is highly nonlinear to visualize both the high concentration in the trapping center and the comparable low contrast between the outside concentration and the depleted area. The scale bars are 100µm.

The radial fluorescence intensity of trapped DNA molecules is shown in Figure 13d. The intensities are normalized to the center concentration to compare the accumulation efficiency by the confinement of the distribution for different polymer lengths. The concentration profile differs only in the center of the trap from the expected exponential shape. This is explained by the size of the thermal laser spot with a diameter of $d_{1/e}=70\,\mu\mathrm{m}$, which is used to drive the bidirectional fluid flow. In the center the laser spot overlaps and cancels out the flow. This lowers the efficiency of the trap in the center region.

The radial distribution of the measured intensity is fitted with an exponential function in the region beyond $r=10\mu\mathrm{m}$. The trapping potential is obtained from the intensity ratio $U_{\mathrm{TRAP}}/kT=-\ln(c/c_0)=-\ln[I_{\mathrm{EXP}}(0)/I_{\mathrm{FIT}}(100\mu\mathrm{m})]$, where $I_{\mathrm{EXP}}(0)$ is the measured fluorescence intensity in the center. We take the extrapolated intensity at the edge of the trapping region $I_{\mathrm{FIT}}(100\mu\mathrm{m})$ where the fluorescence measurement is limited by background and the dynamic range of the camera. Figure 13e shows the measured potential depths of the molecule conveyor for single stranded DNA molecules of different lengths (open circles). The simulated data (solid line) describes the experimental results quantitatively.

Moving Trap

Since the conveyor belt is driven entirely optically, its position can be changed easily. Instead of waiting for the molecules to diffuse into the trap, they can be collected while passing over them. Figure 14a shows 40 nm polystyrene beads. Comparable to a vacuum cleaner, the radial

conveyor belt collects all particles on the trace. A similar protocol traps 50 base DNA molecules (Fig. 14b).

V. References

1. T. Thorsen, S. J. Maerkl and S. R. Quake, *Microfluidic large-scale integration*, **Science** 298, 580 (2002).

2. H. C. Fan, Y. J. Blumenfeld, U. Chitkara, L. Hudgins and S. R. Quake, *Noninvasive diagnosis of fetal aneuploidy by shotgun sequencing DNA from maternal blood*, **Proc. Natl. Acad. Sci. U.S.A.** 105, 16266 (2008).

3. C. Ludwig, **Sitz.ber. Akad. Wiss. Wien, Math.-Nat.wiss. Kl.** 20, 539 (1856).

4. C. Soret, **Arch. Sci.** 3, 48 (1879).

5. S. Duhr and D. Braun, *Why molecules move along a temperature gradient*, **Proc. Natl. Acad. Sci. U.S.A.** 103, 19678 (2006).

6. M. Braibanti, D. Vigolo and R. Piazza, *Does thermophoretic mobility depend on particle size?*, **Phys. Rev. Lett.** 100, 4 (2008).

7. A. Ashkin, *Acceleration and trapping of particles by radiation pressure*, **Phys. Rev. Lett.** 24, 156 (1970).

8. A. Ashkin, *Optical trapping and manipulation of neutral particles using lasers*, **Proc. Natl. Acad. Sci. U.S.A.** 94, 4853 (1997).

9. S. M. Block, L. S. B. Goldstein and B. J. Schnapp, *Bead movement by single kinesin molecules studied with optical tweezers*, **Nature** 348, 348 (1990).

10. A. Ashkin, J. M. Dziedzic, J. E. Bjorkholm and S. Chu, *Observation of a single-beam gradient force optical trap for dielectric particles* , **Opt. Lett.** 11, 288 (1986).

11. E. Yariv and H. Brenner, *Flow animation by unsteady temperature fields*, **Phys. Fluids** 16, L95 (2004).

12. S. R. de Groot, P. Mazur, **Nonequilibrium Thermodynamics (North–Holland, Amsterdam)** (1969).

13. S. Duhr and D. Braun, *Thermophoretic depletion follows Boltzmann distribution*, **Phys. Rev. Lett.** 96, 168301/1 (2006).

14. R. D. Astumian, *Coupled transport at the nanoscale: The unreasonable effectiveness of equilibrium theory*, **Proc. Natl. Acad. Sci. U.S.A.** 104, 3 (2007).

15. J. K. G. Dhont, *Thermodiffusion of interacting colloids. I. A statistical thermodynamics approach*, **J. Chem. Phys.** 120, 1632 (2004).

16. J. K. G. Dhont, *Thermodiffusion of interacting colloids. II. A microscopic approach*, **J. Chem. Phys.** 120, 1642 (2004).

17. E. Ruckenstein, *Can phoretic motions be treated as interfacial-tension gradient driven phenomena*, **J. Colloid Interface Sci.** 83, 77 (1981).

18. A. Parola and R. Piazza, *Particle thermophoresis in liquids*, **Eur. Phys. J. E** 15, 255 (2004).

19. A. Wurger, *Thermophoresis in colloidal suspensions driven by Marangoni forces*, **Phys. Rev. Lett.** 98, 138301 (2007).

20. D. Rudhardt, C. Bechinger and P. Leiderer, *Direct Measurement of Depletion Potentials in Mixtures of Colloids and Nonionic Polymers*, **Phys. Rev. Lett.** 81, 1330 (1998).

21. D. Braun and A. Libchaber, *Trapping of DNA by thermophoretic depletion and convection*, **Phys. Rev. Lett.** 89, 188103 (2002).

22. S. Duhr and D. Braun, *Optothermal molecule trapping by opposing fluid flow with thermophoretic drift*, **Phys. Rev. Lett.** 97, 038103 (2006).

VI. Acknowledgments

I had a great time during my work at Dieters lab and I did a big step forwards in developing myself. I have not only learned a lot about science but more importantly learned to enjoy doing science. The outcome of my work would not has been possible without all the people who have supported me.

First of all I want to thank Dieter for the close collaboration. He was always available for discussions and came up with a lot of great ideas. Thanks for the intense help writing the publications and for giving me the possibility to visit the all the important conferences.

Ingmar Schön with whom I shared the setup for assistance. Thanks for the chip processing, for the improvements of the setup and organizing workflows in the lab.

Stefan Duhr for all the help and support especially in the beginning of my PhD and during my diploma thesis. We had a lot of fun at all these conferences.

Philip Baaske for lev18 in wc3 and all the fränkische Bier.

Christoph Wienken for frequently accompanying me at the news bar for only one becks.

Christof Mast and Hubert for assistance and the Haribo Kracher.

Max Wühr for doing experiments.

Mario for his patience while sharing the setups.

Philip Reineck for accompanying me during the last weekends in the lab.

Special thanks to Hermann Gaub for supporting me during my work and useful discussions. Thanks for the great environment including all the great food at the Christmas parties and the exciting excursions.

Angelika, Tom, Ralf and Beno for the help in the Chemistry Lab and finding things.

Stefan Stahl, Ferdinand Kühner, Lars, Elias for interesting discussions.

Ann, Katja, Tom for proofreading.

Stefan Kufer, Thomas Bornschlögl, Hendrik Dietz for the great time we spent together and for encouraging me when I was depressed.

Julia and Anna Schmitz, Tom, Stefan for the great Schafkopf evenings.

Katja, Uta, Dominik, Jan, Philip S., Mathias for drinking, discussions, poker, SC, chatting, cooking and having fun.

Thanks to Wolfgang Zinth for discussions and the support.

My parents, brothers, nephews, nieces and Esther for the good time at home and for the financial support.

Thanks to the Tinnefeld group, the Braun group and the Gaub group for the nice working atmosphere.

Thank you all, I owe you so much.

VII. Appendix: Publications

1. P. Baaske, F. M. Weinert, S. Duhr, K. H. Lemke, M. J. Russell and D. Braun, *Extreme accumulation of nucleotides in simulated hydrothermal pore systems*, **Proc. Natl. Acad. Sci. U.S.A.** 104, 9346 (2007)
2. F. M. Weinert and D. Braun, *Observation of Slip Flow in Thermophoresis*, **Phys. Rev. Lett.** 101, 168301 (2008)
3. F. M. Weinert, J. A. Kraus, T. Franosch, and D. Braun, *Microscale Fluid Flow Induced by Thermoviscous Expansion Along a Traveling Wave*, **Phys. Rev. Lett.** 100, 164501 (2008).
4. F. M. Weinert and D. Braun, *Optically driven fluid flow along arbitrary microscale patterns using thermoviscous expansion*, **J. Appl. Phys.** 104, 104701 (2008)
5. F. M. Weinert, M. Wühr and D. Braun, *Light driven microflow in ice*, **Appl. Phys. Lett.** 94, 113901 (2009)
6. F. M. Weinert and D. Braun, *An optical conveyor for molecules*, submitted to Science June 19, 2009

Extreme accumulation of nucleotides in simulated hydrothermal pore systems

Philipp Baaske*, Franz M. Weinert*, Stefan Duhr*, Kono H. Lemke†, Michael J. Russell‡, and Dieter Braun*§

*Biophysics Department, Ludwig-Maximilians Universität München, Amalienstrasse 54, 80799 München, Germany; †Geochemistry Group, Institute for Mineralogy and Petrology, Swiss Federal Institute of Technology, ETH-Zürich, 8092 Zürich, Switzerland; and ‡Jet Propulsion Laboratory, California Institute of Technology, Pasadena, CA 91125

Edited by Howard Brenner, Massachusetts Institute of Technology, Cambridge, MA, and approved March 9, 2007 (received for review October 28, 2006)

We simulate molecular transport in elongated hydrothermal pore systems influenced by a thermal gradient. We find extreme accumulation of molecules in a wide variety of plugged pores. The mechanism is able to provide highly concentrated single nucleotides, suitable for operations of an RNA world at the origin of life. It is driven solely by the thermal gradient across a pore. On the one hand, the fluid is shuttled by thermal convection along the pore, whereas on the other hand, the molecules drift across the pore, driven by thermodiffusion. As a result, millimeter-sized pores accumulate even single nucleotides more than 10^8-fold into micrometer-sized regions. The enhanced concentration of molecules is found in the bulk water near the closed bottom end of the pore. Because the accumulation depends exponentially on the pore length and temperature difference, it is considerably robust with respect to changes in the cleft geometry and the molecular dimensions. Whereas thin pores can concentrate only long polynucleotides, thicker pores accumulate short and long polynucleotides equally well and allow various molecular compositions. This setting also provides a temperature oscillation, shown previously to exponentially replicate DNA in the protein-assisted PCR. Our results indicate that, for life to evolve, complicated active membrane transport is not required for the initial steps. We find that interlinked mineral pores in a thermal gradient provide a compelling high-concentration starting point for the molecular evolution of life.

concentration problem | hydrothermal vents | molecular evolution | origin of life problem | RNA world

Starting with Miller and Urey (1), a wide range of studies on the origin of life discuss the chemical synthesis of protobiomolecules (2–4). Concurrently, the studies of replication systems (5–8) culminated in the RNA-world proposal (9). All these approaches require fairly high concentrations of small proto-biotic molecules, whereas geochemical extrapolations indicate a dilute prebiotic ocean with concentrations comparable to contemporary values (10, 11). This discrepancy has been termed the concentration problem of the origin of life (10, 12). In the following, we describe a robust and efficient solution to the concentration problem, based on heat currents in porous mineral precipitates comprising a hydrothermal mound developed over a moderately warm submarine spring.

Living cells are crowded with small molecules which are accumulated as a result of highly evolved active transport mechanisms across the cell membrane (13). A comparably effective transport mechanism is required to solve the concentration problem of the origin of life. However, to accumulate molecules from a highly diluted prebiotic ocean (10, 11), a considerable entropic gap has to be bridged. In a rough estimate, at least a 10^6-fold accumulation is required for small protobiomolecules to interact. To fulfill the second law of thermodynamics, such states of exceedingly low entropies can only be siphoned from a larger nonequilibrium system. Contemporary life sustains the required high molecular concentration in a dissipative nonequilibrium state by a wide range of highly evolved strategies. For the evolution of life, an already existing protobiological dissipative environment is required (14). The most compelling would refer to an accumulation of molecules into preexisting abundant compartments of cellular dimensions (15). Both requirements are fulfilled by the accumulation mechanism we propose here.

Hydrothermal Setting

From a geological point of view, thermal gradients are the most abundant dissipative systems on the early earth. They drive convective water flow with a wide variety of geometries. Contemporary hydrothermal vents, both black smokers and "Lost City" type vents, are only extreme cases for heat dissipation. Hydrothermal vents are surrounded by highly porous mineral precipitates. Within these structures, we consider the ubiquitous millimeter to micrometer sized pores and syneresis cracks (Fig. 1*a*). A temperature gradient, typically along the horizontal direction, exists across such pore systems. We show that these natural settings can easily accumulate single nucleotides $>10^8$-fold at the bottom of a plugged pore system. Thus, this accumulation is sufficient to step up from the dilute hydrothermal solution to molar concentrations within the pore.

It is well known that probiotic reactions can be envisaged to foster molecular evolution and favor synthesis over hydrolysis only when concentrations are sufficiently high (16). Submarine hydrothermal environments were previously envisaged as potential sites for the emergence of life, partly because of their contemporary habitability and partly because essential basic materials can be found in such environments (14, 15, 17–20). The concentration mechanism described here considerably strengthens the scenario for a hydrothermal emergence of life.

Robust Exponential Accumulation

The mechanism of accumulation operates as follows. In a hydrothermal vent a plugged pore system is sandwiched between the hot vent interior and the cooling outside ocean (Fig. 1*b*). A temperature gradient across the pore drives two entangled processes: (*i*) molecules are shuttled up and down the cleft by laminar thermal convection and (*ii*) thermophoresis drives the molecules along the temperature gradient, i.e., perpendicular to the convection flow. Both processes are indicated by white arrows in Fig. 1*c*. In combination, they lead to a strong vertical accumulation toward the closed bottom of the cleft. This geological setting is analogous to a Clusius-tube or thermogravitational column (21). We simulate the behavior of rather rapidly diffusing single nucleotides. Even with conventional biotechno-

Author contributions: D.B. designed research; P.B., F.M.W., and S.D. performed research; P.B., F.M.W., S.D., K.H.L., M.J.R., and D.B. analyzed data; and P.B., K.H.L., M.J.R., and D.B. wrote the paper.

The authors declare no conflict of interest.

This article is a PNAS Direct Submission.

See Commentary on page 9105.

§To whom correspondence should be addressed. E-mail: dieter.braun@physik.lmu.de.

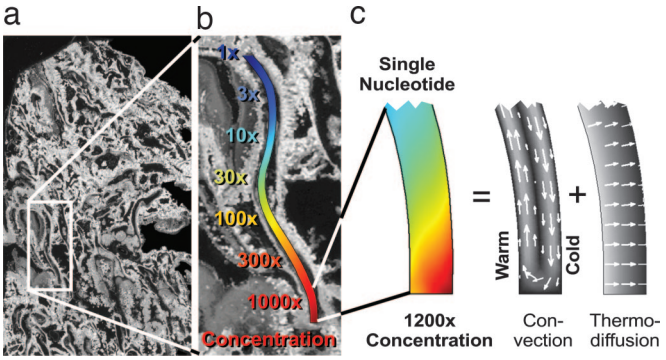

Fig. 1. Heat-driven molecular accumulation in hydrothermal pores. (*a*) Section through aragonite ($CaCO_3$) from the submarine hydrothermal vent field at Lost City (kindly provided by D. Kelley; ref. 20). (*b*) Simulation of a part of the pore system. If subjected to a horizontal thermal gradient of 30 K, a 1,200-fold accumulation of single nucleotides is expected (logarithmic concentration color scale). A concatenation of three of these pore sections leads to a 10^9-fold accumulation. (*c*) The mechanism of accumulation is driven by heat in a twofold way. Thermal convection shuttles the molecules vertically up and down and thermophoresis pushes the molecules horizontally to the right. The result is a strong molecular accumulation from the top to the bottom (linear concentration color scale).

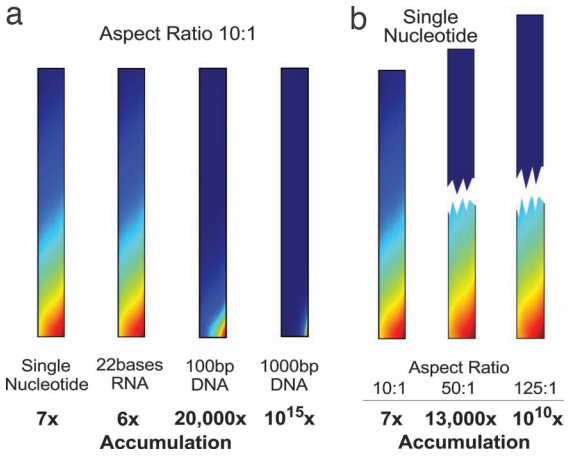

Fig. 2. Predicted effects of the molecule size and pore length on the accumulation level. The simulation results are based on the experimentally measured Soret coefficients and diffusion coefficients for DNA and RNA (see Table 1). (*a*) The accumulation increases exponentially with the size of the molecule. Whereas single nucleotides are accumulated 7-fold in a short cleft of aspect ratio 10:1, double-stranded DNA comprising 1,000 base pairs accumulates 10^{15}-fold. The equilibration takes 9 min for single nucleotides and 14 min for single stranded RNA comprising 22 bases. For DNA polynucleotides of 100 and 1,000 bp it takes 18 or 33 min, respectively. (*b*) Elongation of the cleft exponentially increases the accumulation. For example, the accumulation of single nucleotides is raised to a 10^{10}-fold level in a pore with an aspect ratio of 125:1. A linear concentration scale is used in both plots, scaled to the respective maximal concentration. The time to reach steady state is 9 min for $r = 10$, 4 h for $r = 50$ and 23 h for $r = 125$.

logical or microfluidic laboratory methods, such small molecules are hard to concentrate because of their considerable diffusion. The simulation shows a strong 1,200-fold downward accumulation of single nucleotides for the 5 mm short, bent cleft of Fig. 1*b*. As we will see later, a concatenation of three of these pores leads to a $1{,}200^3 = 1.7 \times 10^9$-fold accumulation.

We applied a 30 K temperature difference across the pore and found that maximal accumulation occurred in a pore with a cross-section of 145 μm. The diffusion of molecules in the convection flow was calculated by solving the combined Navier–Stokes, diffusion and heat transfer equations using commercial finite element software (Femlab, Comsol). The simulated pores feature a closed bottom and an open top end. The biomolecule concentration was fixed at the top, whereas the bulk fluid was subjected to gravity and restricted by the pore with nonslip boundary conditions. The heat transfer is barely affected by the slow laminar convection, and the temperature drops linearly across the pore structure.

Previously, we measured the thermophoretic characteristics of nucleotides using microfluidic fluorescence techniques (22). Molecules move along a thermal gradient ∇T with a drift velocity $v = -D_T \nabla T$. The ratio between the thermodiffusion coefficient D_T and the mass diffusion coefficient D is termed the Soret coefficient $S_T = D_T/D$, which typically determines the steady state concentrations. The values for single nucleotides are measured by using the fluorescent molecule 2′,7′-bis(carboxyethyl)-5 (6)-carboxyfluorescein (BCECF) in a 1 mM Tris buffer. BCECF and single nucleotides are of comparable size and charge. We also obtained S_T values for single stranded RNA of 22 bases in sodium chloride-sodium citrate-buffer with a monovalent salt concentration of 1.7 mM as well as double-stranded DNA of 100 and 1,000 bp in 1 mM Tris buffer. All measurements are performed at pH 7.8. In the experiments, the Soret coefficient S_T changes only by a factor of about three when the concentration of monovalent salt is increased from 1.7 to 170 mM. The Soret coefficient of a single nucleotide is comparable to the considerably larger single-stranded RNA of 22 bases. This is typical for thermodiffusion of charged particles smaller than the debye length and is due to reduced ionic shielding (22). Notably, single stranded RNA with 22 bases shows an ≈3-fold smaller thermodiffusion than single-stranded DNA of the same length. The experimental results are presented in Table 1.

A short pore with an aspect ratio of 10:1 accumulates single nucleotides 7-fold (Fig. 2*a*). A pore with the same aspect ratio accumulates a 22-bases-long single-stranded RNA to 6-fold, a 100-bases-long double-stranded DNA to 20,000-fold, and a 1,000-bases-long DNA to 10^{15}-fold levels. For these larger molecules, the short pore behaves like a molecule trap: once molecules enter the top of the pore, they are transported to the pore base and are accumulated to molar-level concentrations in a micrometer-sized spot in bulk water. As a result, the accumulated molecules diffuse freely and would find chemical reaction partners comparable to the situation within prokaryotic cells (13).

Pertinent to our argument is the fact that accumulation grows exponentially both with the size of the molecule and the length of a concatenated pore system. In concatenated pores accumulation of molecules increases exponentially, a result of the considerable concentration independence of thermophoresis below molar concentrations (23–25). Thus, although single nu-

Table 1. Soret coefficient (S_T) and diffusion coefficient (D) for different molecules

Coefficient	Single nucleotide	ssRNA, 22 bases	ssDNA, 22 bases	dsDNA, 100 bp	dsDNA, 1,000 bp
S_T 1.7 mM salt, per K	0.015	0.014	0.044	0.075	0.3
S_T 170 mM salt, per K	0.006	0.003	0.01	0.019	0.09
D, $\mu m^2/s$	400	100	115	45	8

Table 2. Predicted accumulation depends on the type of molecule and pore aspect ratio

Aspect ratio	Single nucleotide	ssRNA 22 bases	dsDNA 100 bp	dsDNA 1,000 bp
10:1	7	6	2×10^4	10^{15}
25:1	120	89	10^{10}	(10^{37})
50:1	13,000	8,000	(10^{21})	(10^{75})
125:1	10^{10}	6×10^9	(10^{52})	(10^{187})

Accumulation levels that cannot be reached because of steric hindrance are denoted in brackets.

cleotides accumulate merely 7-fold in the short pore of Fig. 2*a*, concatenating 12 of these pores using a wide variety of orientation angles exponentiate the accumulation to an extreme $7^{12} = 10^{10}$-fold level. Elongation of the pore has exactly the same effect. As shown in Fig. 2*b*, a pore system with a total aspect ratio of $r = 125$:1 accumulates single nucleotides 10^{10}-fold. Notably, the length of this pore system is only 18 mm, below the typical lengths of pore systems in hydrothermal settings. A compilation of the simulated accumulation values is given in Table 2.

The analytical solution for the accumulation in a rectangular cleft geometry confirms the above numerical findings. The analytical theory (26, 27) was originally developed for gas separation columns (21). The accumulation is found to be an exponential function given by

$$\frac{c_{\mathrm{BOTTOM}}}{c_{\mathrm{TOP}}} = \exp[0.42 \times S_{\mathrm{T}} \times \Delta T \times r] \qquad [1]$$

with the Soret coefficient S_{T}, the temperature difference ΔT and the aspect ratio r. For $0.42 \times S_{\mathrm{T}} \times \Delta T \times r \gg 1$, the molecular accumulation is large and rises exponentially with temperature difference ΔT or pore length. In pores with a sufficient aspect ratio r, substantial accumulation is reached even for small molecules with tiny Soret coefficients (Table 1). The exponential characteristic of Eq. **1** makes the accumulation robust because a small elongation of the pore leads to a large increase in molecular accumulation. Every linear decrease in the temperature difference ΔT can be compensated by a linear increase in pore aspect ratio r. For example, to achieve the same accumulation at just one tenth of the temperature difference, a 10-fold longer pore is needed. To illustrate this the accumulation versus the aspect ratio, r is plotted in Fig. 3 for single nucleotides, polynucleotides of 22 single stranded RNA bases, and double-stranded DNA comprising 100 and 1,000 base pairs.

The accumulation is highly robust with respect to the changes in the geometry of the pore. Fig. 4*a* shows various geometries that yield equal accumulations. We start with a rectangular pore with an aspect ratio of $r = 10$:1. The accumulation remains at the same level even if the pore is heavily dented, bent, incised, opened toward a bottom molecule repository, or strongly inclined. This insensitivity to geometric variation has two main reasons. First, mass diffusion bridges regions with inferior accumulation. This diffusion between the pores does not require any special geometries between the pore sections. Second, the slowing down of convection resulting from a tilt of the pore section can be easily compensated by a small increase in the pore width, because of the exponent 1/3 in Eq. **2**. For example, a tilt from 90° (vertical) to 1° (basically horizontal) enlarges the optimal cleft width only by a factor of four. Therefore, a wide variety of pore systems accumulate molecules with equal efficiency.

So far, we have discussed only two-dimensional pores with cleft-like geometries. We simulated the cross-section and assumed that the pore extends considerably further into the third

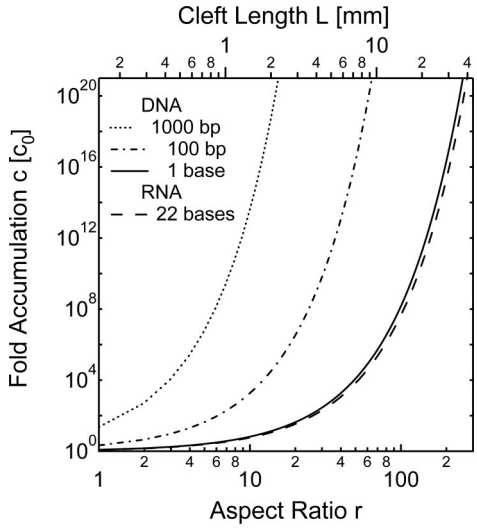

Fig. 3. Exponential accumulation. The accumulation depends exponentially on the aspect ratio r and the temperature difference ΔT, according to the analytical theory (Eq. **1**). Even for single nucleotides, it is remarkably easy to reach exceedingly large molecular accumulations. The accumulation is calculated for $\Delta T = 30$ K.

dimension. However, equal accumulation is also found for pores with only limited extension in the third dimension. Fig. 4*b* shows results for various pore cross-sections with comparable accumulation levels. Also, molecular accumulation is not seen to be significantly lowered over a variety of depths. As noted before, all of the geometries shown in Fig. 4 can be concatenated ad libitum, yielding a wide range of pore system geometries that are capable of an efficient molecular accumulation.

A critical parameter is the width of the pore. For an extended rectangular cleft (26, 27), the largest accumulation is found for an optimal width d_0 given by

$$d_0 = 8.4 \times (\mu D/\alpha\rho g_0 \Delta T \sin\Theta)^{1/3} \qquad [2]$$

with the viscosity of the fluid μ, the diffusion coefficient of the molecule D, the fluid volume expansion coefficient α, the fluid density ρ, the gravitational acceleration g_0, the inclination angle Θ to the horizontal plane, and the temperature difference ΔT. As

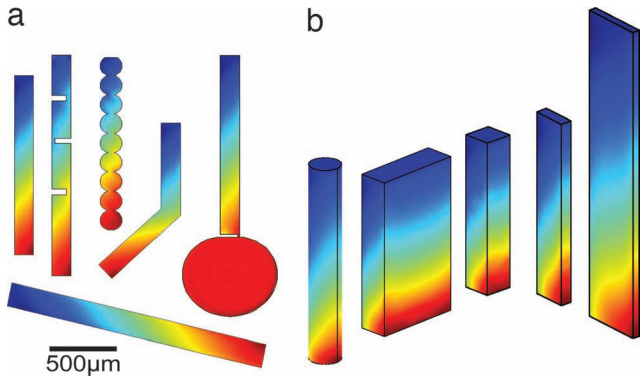

Fig. 4. Robustness of the accumulation. (*a*) Equally efficient accumulation is found for a large variety of geometries. Regions of reduced accumulation are bridged vertically by mass diffusion. Strongly inclined pores accumulate molecules equally well. A linear concentration scale is used in both plots. (*b*) Likewise, a wide range of pore cross-sections yields identical accumulations. As for two dimensional clefts, optimal accumulation is achieved if the convection speed balances the diffusion time across the pore.

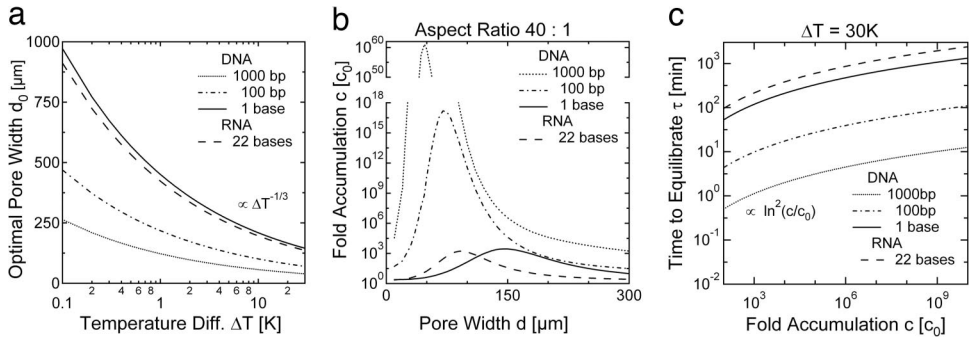

Fig. 5. Pore width and equilibration time. (*a*) The optimal cleft width depends moderately on the molecular size and temperature difference. The optimal cleft width is proportional to $D^{1/3}$ and $\Delta T^{-1/3}$ with the diffusion coefficient D and temperature difference ΔT. As a result, much longer nucleotides require only slightly narrower pores. (*b*) Accumulation drops considerably for pores with a nonoptimal width. Nucleotides are selectively accumulated in particularly narrow chambers. For a wider pore width $d \approx 150$ μm, the accumulation of molecules with different sizes reaches comparable levels. (*c*) The equilibration toward a 10^8-fold accumulation takes 14 h for single nucleotides and 25 h for single-stranded RNA comprising 22 bases. For DNA polynucleotides of 100 and 1,000 bp. it takes 70 or 8 min, respectively. This might be counterintuitive, but larger molecules accumulate faster because a considerably shorter cleft is sufficient to achieve the same level of accumulation.

the result of the exponent 1/3 in Eq. **2**, values for d_0 fall between 40 and 400 μm for an extensive range of parameters D, Θ, and ΔT, as shown in Fig. 5*a*.

Fig. 5*b* illustrates the pore size dependence of the accumulation in more detail. DNA molecules of different length are selectively partitioned depending on the pore width. For an equivalent value of ΔT (30 K), single nucleotides accumulate best for a pore width of 145 μm, whereas a 1,000-bp DNA fragment accumulates best for a width of 40 μm. Therefore, the geometry determines the size of the preferentially accumulated molecules. On the other hand, the accumulation of longer polynucleotides is much more efficient, and pore widths $\approx$150 μm accumulate a wide range of different DNA lengths equally well. Monomers and polymers accumulate to similar levels under all these various pore conditions (Fig. 5*b*).

The time τ to reach a steady state concentration profile is given by the diffusion time along the pore

$$\tau = r^2 d_0^2 / \pi^2 D. \qquad [3]$$

As a result, a 10^8-fold accumulation of single nucleotides is achieved after $\tau = 14$ h, and for a 22-base single-stranded RNA, a 10^8-fold accumulation is achieved after $\tau = 25$ h. However, the time to reach a comparable accumulation for larger molecules drops to 70 min for 100-bp DNA and 8 min for 1,000-bp DNA (Fig. 5*c*), the reason being the much shorter cleft length required for longer DNA.

Notably, all these times are extremely short compared with the lifetime of a typical vent chimney, or even the Lost City vent system, which operates at least for 30,000 years (20, 28).

We also tested the robustness of accumulation against diffusive leakage from the pore. In general, a leak of molecules into an attached closed pore space does not inhibit accumulation. An example is shown in Fig. 4*a*, where a large extension is filled to the same high concentration at the pore base. Only the equilibration time slightly increases as a result of such an extension of the pore. However, leaks into permeable chambers can reduce the accumulation, depending on the concentration gradient ∇c and the resulting diffusive molecular flux, $j = -D\nabla c$. The distance between the leak and the surrounding background concentration $c = 1$ is crucial. This distance is expected to be relatively large for a hydrothermal mound. To characterize the effects of diffusive leaks, we simulated a worst case scenario. A wide diffusive leak is placed at the base of a pore and is connected to the outside over a distance of the pore length itself (Fig. 6*a*). Otherwise the same geometrical condition as illustrated in Fig. 2a is used, namely an aspect ratio of $r = 10{:}1$ with an optimal width d_0. Thus, we effectively simulate a tube which is open to both sides. Compared with a nonleaking pore, the resulting accumulation is reduced from 7 to 3 for single nucleotides, from 6 to 2.6 for single-stranded RNA, from 20,000 to 2,000 for 100-bp DNA and from 10^{15} to 10^{13} for 1,000-bp DNA. These reductions in accumulation that stem from leakage are quite easily compensated for by extending the length of the pore. We conclude that, even if the pore leaks through diffusion, accumulation is maintained at a high level.

In addition to diffusion, slow water flow through pore leakages might hinder accumulation. We focus on an upward flow because this direction is most probable in a hydrothermal mound. We use the same geometry as before (see Fig. 6*a*), but now add an upward flow at the lower end of the leak. This flow is fed with molecules from the outside concentration of $c = 1$. Obviously, such an upward flow through the pore directly competes with the downward accumulation. The accumulation versus flow rate is plotted in Fig. 6*b*. For comparison, the typical convection flow inside the pore is on the 1–10 μm/s scale. Fig. 6*b* shows that the accumulation of single nucleotides is quite robust against the upflow, probably because of the rapid diffusion of these molecules. Slower diffusing molecules are more vulnerable to pore

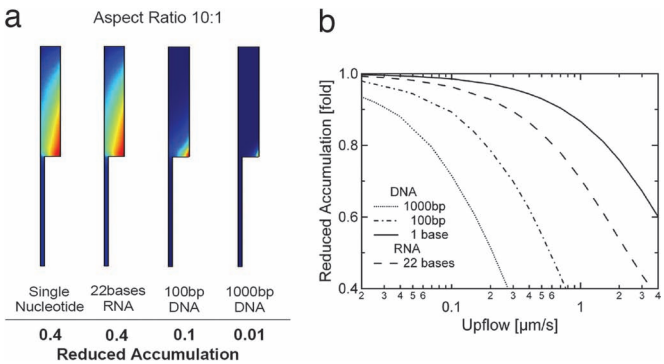

Fig. 6. Reduction of the accumulation by diffusive leakage and upflow. (*a*) A diffusive leak is introduced at the bottom of the pore over 1/5 of the pore width. The numbers beneath indicate the reduction of accumulation relative to the nonleaking pore in Fig. 2*a*. (*b*) Upflow is introduced into the cleft shown on the left side. For longer polynucleotides, the accumulation drops considerably faster with increasing upflow. Short molecules are less affected. The drop in accumulation for both diffusive leaks and upflow drift is readily compensated by a slight elongation of the pore.

flow drift, as can be seen from Fig. 6*b*. For a 22-base single-stranded RNA, the accumulation drops by a factor of two for an upflow of ≈2.5 μm/s. For 100-bp DNA and 1,000-bp DNA, accumulation drops by the same factor for an upflow of 0.6 and 0.2 μm/s, respectively. These flow rates are comparable with the thermal convection speed in the pore. Flow rates in pores of hydrothermal mounds are hard to estimate but are probably slower than these values. As expected, strongest accumulation is found in pores that are well sealed at the bottom. According to our assessment, drift and diffusion in microscopic pore systems in hydrothermal precipitates do not, or only weakly, affect the proposed accumulation mechanism.

Discussion

We compare the assumptions on pore geometry with the geological record. As seen from the representative cross-section in Fig. 1*a*, an aspect ratio between 25 and 50 can be estimated for single elongated pore spaces in the mounds at the Lost City vent site (≈20–100 μm across and ≤1 mm long). Although, at Lost City, pore shapes may be governed by filamentous bacterial growth, chemical garden-like growth with even higher aspect ratios is likely to occur in comparable hydrothermal systems with moderate temperatures. For example, the 500-mm-long hydrothermal pyrite spires from the 352-million-year-old Tynagh zinc-lead sulfide deposit, Ireland, have central cavities that are ≈100 μm in diameter (aspect ratio $r \leq 5{,}000{:}1$) (ref. 29 and Fig. 3*b*). Similar structures have been realized in laboratory simulations (30). Thus, the projected extreme accumulation should be easily reached in natural settings. In any case, the accumulation is exponentiated when low aspect ratio clefts are interconnected. Note that pore concatenation is an especially interesting feature from a geological point of view. During hydrothermal dissolution pores enlarge, become more interconnected (i.e., the value of the aspect ratio increases), and can substantially promote the accumulation of molecules. Based on these results, and given the large number of clefts in any one of multitudinous submarine hydrothermal mounds on the early earth (29), the opportunities would have been manifold for a critical accumulation of organic monomers and polymers synthesized in the same milieu.

In the above calculations, we have assumed a temperature difference of $\Delta T = 30$ K. We anticipate that this is a realistic assumption, because temperature gradients are focused inside the clefts due to the considerably lower thermal conductivity of water (0.6 W/mK) as compared with the surrounding rock (>3 W/mK). The thermal conductivity measured for a hydrothermal pyrite–silica precipitate (31) is 14 W/mK, but the isolated pyrite and quartz minerals yield ≈20 W/mK and 3–4 W/mK, respectively, in laboratory tests (32). The resulting enhancement of the temperature gradient in the liquid part of the pores is 5- to 200-fold. Thus, to obtain the temperature difference of 30 K assumed in the above simulations, the required overall temperature gradient is of the order of 1–40 K/mm, well within reported values of ΔT for natural hydrothermal settings. However, focusing of the temperature gradient in the pores is not essential for the accumulation process. For lower thermal gradients, the same accumulation can be achieved if the pore system is elongated linearly for a decreased temperature difference.

The presented accumulation geometry surpasses previous approaches. Experiments with a circular, laser-heated geometry demonstrated that thermal convection could drive the DNA replicating PCR (33). In the same setting, we observed a considerable accumulation of long DNA (34). Although both of those experiments pointed toward the potential for convection to contribute to the emergence of life (35), no accumulation of short molecules was found or theoretically expected. We now know that this was due to the low aspect ratio of the chamber geometry ($r \approx 0.1$). The pore geometries studied here, however, demonstrate a strong accumulation of small molecules, such as single nucleotides, in a highly plausible geological setting on the early earth.

As we have seen, large molecules accumulate more efficiently. One may ask whether the strong accumulation of solvated organic molecules would lead to the tarring of the pore. This is not expected because thermophoretic coefficients become small for concentrations in the molar range (23–25). As a result, accumulation will level out at similar concentrations and will not lead to tarring. Also, a closing of the pore by microscopic solid particles is unlikely, based on our recent experimental findings (36). It was shown that, for low aspect ratio chambers ($r \approx 0.1$), 2-μm polystyrene spheres became highly concentrated, but still only formed two or three layers of a colloidal crystal. Further accumulation into the volume of the chamber was disrupted by flow interactions of the solid particles with the thermal convection current (36). As a result, convective flow itself is likely to prevent tarring of the pore by larger particles. On the other hand, a minor accumulation of sticky particles at the pore bottom could contribute to the sealing of the leaks (see Fig. 6). Moreover, in this process, any pore shortening would be negligible.

The mechanism provides concentrated molecules in bulk water without requiring molecules to adsorb onto surfaces. Surface-assisted accumulation is often thought to solve the concentration problem, either via drying or specific adsorption. However, biological systems complex enough to evolve a replicating machinery would most likely need to disconnect, at least temporarily, from such restricting adsorbing surfaces (37). During this desorption or wetting process, there is a high risk of losing the replicated molecules into the bulk water (38). In the present scenario, where they would simply be reaccumulated from the pore solution and the catalytic activity of surfaces can be efficiently used. Our approach has the advantage of offering an active concentration mechanism in an already existing, robust enclosure. Because thermophoretic drift is common for molecules, the accumulation scheme applies similarly to nucleic acids, amino acids, and lipids.

The described accumulation in semiclosed microscopic pores has several synergistic advantages that pertain to the molecular evolution of early life. The enclosure of pore space by mineral precipitates frees life from the need to build a semipermeable organic membrane in its very first evolutionary steps. Microbiological evidence indicates that membrane synthesis appears to be a rather late development (15, 18). Moreover, active transport across a membrane to accumulate molecules in a cell is well known to be a highly evolved process, requiring complex proteins to form vesicles and to actively pump molecules across the membrane.

Notably, the mineral pores that we propose as accumulation centers for the emergence of life are presently populated with thermophilic prokaryotes, and it is speculated that these sites could have been inhabited by the last common ancestor and its biochemical precursors (15, 39). Rapid thermal quenching was demonstrated to be able to polymerize both nucleic (40) and amino (16) acids in a setting in which hydrothermal fluids were injected into cooled (4°C) water. The discussed setting of thermal convection provides comparable temperature interfaces, but now within a single pore. Therefore, both the temperature drop and the needed molecule concentration could be found in an enclosure instead of an open flow reactor.

The water inside the pore network is permanently shuttled by laminar thermal convection. Molecules that stochastically escape the accumulation at the bottom of the pore by diffusion are subjected to a rapid periodic temperature variation within a wide range of temperature amplitudes and cycle times inside a single pore. Equally, freshly precipitated mesoscopic mineral grains are subjected to thermal cycling by the convection. Their catalytic surfaces might generate nucleic acid multimers by thermally triggered periodic condensation (4) and unbinding reactions. In

this context, we note that, in a comparable thermal convection setting, DNA was shown to replicate exponentially by using the, albeit protein-catalyzed, PCR (33, 41).

In conclusion, we propose a type of mechanism, driven solely by a temperature gradient, which strongly accumulates even small protobiological molecules in semiclosed hydrothermal pore systems. This setting provides a compelling, dissipative microenvironment to promote the first steps in the molecular evolution of life.

Materials and Methods

Combined solutions of the Navier-Stokes equation (velocity $\vec{u}$, pressure p, density ρ, viscosity η), molecule diffusion (concentration c, diffusion coefficient D), and heat transfer (temperature T, heat conductivity k) were simulated in two dimensions by a finite element solver (Comsol, Femlab). Cross terms induce the thermal convection with the expansion coefficient α and the gravitational acceleration g_0, trigger thermophoresis with the thermodiffusion coefficient D_T and consider the flow-induced heating with the heat capacity c_P. Boundary conditions were nonslip for $\vec{u}$, neutral for c except for fixing the concentration to $c = 1$ at the top opening of the column and a horizontal temperature difference of ΔT across the cleft. Material parameters were as follows: density of water 1,000 kg/m^3, viscosity 0.0012 ($N \times$ s)/m^2, heat capacity 4,200 J/(kg $\times$ K), heat conductivity 0.6 W/(m $\times$ K), volume expansion 3.2×10^{-4}, cold temperature 293 K, temperature difference 30 K, and gravitational acceleration 9.8 m/s^2. The temperature dependence of the above parameters is not significant in the simulations. The Femlab simulation files can be obtained from the authors.

We thank Ludmilla Mendelevitch for initial simulations and Hermann Gaub for hosting D.B.'s Emmy–Noether Nachwuchsgruppe, which was funded by the Deutsche Forschungsgemeinschaft. M.J.R.'s work was conducted at the Jet Propulsion Laboratory, California Institute of Technology, under contract with the National Aeronautics and Space Administration.

1. Miller SL (1953) *Science* 15:528–529.
2. Drobner E, Huber H, Wächtershäuser G, Rose D, Stetter KO (1990) *Nature* 346:742–744.
3. Zubay G (2000) *Origins of Life on the Earth and in the Cosmos* (Academic, New York), 2nd Ed.
4. Ferris JP (2002) *Origins Life Evol Biosph* 32:311–332.
5. Eigen M (1971) *Naturwissenschaften* 58:465–523.
6. Kuhn H (1976) *Naturwissenschaften* 63:68–80.
7. Sievers D, von Kiedrowski G (1994) *Nature* 369:221–224.
8. Joyce GF (1989) *Nature* 338:217–224.
9. Cech TR, Atkins JF, Gesteland RF, eds (2000) *The RNA World* (Cold Spring Harbor Lab Press, Plainview, NY).
10. Dose K (1975) *Biosystems* 6:224–228.
11. Mojzsis SJ, Harrison TM, Pidgeon RT (2001) *Nature* 409:178–181.
12. de Duve C (1991) *Blueprint for a Cell: The Nature and Origin of Life* (Neil Patterson, Burlington, NC).
13. Ellis RJ (2001) *Trends Biochem Sci* 26:597–604.
14. Corliss JB (1990) *Nature* 347:624.
15. Koonin EV, Martin W (2005) *Trends Genet* 21:647–654.
16. Imai E, Honda H, Hatori K, Brack A, Matsuno K (1999) *Science* 283:831–833.
17. Russell MJ, Hall AJ, Cairns-Smith AG, Braterman PS (1988) *Nature* 336:117.
18. Russell MJ, Hall AJ (1997) *J Geol Soc London* 154:377–402.
19. Nisbet EG, Sleep NH (2001) *Nature* 409:1083–1091.
20. Kelley DS et al (2001) *Nature* 412:145–149.
21. Clusius K, Dickel G (1938) *Naturwissenschaften* 26:546.
22. Duhr S, Braun D (2006) *Proc Natl Acad Sci USA* 103:19678–19682.
23. Duhr S, Arduini S, Braun D (2004) *Eur Phys J E* 15:277–286.
24. Piazza R, Iacopini S, Triulzi B (2004) *Phys Chem Chem Phys* 6:1616–1622.
25. de Gans BJ, Kita R, Wiegand S, Luettmer-Strathmann J (2003) *Phys Rev Lett* 91:245501.
26. Furry WH, Jones RC, Onsager L (1939) *Phys Rev* 55:1083–1095.
27. Debye P (1939) *Annalen der Physik* 36:284–294.
28. Kelley DS, Karson JA, Fruh-Green GL, Yoerger DR, Shank TM, Butterfield DA, Hayes JM, Schrenk MO, Olson EJ, Proskurowski G, *et al* (2005) *Science* 307:1428–1434.
29. Russell MJ, Hall AJ, Boyce AJ, Fallick AE (2005) *Econ Geol* 100:419–438.
30. Stone DA, Goldstein RE (2004) *Proc Natl Acad Sci USA* 101:11537–11541.
31. Rona PA, Davis EE, Ludwig RJ (1998) *Proc Ocean Drilling Prog Sci Results* 158:329–336.
32. Clauser C (2006) in *Landolt-Börnstein: Numerical Data and Functional Relationships*, ed Heinloth K (Springer, Heidelberg).
33. Braun D, Goddard NL, Libchaber A (2003) *Phys Rev Lett* 91:158103.
34. Braun D, Libchaber A (2002) *Phys Rev Lett* 89:188103.
35. Braun D, Libchaber A (2004) *Phys Biol* 1:1–8.
36. Duhr S, Braun D (2005) *Appl Phys Lett* 86:131921.
37. Duve CD, Miller SL (1991) *Proc Natl Acad Sci USA* 88:10014–10017.
38. Wächtershäuser G (1994) *Proc Natl Acad Sci USA* 91:4283–4287.
39. Martin W, Russell MJ (2003) *Philos Trans R Soc London B* 358:59–85.
40. Ogasawara H, Yoshida A, Imai E, Honda H, Hatori K, Matsuno K (2000) *Origins Life Evol Biosph* 30:519–526.
41. Krishnan M, Ugaz VM, Burns MA (2002) *Science* 298:793.

Observation of Slip Flow in Thermophoresis

Franz M. Weinert and Dieter Braun*

Systems Biophysics, Ludwig Maximilians Universität München, Amalienstrasse 54, 80799 München, Germany

(Received 4 September 2007; published 13 October 2008)

Two differing theories aim to describe fluidic thermophoresis, the movement of particles along a temperature gradient. While thermodynamic approaches rely on local equilibrium, hydrodynamic descriptions assume a quasi-slip-flow boundary condition at the particle's surface. Evidence for slip flow is presented for the case of thermal gradients exceeding $(aS_T)^{-1}$ with particle radius a and Soret coefficient S_T. Thermophoretic slip flow at spheres near a surface attracts or repels tracer particles perpendicular to the thermal gradient. Moreover, particles mutually attract and form colloidal crystals. Fluid dynamic slip explains the latter quantitatively.

DOI: 10.1103/PhysRevLett.101.168301 PACS numbers: 82.70.Dd, 82.40.Ck

Thermophoresis in water moves particles and molecules along a temperature gradient [1–3]. Typically, the particle velocity v is assumed to be a linear function of the temperature gradient ∇T: $v = -D_T \nabla T$, with the thermophoretic mobility $D_T = S_T D$, where the Soret coefficient is S_T and the diffusion coefficient is D. Several competing models have been proposed to describe the microscopic cause [4–17]. Recent experiments aim to distinguish between the models [18–21].

For small temperature gradients, the thermophoretic movement of polystyrene beads and DNA has been predicted quantitatively in the limit of a thin Debye layer, which is given by $a > 3\lambda$, where a is the hydrodynamic radius and λ is the Debye shielding length [8,10]. It was argued that the movement is the result of local equilibration driven by the thermal fluctuations of the particles [4–10]. However, such a local equilibrium model is expected to break down for thermal gradients exceeding the following condition [7–9]:

$$\nabla T > D/aD_T. \quad (1)$$

At larger thermal gradients, Marangoni-like quasislip on the particle surface is likely to dominate [11–17]. However, this regime is experimentally difficult to access. We devised two experimental strategies. In both cases, a cooling solid wall created a strong thermal gradient in the adjacent water film perpendicular to the surface. We probed the slip flow near the beads with smaller tracer particles, and we investigated how the hydrodynamic interaction between equal-sized particles leads to mutual attraction parallel to the surface.

In both cases, we found particle movement parallel to the wall although an insufficiently strong thermal gradient exists along this direction to cause the observed behavior. These findings cannot be explained with a local equilibrium approach, as the energy gradient parallel to the solid support is not sufficient to create the particle movement. However, the hydrodynamic interaction of the thermophoretic slip flow, which is deflected by the solid support, is responsible for the observed particle movement, as shown below.

At a gradient smaller than the criterion from Eq. (1), particle fluctuations dominate, and no attraction or tracer movement parallel to the wall is found. This does not contradict an explanation based on thermophoresis with local equilibrium [7,8,10]. Our finding of fluid flow at strong thermal gradients points towards an interesting transition in thermophoresis near the thermal gradient given by Eq. (1).

Materials and methods.—Water was homogeneously heated in a thin chamber (10–25 μm) by an infrared laser scanning microscope (1455 nm, 300 mW; for details, see [22]). The laser was uniformly scanned across a rectangular area using a moderately focused beam (diameter 80 μm). The horizontal chamber temperature was imaged with a fluorescent dye [8,9] and checked for homogeneity. The vertical thermal gradient is derived from thermal conductivities of the chamber materials: insulating plastic on top ($\lambda = 0.16$ W/mK) and cooling sapphire at the bottom ($\lambda = 34$ W/mK). Typically, thermal gradients in the range of 0.2–0.7 K/μm are generated at the sapphire surface, and the fluid temperature is increased by less than 5 K. To confirm that optical trapping effects were absent, we used heavy water which is 100-fold less absorbing than water. In this system, the thermal gradients are equally reduced. All observed effects were reversible; after switching off the heating, the particles diffused freely again.

Tracer particle attraction and repulsion (Fig. 1).—We used small tracer particles (0.5 μm diameter, F-8888, Molecular Probes) to probe the possible fluid flow in the vicinity of larger particles (10 μm diameter). The latter were made from either polystyrene (F13838, Molecular Probes) or silica (PSI-10.0, Kisker) which show a positive and negative Soret coefficient under these conditions, respectively. The tracer particles ($S_T = 8.9$ K^{-1}) are also subjected to downward thermophoresis in a thermal gradient of $\nabla T = 0.24$ K/μm in a 25 μm thick chamber filled with saline-sodium citrate buffer (15 mM NaCl and

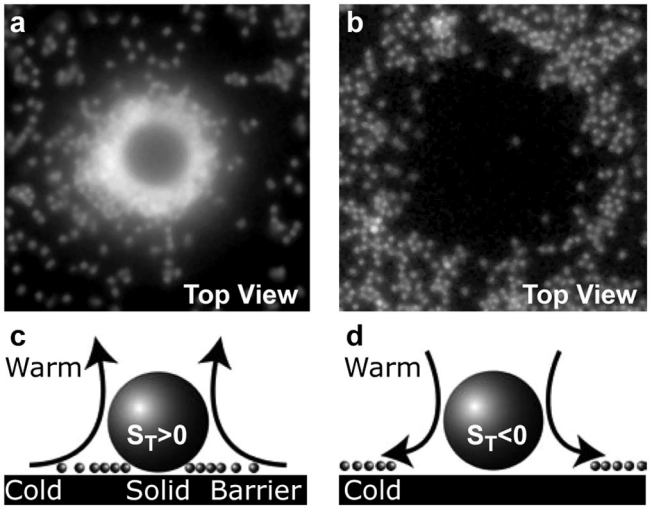

FIG. 1. The slip flow induced by a temperature gradient across particles with a diameter of 10 μm attracts or repels tracer particles of diameter 0.5 μm. The direction of the flow depends on the sign of the Soret coefficient of the large particle. (a) Polystyrene beads with $S_T > 0$ attract the tracer particles. (b) Silica spheres with $S_T < 0$ repel them. (c),(d) Schematic side view of the flow induced accumulation (depletion) of the tracer particles.

1.5 mM sodium citrate at pH 7.8) (Fig. 1). Tracer particles accumulated near a 10 μm polystyrene particle, where an upward directed slip flow was expected. The tracer particles were depleted from the area around the 10 μm silica particles, which had a negative Soret coefficient, thus indicating a downward slip flow [Figs. 1(c) and 1(d)].

Crystallization (Fig. 2).—In the above experiment, the 10 μm particles sedimented due to their weight. Smaller particles with a positive Soret coefficient can be moved to the cold surface by the thermal gradient. As a result of their surface-generated slip flows, the particles subsequently attract one another [Fig. 2(a)]. To probe this, we imaged 1 μm diameter polystyrene particles, which normally experience repulsive interactions with each other (10 pM, F-8823, Molecular Probes) in 100 μM tris(hydroxymethyl)aminomethane hydrochloride buffer (pH 7.8) inside a 10 μm thin plastic-sapphire chamber. Without thermal gradients, the particles diffused freely with a sedimentation length of $L = kT/F_{\mathrm{pot}} = 15$ μm, where F_{pot} is the gravitational force [Fig. 2(c), inset]. After switching on a thermal gradient of 0.65 K/μm [Fig. 2(b)], the thermophoretic drift decreased the sedimentation length to below $L = 1/(S_T \nabla T) = 100$ nm. As the particles reached the surface, they were attracted to one another within interparticle distances of several micrometers and formed two-dimensional crystals [Fig. 2(c)].

To exclude influences of optical effects induced by the laser, we externally applied the temperature gradient by cooling the outer top of an all-glass chamber to 14 °C while heating its bottom to 60 °C [Fig. 2(d)]. The temperature difference drops across the glass-water-glass chamber sandwich according to their respective thickness and heat

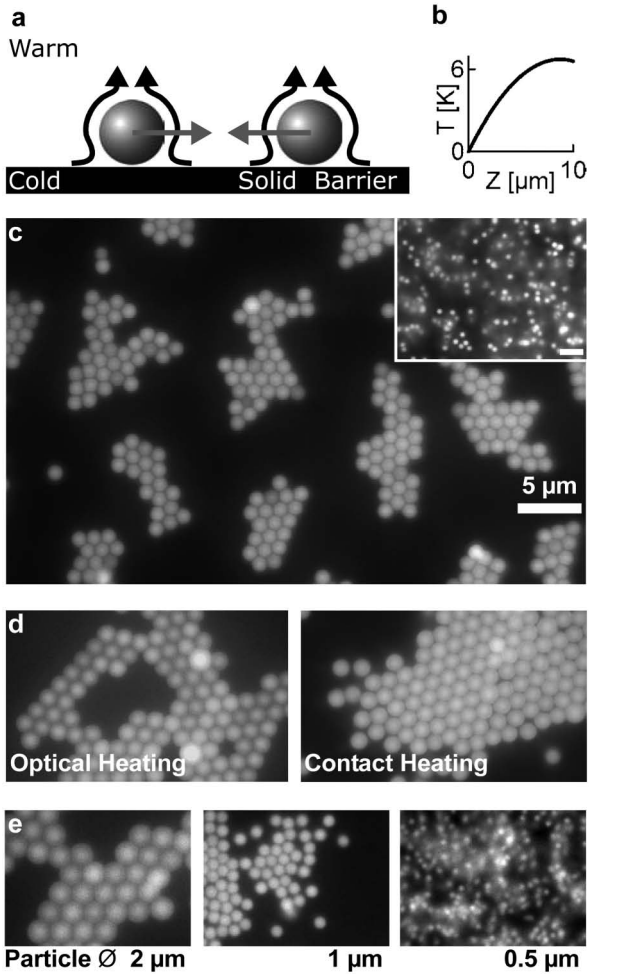

FIG. 2. *Thermophoretic crystallization.* (a) In a strong temperature gradient, particles move ballistically to the cold surface (side view). The persisting slip flow is deflected by the surface and leads to mutual hydrodynamic attraction. (b) Temperature profile. (c) Colloidal crystals of 1 μm polystyrene particles on a cold surface for positive Soret coefficients (view from the top after 20 s of heating). Inset: Before temperature application. (d) Crystals form equally well for a contact heated chamber without laser irradiation (2 μm particles). (e) At a fixed temperature gradient of 0.28 K/μm, crystallization strongly depends on the Soret coefficient, following the threshold condition of Eq. (1). See supplemental material [34].

conductivities and subsequently lifts the particles against sedimentation. We calculated a temperature gradient of 0.05 K/μm, slightly smaller than the optically applied gradient of 0.28 K/μm but still within the criterion (1). We find less densely packed crystals for 2 μm polystyrene particles under contact heating as expected from the weaker temperature gradient.

Size dependence.—As seen in Fig. 2(e), a thermal gradient of $\nabla T = 0.28$ K/μm applied to particles of different sizes caused strong varying degrees of attraction. Particles with 2 μm diameter ($S_T = 43$ K^{-1}) experienced high attraction to one another; moderate attraction was observed for 1 μm particles ($S_T = 20$ K^{-1}); no attraction was seen

for 0.5 μm particles ($S_T = 4\ \mathrm{K}^{-1}$). We found crystallization only when the criterion of Eq. (1) was fulfilled, where the values $\nabla T a S_T$ for the respective particle size were 12, 2.8, and 0.28.

Quantification of the attraction.—In a thermal gradient of 0.28 K/μm, we determined the attractive pseudopotential of a particle pair by tracking the interparticle distance distribution parallel to the surface. The usage of "pseudo" should imply that the forces are not conservative [23]. Figure 3(a) shows an image of the isolated 2 μm polystyrene particles, which were tracked ($S_T = 43/\mathrm{K}$, F-8827, Molecular Probes) and found to fluctuate in close proximity. We obtained the pseudopotential difference ΔV of the attraction from the Boltzmann distribution. The number of particles ΔN found within the distance interval $[d, d + \Delta d]$ is given by

$$\Delta N(d) = 2\pi d \bar{N} e^{-\Delta V(d)/kT} \Delta d, \tag{2}$$

with average particle density $\bar{N}$ [24]. Particle distances were recorded over 1300 s and included stochastic binding and unbinding processes of the particle pair. The resulting pseudopotential $\Delta V(d)$ from $N = 8300$ pair distance values is plotted in Fig. 3(b). The pseudopotential is shifted to zero potential at a distance of 8 μm. Beyond this distance, we did not obtain enough data to statistically evaluate the shape of the curve. The attraction well reaches a depth of 5 kT.

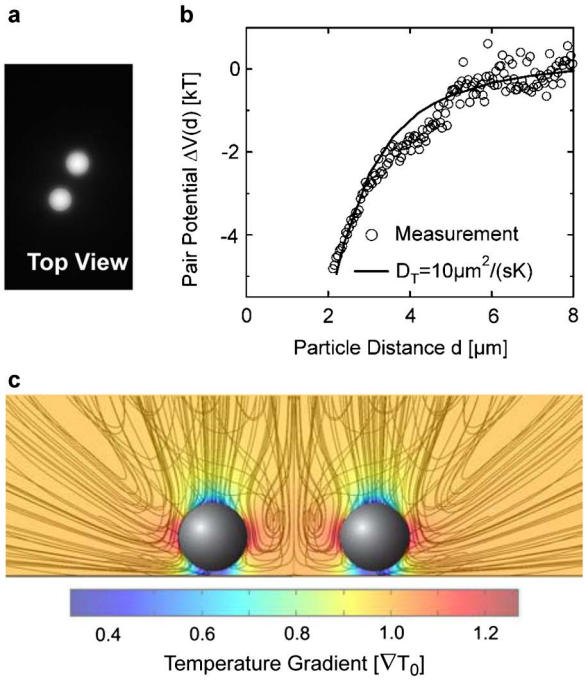

FIG. 3 (color online). *Particle attraction from thermophoretic slip flow.* (a),(b) The distance distribution of a single particle pair is measured by particle tracking. The effective pseudo pair potential $\Delta V(d)$ was determined using Boltzmann statistics (open circles). (c) The three-dimensional flow around the particles was calculated using finite elements. A projection of the flow lines is shown in gray; the thermal gradient is color coded and given in units of the free solution temperature gradient ∇T_0. The calculated pair potential is plotted as a solid line in (b).

Slip-flow boundary condition.—Slip-flow conditions in the Debye layer close to the surface of the particles have been proposed by Ruckenstein [11] and discussed by several authors, including Keyes [12], Anderson [13], Morozov [14], Semenov [15], Piazza [16], and Würger [17]. The details of the provided flow fields vary. We will compare our experiments with the flow fields of Piazza and Würger. The authors differ in their treatment of flow at the nanoscale and assume either nonslip flow (Piazza) or quasislip flow (Würger) at the particle-water interface inside the Debye layer. Both solutions are identical for distances r larger than the Debye length λ and for particles with radius $a \gg \lambda$, which is in the regime probed by our experiments.

The Marangoni force tangential to the surface counterbalances the off-diagonal components of the hydrodynamic surface stress [17]. In Cartesian coordinates (x, y, z), the tangential direction at the surface of the sphere is $\mathbf{t} = (-xz, -yz, x^2 + y^2)/(r\sqrt{x^2 + y^2})$ and the normal direction $\mathbf{n} = (x, y, z)/r$. With $r = \sqrt{x^2 + y^2 + z^2}$ and the fluid velocity $\mathbf{v}$, the surface boundary condition reads explicitly

$$\eta[r\mathbf{n} \cdot \nabla(\mathbf{t} \cdot \mathbf{v}/r) + \mathbf{t} \cdot \nabla(\mathbf{n} \cdot \mathbf{v})] = \gamma_T \mathbf{t} \cdot \nabla T. \tag{3}$$

The temperature dependence of the surface energy given by $\gamma_T = 3\eta D_T/a\kappa$ is set to match the thermophoretic mobility D_T in free solution within the pseudoslip condition framework. The factor $\kappa = (3\kappa_S)/(2\kappa_S + \kappa_P)$ is given by the thermal conductivities of water $\kappa_S = 0.54\ \mathrm{W/(m \cdot K)}$, polystyrene $\kappa_P = 0.13\ \mathrm{W/(m \cdot K)}$, and fused silica $\kappa_P = 1.3\ \mathrm{W/(m \cdot K)}$. The thermophoresis of particles was measured by single particle tracking [8] at similar thermal gradients. The treatment with nonslip in the Debye layer [16] gives the same simulation result. However, it requires a different microscopic parametrization for γ_T to match the measured values of D_T.

Finite element calculation.—We carried out the simulation using an industrial finite element solver in 3D (FemLab 3.1, Comsol). Nonslip boundary conditions were used at the bottom sapphire surface. The surrounding box was treated with symmetric boundaries at the symmetry plane between the spheres and neutral flow boundary conditions otherwise. The temperature gradient was calculated using bulk thermal conductivities of the materials. The particle was located above the bottom sapphire at the sedimentation length kT/F with a downward force F from thermophoresis and gravitation. We iteratively adapted the surface slip-flow condition to meet Eq. (3) within a relative error of 10%. The flow lines and the thermal gradient for a solution with a particle distance of 4.6 μm are depicted in Fig. 3(c). A simulation of a single particle without nearby surfaces reproduced the analytical drift solution of Ref. [17].

We calculated the total hydrodynamic forces on the surfaces $d\Omega$ of one particle, which is subjected to the fluid flow, induced by a second particle. The x component of the

total hydrodynamic force F_x is given by

$$F_x = \int \left[\eta \mathbf{n} \left(\nabla v_x + \frac{\partial}{\partial x} \mathbf{v} \right) - n_x p \right] d\Omega, \qquad (4)$$

with the pressure p, viscosity η, velocity field $\mathbf{v}$, and normal vector $\mathbf{n}$ [25]. By integrating $F_x(d)$ for a set of particle distances d, we obtained the pseudopotential of the particle attraction $V(d)$. Both the experimentally and theoretically obtained pseudopotentials flatten out into noise levels for distances beyond 8 μm. As shown in Fig. 3(b), the calculated pseudopotential fits the experimentally determined potential in ample detail without fitting parameters. Thus the particle attraction can be quantitatively understood based on the hydrodynamic interaction induced by thermophoretic slip flows.

Discussion.—Particle attraction is not expected from a thermodynamic viewpoint of thermophoresis. As the thermally insulating particles are not heated by laser absorption, we find 100-fold smaller thermal gradients parallel to the surface compared to the perpendicular gradient, as calculated from heat conduction [Fig. 3(c)]. These residual parallel gradients would lead to a minor thermophoretic repulsion for $S_T > 0$ in contradiction with the attractive forces found experimentally.

The reported hydrodynamic attraction differs fundamentally from previously reported experiments [26]. There, thermal convection was externally triggered and particle crowding lead to crystallization. Comparable colloidal crystals from large scale fluid flow were also found at the chamber surface after experiments on thermodiffusion-assisted convection [27]. In contrast, we report particle attraction solely driven by a highly localized flow from the particles under convection-free conditions. The driving mechanism also differs from hydrodynamic attraction in sedimentation [28,29] or during electrophoretic deposition [30–32], where the mutual attraction is predominantly driven by an electro-osmotic fluid flow at the barrier surface [32] rather than on the particle surface. The reported particle attraction in a thermal gradient is likely to disturb thermal field flow fractionation for large particles [18]. Temperature gradients on a surface can be structured by patterning the thermal conductivity of the substrate, allowing for considerable technical applications such as the formation of photonic crystals [33] or biomolecule detection.

Conclusions.—At sufficiently large temperature gradients, we found direct evidence for slip-flow models of thermophoresis. Ballistic thermophoretic drift frustrated by a solid wall leads to interparticle attraction in contrast to thermodynamic expectations. As a result, we were able to create two-dimensional crystals thermally. Marangoni-like slip flow at the particle surface describes the attraction force quantitatively. Our finding argues towards two regimes in thermophoresis depending on the applied temperature gradient.

We thank Ann Fornof and Katja Falter for reading the manuscript. The research was funded by the Emmy Noether program of the Deutsche Forschungsgemeinschaft (DFG) in conjunction with the Nanosystems Initiative Munich (nim).

*dieter.braun@physik.lmu.de

[1] C. Ludwig, Sitz.ber. Akad. Wiss. Wien, Math.-Nat.wiss. Kl. **20**, 539 (1856).
[2] C. Soret, Arch. Sci. **3**, 48 (1879).
[3] S. R. de Groot and P. Mazur, *Non-Equilibrium Thermodynamics* (North-Holland, Amsterdam, 1969).
[4] J. K. G. Dhont, J. Chem. Phys. **120**, 1632 (2004).
[5] J. K. G. Dhont, J. Chem. Phys. **120**, 1642 (2004).
[6] S. Fayolle *et al.*, Phys. Rev. Lett. **95**, 208301 (2005).
[7] S. Duhr and D. Braun, Phys. Rev. Lett. **96**, 168301 (2006).
[8] S. Duhr and D. Braun, Proc. Natl. Acad. Sci. U.S.A. **103**, 19 678 (2006).
[9] R. D. Astumian, Proc. Natl. Acad. Sci. U.S.A. **104**, 3 (2007).
[10] J. K. G. Dhont *et al.*, Langmuir **23**, 1674 (2007).
[11] E. Ruckenstein, J. Colloid Interface Sci. **83**, 77 (1981).
[12] T. Keyes, J. Stat. Phys. **33**, 287 (1983).
[13] J. L. Anderson, Annu. Rev. Fluid Mech. **21**, 61 (1989).
[14] K. I. Morozov, J. Exp. Theor. Phys. **88**, 944 (1999).
[15] M. E. Schimpf and S. N. Semenov, J. Phys. Chem. B **105**, 2285 (2001).
[16] A. Parola and R. Piazza, Eur. Phys. J. E **15**, 255 (2004).
[17] A. Würger, Phys. Rev. Lett. **98**, 138301 (2007).
[18] P. M. Shiundu, G. Liu and J. C. Giddings, Anal. Chem. **67**, 2705 (1995).
[19] J. Rauch and W. Köhler, Phys. Rev. Lett. **88**, 185901 (2002).
[20] D. Braun and A. Libchaber, Phys. Rev. Lett. **89**, 188103 (2002).
[21] M. Braibanti, D. Vigolo, and R. Piazza, Phys. Rev. Lett. **100**, 108303 (2008).
[22] F. M. Weinert *et al.*, Phys. Rev. Lett. **100**, 164501 (2008).
[23] T. M Squires, J. Fluid Mech. **443**, 403 (2001).
[24] D. Rudhardt, C. Bechinger, and P. Leiderer, Phys. Rev. Lett. **81**, 1330 (1998).
[25] L. D. Landau and E. M. Lifshitz, *Fluid Dynamics* (Elsevier Butterworth-Heinemann, Oxford, 2004).
[26] S. Duhr and D. Braun, Appl. Phys. Lett. **86**, 131921 (2005).
[27] R. Cerbino, A. Vailati, and M. Giglio, Phys. Rev. E **66**, 055301 (2002).
[28] T. M. Squires and M. P. Brenner, Phys. Rev. Lett. **85**, 4976 (2000).
[29] J. Bafaluy *et al.*, Phys. Rev. Lett. **70**, 623 (1993).
[30] M. Giersig and P. Mulvaney, Langmuir **9**, 3408 (1993).
[31] M. Trau, D. A. Saville, and I. A. Aksay, Science **272**, 706 (1996).
[32] W. D. Ristenpart, I. A. Aksay, and D. A. Saville, Phys. Rev. E **69**, 021405 (2004).
[33] Y. A. Vlasov *et al.*, Nature (London) **414**, 289 (2001).
[34] See EPAPS Document No. E-PRLTAO-101-036841 for a movie related to Fig. 2. For more information on EPAPS, see http://www.aip.org/pubservs/epaps.html.

Microscale Fluid Flow Induced by Thermoviscous Expansion Along a Traveling Wave

Franz M. Weinert,[1] Jonas A. Kraus,[2] Thomas Franosch,[2] and Dieter Braun[1]

[1]*Applied Physics and Center for NanoScience (CeNS), Department of Physics, Ludwig-Maximilians-Universität München, Amalienstrasse 54, 80799 München, Germany*

[2]*Arnold Sommerfeld Center for Theoretical Physics (ASC) and Center for NanoScience (CeNS), Department of Physics, Ludwig-Maximilians-Universität München, Theresienstraße 37, 80333 München, Germany*

(Received 27 September 2007; published 22 April 2008)

The thermal expansion of a fluid combined with a temperature-dependent viscosity introduces nonlinearities in the Navier-Stokes equations unrelated to the convective momentum current. The couplings generate the possibility for net fluid flow at the microscale controlled by external heating. This novel thermomechanical effect is investigated for a thin fluid chamber by a numerical solution of the Navier-Stokes equations and analytically by a perturbation expansion. A demonstration experiment confirms the basic mechanism and quantitatively validates our theoretical analysis.

DOI: 10.1103/PhysRevLett.100.164501 PACS numbers: 47.15.gm, 47.61.−k, 47.85.−g, 47.85.L−

Spatial confinement of a liquid changes its flow behavior markedly since the importance of surface forces relative to the volume forces increases as the confinement becomes smaller. Recently, flow at the scale of millimeters and below has attracted significant attention, stimulated by the rapid advances to manipulate and to control small-scale devices [1–4]. Since microfluidic flow often is essentially at zero Reynolds number, viscous drag overwhelms the inertial effects of the fluid giving rise to peculiar flow behavior [5,6]. In particular, heat conduction becomes quite efficient, since the thermal diffusivity $\kappa = k/\rho c_p$, with k the thermal conductivity and ρc_p the volumetric heat capacity, implies thermal relaxation times $D^2/\pi^2\kappa$ of the order of 0.1 ms for water confined by walls separated by $D = 10\ \mu$m. Usually, this strong thermal coupling gives rise to a uniform temperature and all physical processes are isothermal. Since pressure effects upon density are negligible if the velocities are small with respect to the speed of sound, fluid flow is essentially ''dynamically incompressible'' [7]; i.e., the velocity field is solenoidal, $\mathrm{div}\vec{v} = 0$.

Recently, it has been noted by Yariv *et al.* [8] that for the case of unsteady heating, this is no longer the case, and one can in principle generate a nonsolenoidal flow. A transient fluid flow emerges due to a thermal expansion of the fluid as a reaction to the heating in combination with the thermal diffusion.

In this Letter, we propose a novel mechanism to generate net flow in a thin fluid chamber, i.e., a viscous liquid confined between two plates separated by a distance of the order of a few micrometers. The driving of the fluid flow is provided by imposing a traveling temperature wave. We show analytically within a thin-film approximation that such unsteady heating leads to net fluid flow. Then, we corroborate our analytic approach by a finite-element calculation. Last, we provide first experimental evidence that there is indeed net flow and that the fundamental dependences have been correctly identified.

The basic mechanism may be summarized as follows: Because of thermal expansion of the liquid, the motion of the heating results in a pressure modulation. The pressure gradients induce a potential flow which, however, does not lead to net fluid flow. Yet, the temperature dependence of the shear viscosity gives rise to a small net mass transport typically opposite to the motion of the heat source. The flow velocity is then proportional to the thermal expansion coefficient of the fluid, $\alpha = \rho_0^{-1}(\partial\rho/\partial T)$, as well as to the thermal viscosity coefficient $\beta = -\eta_0^{-1}(\partial\eta/\partial T)$.

The geometry under consideration consists of a thin chamber of height D and a much larger lateral extension. There is a natural small parameter $\epsilon = D/L \ll 1$, where L is a typical length scale in the lateral direction. Since the film is thin, one expects the Navier-Stokes equations to be dominated only by a few terms. To identify the relevant contributions, dimensionless quantities are introduced as $t = Tt^*$, $v_i = Uv_i^*$, $v_i = vv_\perp^*$, $x_i = Lx_i^*$, $x_\perp = Dx_\perp^*$, $p = Pp^*$. Lateral directions are labeled by the index $i \in \{x, y\}$, whereas the vertical direction is indicated by the subscript $\perp$. To keep all terms in the mass conservation law, the scales are chosen as $v = \epsilon U$, $T = L/U$, and consequently the fluid flow is essentially in-plane. To balance the leading order term in the momentum conservation law, the pressure scale has to be chosen as $P = \eta_0 U/(\epsilon^2 L)$. Momentum transport via convective processes may be ignored from the very beginning since the Reynolds number is small, $\mathrm{Re} = \rho_0 UL/\eta_0 \ll 1$ [9]. Then, the mass conservation law and the momentum balance in perpendicular and lateral direction read to leading order in a *thin-film approximation*, see, e.g., [10–12] (restoring units)

$$\partial_t\rho + \nabla_\perp(\rho v_\perp) + \nabla_i(\rho v_i) = 0, \tag{1a}$$

$$\nabla_\perp p = 0, \tag{1b}$$

$$\nabla_\perp[\eta\nabla_\perp v_i] + \nabla_i p = 0. \tag{1c}$$

As a consequence of the thin-film geometry, (i) bulk vis-

cous processes do not contribute to the leading order equations, (ii) the pressure is homogeneous in the perpendicular direction, (iii) lateral pressure gradients drive the lateral fluid flow. Note that the divergence of the velocity field is irrelevant for the momentum balance but plays a crucial role in the mass conservation law.

The coupling to the temperature enters the equations via the expansion of the fluid as well as by the temperature dependence of the shear viscosity. For the problem at hand, it is appropriate to neglect the mechanical compressibility of the fluid and to expand the equation of state to first order in the temperature field, $\rho = \rho_0(1 - \alpha\delta T)$, where δT is the local temperature change and $\alpha = -(\partial \ln\rho/\partial T)_p$ the thermal expansion coefficient at the reference state (ρ_0, T_0). The density field then is eliminated from the equations of motion in favor of the temperature field δT. A second ingredient for the theoretical model is to include the variation of the shear viscosity with temperature. Introducing the thermal viscosity coefficient $\beta = -(\partial \ln\eta/\partial T)_p$, the coupling reads $\eta = \eta_0(1 - \beta\delta T)$ to first order.

In the case of considerable thermal coupling to the walls, the temperature field approximately reflects the profile of the heat source. The in-plane variations of the temperature field occur on scales λ, $b \gg D$, where λ denotes the wavelength and b the typical lateral extension of the heating. Consequently, the spatial dependence of the density and the shear viscosity is only in-plane as it is inherited from the temperature profile. With this additional assumption, the in-plane momentum balance equation, Eq. (1c), is readily integrated for no-slip boundary conditions at the walls

$$v_i = -\frac{1}{2\eta} z(D - z)\nabla_i p; \tag{2}$$

i.e., the velocity profile corresponds to Poiseuille flow.

Since the spatial dependence of the velocity profiles perpendicular to the wall is known, one may project the three-dimensional problem to the two-dimensional plane by averaging over the vertical z-direction,

$$\bar{v}_i = \frac{1}{D}\int_0^D v_i dz = -\frac{D^2}{12\eta}\nabla_i p. \tag{3}$$

Because the density is assumed to vary only in the lateral direction, the mass conservation law, Eq. (1a), can be directly averaged over the perpendicular direction, $\partial_t\rho + \nabla_i(\rho\bar{v}_i) = 0$, without introducing new terms. The pumping process becomes stationary in the frame of reference comoving with the heat wave, i.e., substituting $\bar{v}_x \mapsto \bar{v}_x - u$, where u denotes the velocity of the heat wave. Then, in the comoving frame, the averaged mass conservation law yields

$$-u\nabla_x\rho + \rho\nabla_i\bar{v}_i = -\bar{v}_i\nabla_i\rho. \tag{4}$$

Here, the velocities $\bar{v}_i$ are small quantities, typically $\bar{v}_i \ll u$. From the closed set of equations, Eqs. (3) and (4), the fluid velocity can be calculated. The temperature profile in the comoving frame enters Eq. (4) in the form of density gradients, $\nabla_i\rho = -\alpha\rho_0\nabla_i\delta T$ and Eq. (3) via the temperature-dependent viscosity. The net flow emerges only if the thermal viscosity coefficient β is nonvanishing. For a temperature-independent viscosity, the pressure acts as a velocity potential, Eq. (3), and averaging along the direction of the wave propagation yields a vanishing net flow.

We exemplify the flow profiles for the case of a Gaussian temperature wave $\delta T(\vec{r}) = \delta T_0 \cos(kx)e^{-y^2/2b^2}$, obtained by a numerical solution of Eqs. (3) and (4) using the FEMLAB®3.1 software package by Comsol. We have used a wavelength $\lambda = 2\pi/k = 50$ μm, a lateral width $b = 7$ μm of the Gaussian modulation, a temperature amplitude of $\delta T_0 = 3.8$ K, and a thermal wave velocity $u = 100$ mm/s. The parameters for $\alpha = 3.0 \times 10^{-4}$ K^{-1}, $\beta = 0.022$ K^{-1} correspond to water at ambient temperature. The parameters have been chosen such that the temperature modulation appears approximately as a train of circular heated areas mimicking the demonstration experiment below. The regions where the temperature gradient is maximal (minimal) act as sources (sinks) for the velocity field, giving rise to a locally dipolar pattern of the fluid flow, see Fig. 1(a). Careful inspection reveals that the velocities in the heated regions are bigger than in the colder ones. The pressure profile is shifted by a quarter of a wavelength reflecting the local expansion of the fluid, Fig. 1(b). The solenoidal part of the velocity field has been obtained as the difference of two FEMLAB calculations for thermal viscosity coefficients $\beta \neq 0$ and $\beta = 0$. Close to the center of the wave, this contribution is directed

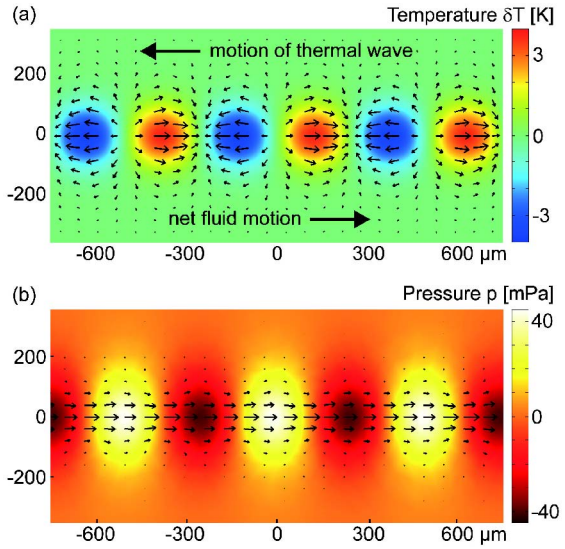

FIG. 1 (color online). Finite-element solution for a temperature wave in the comoving frame. (a) The temperature profile is indicated by the color scale and the arrows refer to the induced velocity flow. (b) The corresponding pressure modulation (color scale) and the solenoidal component of the flow.

opposite to the thermal wave velocity with an average pump velocity $v_{\mathrm{fl}}^{\mathrm{FEM}} = 2.88\ \mu\mathrm{m/s}$ at the center of the thermal wave, whereas far away from the heating, there is a characteristic backflow. The pressures induced by the pumping are below 10^{-6} bar [Fig. 1(b)]. The pressure limitations of the glass chamber used are estimated to 10 bar by a finite element calculation. However, the pressure induced by the pumping increases with the viscosity of the fluid and eventually will stall the pump motion since thermal expansion will deform only the chamber walls instead of triggering fluid motion. So we expect to equally pump fluids with viscosities 10^7 fold higher than water.

To gain further insight, we develop a perturbative analytical solution for the fluid flow appropriate for small temperature changes. Formally, the expansion is performed in the small parameters α and β, and we shall show that net fluid flow first occurs at $\mathcal{O}(\alpha\beta)$. The quiescent fluid $v_i \equiv 0$, $p = p_0$ solves the governing equations to zeroth order in α, β, i.e., if all couplings to the temperature field are ignored. To leading order in α, the term on the r.h.s. of Eq. (4) is of second order and may be ignored. Similarly, (3) is expanded to first order in the temperature change

$$\bar{v}_i = -\frac{D^2}{12\eta_0}(\nabla_i p)(1 + \beta\delta T). \tag{5}$$

Already at this point, one concludes that to order $\mathcal{O}(\beta^0)$, the velocity corresponds to potential flow only; hence, no net pumping arises to that order. The leading order to the pump velocity is then expected to be of order $\mathcal{O}(\alpha\beta)$. To identify the net fluid motion, it is favorable to introduce the velocity potential, χ, and the stream function, ψ, via $\bar{v}_x = \nabla_x\chi + \nabla_y\psi$, $\bar{v}_y = \nabla_y\chi - \nabla_x\psi$. From Eq. (5), one infers that the leading term corresponds to pure gradient flow, i.e., $\chi = -(D^2/12\eta_0)p$, where $\chi(\vec{r})$ denotes the velocity potential and $\vec{r} = (x, y)$. To the required order, χ is determined by combining Eqs. (4)

$$\nabla^2\chi(\vec{r}) = -\alpha u\nabla_x\delta T(\vec{r}) + \mathcal{O}(\alpha^2). \tag{6}$$

Once the velocity potential is determined, the stream function is calculated by extracting from $\beta\delta T(\vec{r})\nabla_i\chi(\vec{r})$ its solenoidal component. By Helmholtz's decomposition theorem, the stream function satisfies a Poisson equation

$$-\nabla^2\psi = \nabla_x(\beta\delta T\nabla_y\chi) - \nabla_y(\beta\delta T\nabla_x\chi). \tag{7}$$

The lowest order contribution to the stream function is thus proportional to $\alpha\beta$, which also sets the overall scale of the thermomechanical effect. Furthermore, one infers from Eq. (7) that a strictly one-dimensional temperature modulation does not give rise to solenoidal flow. The remaining task is to solve the set of Poisson equations, which can be easily implemented by numerical methods. To determine the average flow for a travelling periodic temperature wave train of wavelength λ, it is actually sufficient to know the velocity potential,

$$v_{\mathrm{fl}}(y) \equiv \frac{1}{\lambda}\int_0^\lambda dx\bar{v}_x(\vec{r}) = -\frac{1}{\lambda}\int_0^\lambda dx\chi(\vec{r})\beta\nabla_x\delta T(\vec{r}), \tag{8}$$

where the last relation follows from the representation, Eq. (5) and an integration by parts.

To illustrate the physics, we consider a Gaussian temperature wave $\delta T(\vec{r}) = \delta T_0\cos(kx)e^{-y^2/2b^2}$, where b characterizes the lateral width of the wave train. The Poisson equation, Eq. (6), can be solved exactly in terms of the error functions [13]; however, it is instructive to construct an approximate solution for wide waves, $kb \gg 1$. Then the problem is effectively one-dimensional, and χ depends on the lateral coordinate y only parametrically. One readily calculates $\chi = -u\alpha\delta T_0\sin(kx)e^{-y^2/2b^2}/k$, implying a net fluid motion

$$v_{\mathrm{fl}}(y) = -u\alpha\beta(\delta T_0)^2\exp(-y^2/b^2)/2, \tag{9}$$

typically opposite to the motion of the traveling temperature wave. Since by assumption the changes in the density and the viscosity are small, the net fluid motion is much slower than the velocity of the temperature wave, $v_{\mathrm{fl}} \ll u$.

We have confirmed the predicted fluid movement in a demonstration experiment. A circular variant of a thermal wave is imposed with infrared light to a thin fluid film, see Fig. 2. The fluid movement is recorded using micrometer-sized fluorescent particles, and the thermal wave is imaged stroboscopically with temperature-sensitive fluorescence. Within experimental errors, the theory captures the thermally triggered net flow.

The details of the experiment are as follows: A fiber laser at 1455 nm and a maximal power of 5 W (RLD-5-1455, IPGLaser) is deflected by an acousto-optical deflector (Pegasus Optik, AA.DTS.XY.100) and moderately focused from below (Thorlabs, C240TM-C, $f = 8$ mm, NA = 0.5) to a 10 μm thin fluid film sandwiched between sapphire windows. The light is absorbed by water with an attenuation length of 305 μm. The chamber is imaged from above by a fluorescence microscope (Zeiss, Axiotech Vario) and a CCD camera (SensiCam QE,

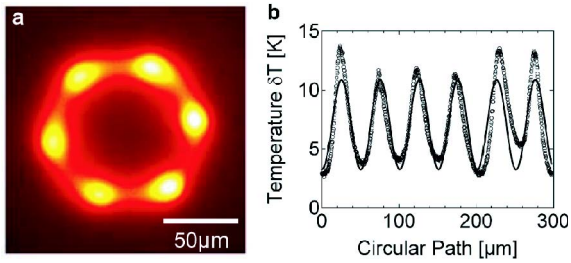

FIG. 2 (color online). Demonstration experiment. (a) A circular thermal wave is created in water by a moving focus of an infrared laser. The temperature is inferred by stroboscopic imaging of a temperature-sensitive fluorescent dye. (b) Peak temperature along the circumference. A sinusoidal fit yields a temperature amplitude of $\delta T_0 = 3.8 \pm 0.5$ K.

PCO). The illumination is provided by a green LED (LXHL-LX5C, Luxeon) which for the temperature imaging was modulated with a bandwidth of 150 kHz using a laser current source (LD-3565, ILX Lightwave). The temperature field was imaged using 50 μM of the fluorescent dye BCECF under stroboscopic illumination [14,15] to determine the temperature amplitude of the thermal wave.

The thermal wave is generated by a scanning laser spot. Six individual temperature peaks are created by a circular pattern of radius $R = 50$ μm with a base frequency of 30 kHz. The frequency is faster than the thermal relaxation time, which is dominated by the vertical heat currents and determined to 0.21 ms using a finite-element calculation. A thermal wave of six points is generated, measured in Fig. 2. The points are rotated using a slower shift frequency $f_S = 0.2 \ldots 2$ kHz. The result is a circular thermal wave with velocity $u = f_S \times 2\pi R/6 = 10 \ldots 100$ mm/s.

Fluid velocities are measured by single particle tracking of 80 pM of 1 μm diameter silica beads (PSi-G1.0, Kisker). Particle velocities could be well discriminated from Brownian diffusion by tracking 5 independent particles over 10 μm with a positional error of 1 μm. The peak velocity of the parabolic flow profile was measured by selecting the beads in the chamber center. The experimental values were multiplied by $2/3$ to compare with the chamber-averaged theoretical values. Optical trapping or thermophoresis would move the tracer particles with the thermal wave, opposite to the observed flow direction. Under the experimental conditions, both effects would yield similar attractive forces. However, control experiments in heavy water with its 100-fold decreased absorptive heating only revealed moderate attraction into the illuminated ring, but no pumping movement along it (< 0.13 μm/s). This indicates that the particles are ideal tracers of the fluid motion at the used focus size [15].

With the above described temperature pattern and a thermal wave velocity of $u = 100$ mm/s, we measure a peak fluid flow of $v_{\mathrm{fl}}^{\mathrm{exp}} = 2.7 \pm 0.5$ μm/s. We expect from the wide wave solution, Eq. (9), a fluid velocity of $v_{\mathrm{fl}}^{\mathrm{theo}} = 4.77$ μm/s. Applying the complete analytical solution [13] or the FEMLAB result yields $v_{\mathrm{fl}}^{\mathrm{FEM}} = 2.88$ μm/s which describes the experimental result quantitatively.

Two parameter variations further confirm the theoretical model (Fig. 3). The dependence on the temperature amplitude δT_0 exhibits a parabolic dependence [Fig. 3(a)] as expected theoretically by Eq. (9). Furthermore, the fluid velocity scales linearly with the velocity u [Fig. 3(b)] of the thermal wave as predicted (solid lines). We therefore find experimentally that a circular thermal wave triggers a fluid flow according to the theoretical description.

To conclude, we showed that a thermal wave can move a fluid by the nonlinear combination of the temperature-dependent density and viscosity. While the obtainable fluid velocities are small at present, future improvements could allow microfluidic applications.

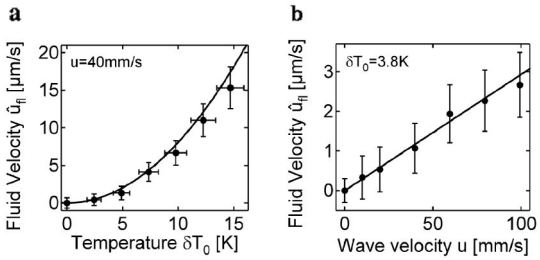

FIG. 3. Experiment versus theory. (a) The fluid velocity scales quadratically with the amplitude of the thermal wave δT_0. (b) The speed increases linearly with the velocity u of the thermal wave. Measurements are given as dots, the theory as solid lines with the geometrical prefactor determined in Ref. [13]. Error bars are standard errors.

We thank Joseph Egger for initial discussions. F. M. W. and D. B. were supported by the DFG. Support by the Nanosystems Initiative Munich (NIM) is gratefully acknowledged.

[1] H. A. Stone, A. D. Stroock, and A. Ajdari, Annu. Rev. Fluid Mech. **36**, 381 (2004).
[2] G. M. Whitesides, Nature (London) **442**, 368 (2006).
[3] T. M. Squires and S. R. Quake, Rev. Mod. Phys. **77**, 977 (2005).
[4] T. Thorsen, S. J. Maerkl, and S. R. Quake, Science **298**, 580 (2002).
[5] J. Happel and H. Brenner, *Low Reynolds Number Hydrodynamics* (Kluwer, The Hague, 1983).
[6] G. K. Batchelor, in *Theoretical and Applied Mechanics*, edited by W. Koiter (Elsevier North Holland, The Netherlands, 1977), pp. 33–55.
[7] G. K. Batchelor, in *An Introduction to Fluid Dynamics* (Cambridge Univers. Press, Cambridge, 1967).
[8] E. Yariv and H. Brenner, Phys. Fluids **16**, L95 (2004).
[9] The dimensionless number quantifying the relative importance of convective to viscous terms for a thin-film geometry is actually even smaller $\mathrm{Re}^* = \rho_0 U h^2/L\eta_0$ [10].
[10] L. G. Leal, in *Laminar Flow and Convective Transport Processes*, edited by H. Brenner (Butterworth-Heinemann, Boston, 1992).
[11] A. Oron, S. H. Davis, and S. G. Bankoff, Rev. Mod. Phys. **69**, 931 (1997).
[12] S. B. G. O'Brien and L. W. Schwartz, in *Encyclopedia of Surface and Colloid Science* edited by A. T. Hubbard (Dekker, New York, 2002), p. 5283.
[13] J. A. Kraus, Diploma thesis, LMU München, 2007.
[14] S. Duhr, S. Arduini, and D. Braun, Eur. Phys. J. E **15**, 277 (2004).
[15] S. Duhr and D. Braun, Proc. Natl. Acad. Sci. U. S. A. **103**, 19678 (2006).

Optically driven fluid flow along arbitrary microscale patterns using thermoviscous expansion

Franz M. Weinert and Dieter Braun[a)]
Systems Biophysics, Functional NanoSystems, Center for Nanoscience (CENS), Department of Physics, Ludwig-Maximilians University Munich, Amalienstr. 54, 80799 Munich, Germany

(Received 25 June 2008; accepted 8 October 2008; published online 25 November 2008)

We show how fluid can be moved by a laser scanning microscope. Selected parts of a fluid film are pumped along the path of a moving warm spot which is generated by the repetitive motion of an infrared laser focus. With this technique, we remotely drive arbitrary two-dimensional fluid flow patterns with a resolution of 2 μm. Pump speeds of 150 μm/s are reached in water with a maximal temperature increase in the local spot of 10 K. Various experiments confirm that the fluid motion results from the dynamic thermal expansion in a gradient of viscosity. The viscosity in the spot is reduced by its enhanced temperature. This leads to a broken symmetry between thermal expansion and thermal contraction in the front and the wake of the spot. As result the fluid moves opposite to the spot direction due to both the asymmetric thermal expansion in the spot front and the asymmetric thermal contraction in its wake. We derive an analytical expression for the fluid speed from the Navier–Stokes equations. Its predictions are experimentally confirmed without fitting parameters under a number of different conditions. In water, this nonlinearity leads to a fluid step of $<$100 nm for each passage of the spot. Since the spot movement can be repeated in the kilohertz regime, fluid speeds can exceed 100 μm/s. Using this technique, we pump nanoparticles over millimeters through a gel. An all-optical creation of a dilution series of DNA and biomolecules by aliquotation and mixing is demonstrated for fluids sandwiched between untreated and unstructured, disposable microscope cover slips. The shown optical remote control of fluid flow expands the microfluidic paradigm into previously inaccessible regimes of tiny volumes, closed flow paths, fast switching between flow patterns, and remote fluid control under extreme fluid conditions. © *2008 American Institute of Physics*. [DOI: 10.1063/1.3026526]

I. INTRODUCTION

The defined control of fluid flow on the microscale is the basis for several applications in chemistry and biology[1–5] and plays an important role in scaling biosensing applications down to the scale of single cells. The aim is to find a defined control of volumes comparable to the size of biological systems. This miniaturization is expected to shorten the time of the experiment, to enhance the signal to noise ratio of detection and to reduce the overall consumption of chemicals. In the past, several ways to remotely switch valves in micromanufactured channels for the control of fluid flow in channels have been explored.[6–10] Optical methods have been investigated to move covered liquid droplets[11,12] or to drive liquid flow by holographically induced vortex flows near trapped particles.[13] Lithographic surface patterning is used to induce droplet movement by thermocapillary actuation[14] or surface acoustic waves.[15] Here we propose an optical remote driving and random access control of two-dimensional liquids without surface patterning or the usage of special substrates.

Today, pressure is the dominating paradigm to drive flow along microscale channels. However, its control suffers from hysteresis effects and requires macroscale connections to outside pumps and controllers. An interesting aspect of the presented method is its complementary approach as compared to contemporary microfluidics. Our technique neither requires walls to define the fluid motion nor needs channels with external pressure control to drive the fluid flow by pressure and does not rely on valves to switch between pump paths. We drive fluids highly locally, contact-free, and all optical. This allows to move fluids along paths which are arbitrarily defined without channel walls. We believe that the high reproducibility of optical techniques and the fact that the pump velocity enhances for thinner fluid films open a range of unexpected applications of the approach and point towards reliable nanofluidic designs.

The ability to remotely control matter with light has unique advantages. In many fields of physics and biology, optical control of matter is used due to its versatility and precision and has had a major impact on experimental methods. For example, optical traps allowed to cool and isolate single atoms in vacuum in a wide variety of geometries. Furthermore, optical tweezers[16–18] have been employed to grab and move objects on the microscale under physiological conditions. In the reported experiments, we expand the optical control paradigm to the continuum mechanics regime. Instead of controlling the movement of objects with optical contrast, we describe the arbitrary optical control of a homogeneous fluid film. We can realize arbitrary solutions of the

[a)]Author to whom correspondence should be addressed. Electronic mail: dieter.braun@physik.lmu.de.

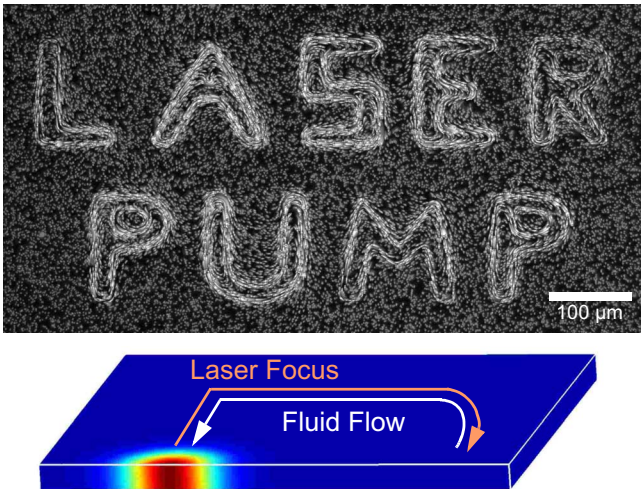

FIG. 1. (Color online) Pumping water optically along arbitrary patterns. Fluid flow along the letters "LASER PUMP" is driven by dynamically heating a thin fluid film with a laser scanning microscope. As seen, complex flow patterns are easily accomplished. No channels restrict the fluid flow. Local pumping of the fluid film is the result of thermoviscous fluid movements for each passage of the laser focus. We visualize the water flow by fluorescent tracer particles. Movies of flow patterns can be found in the supplementary materials section.

two-dimensional Navier–Stokes equation with a resolution of a few micrometers and velocities on the order of 100 μm/s.

Using the nonlinear effect described here, we can, for example, move water along the letters "LASER PUMP" without lateral walls to guide the flow (Fig. 1). In the example, we sandwich a 10 μm thin sheet of water between glass slides and move an infrared laser focus along the letters with a laser scanning microscope. The water is locally heated by direct absorption of the laser irradiation. The spot movement along the letters is repeated in the kilohertz regime. As result, the fluid flows the reverse path of warm spot movement. In the following we describe the theoretical basis of the effect, derive an expression for the pump velocity, test the expression in various experiments, and end with discussing the prospects and limitations of the approach.

II. EXPERIMENT

A. Optical setup and imaging

The infrared laser scanning microscope is operated with a fiber laser (RLD-5-1455, IPGLaser, 5 W) at wavelength of 1455 nm, collimated to a $1/e^2$ diameter of 1.5 mm (F240FC-1550, Thorlabs). Water absorbs this wavelength strongly with an attenuation length of 305 μm. The absorbed light power ranged in intensity from 1 to 100 mW. An acousto-optical deflector (Pegasus Optik, AA.DTS.XY.100) modulated and moved the laser spot, which was focused into the fluid chamber from below with a long distance lens [Thorlabs, C240TM-C, focus length $f=8$ mm, numerical aperture NA=0.5, $NA_{eff}=0.07$]. For experiments with small spot diameters (Fig. 5) we focused the beam using a lens with high NA (Thorlabs, C570TM-C, $f=2.84$ mm, $NA_{eff}=0.2$). Imaging was provided by an upright fluorescence microscope (Zeiss, Axiotech Vario) from the top. For illumination, a green light emitting diode (LXHL-LX5C, Luxeon) was driven with a current source (LD-3565, ILX Lightwave, modulation bandwidth of 100 kHz).

Flow velocities were measured by tracing 80 pM of green fluorescent 1 μm diameter silica microspheres (PSi-G1.0, Kisker, Germany) which showed negligible optical trapping at the used focus size. This was tested with heavy water with 100-fold lower light absorption, which should show similar optical trapping. Under otherwise identical conditions, no optical trapping and no movement of the particles were found, indicating that optical trapping or other optical forces due to the focused laser light play no role. Optical trapping would move the tracer particles towards the laser spot movement, opposite to the observed flow direction. Tracking resolution was typically 100 nm. We used a circular pump geometry with a radius of 60 μm to measure the velocities.

Temperatures were imaged using 50 μM of the fluorescent dye 2′,7′-bis(carboxy-ethyl)-5(6)-carboxyfluorescein (Molecular Probes) in 10 mM tris(hydroxymethyl) aminomethane hydrochloride buffer at *p*H 7.8. The fluorescence depends on temperature and was translated to chamber-averaged temperatures with a sensitivity of $-0.013/\mathrm{K}$.[19] The shape and temperature of the moving spot were imaged stroboscopically with a 10 μs long rectangular light pulse each time the laser spot passed by. The flow was imaged by averaging over subsequent image differences. The tracer particles were solved in 75% (v/v) glycerol/water to enhance the flow contrast by suppressing diffusion.

B. Chambers and light driven microfluidics

If not indicated explicitly, the chamber thickness was 6.5 μm. The chamber thickness was measured by focusing the top and the bottom of the chamber with a calibrated *z* drive. For Fig. 8, a 45 °C warm, 2 μl drop of low melting agarose gel (A3038, Roth Laborbedarf) was sandwiched between two glass slides. After gelation by cooling to room temperature, a 120 nM solution of 40 nm beads in water (F8795, Molecular Probes) were pipetted at the edge of the cover slide. Capillary forces pulled the liquid inside and formed an interface towards the gel. The chamber height was 10 μm. The gel was initially molten with a low repetition rate ($f=1$ Hz), while the fluid was pumped along the trace at $f=50$ Hz.

In Fig. 9, the preparation for the gel interface additionally required to further suppress the diffusion of the small biomolecules by the addition of 66% saccharose to the gel.

For Fig. 10, two droplets of 2% low melting agarose gel in 10 mM TRIS buffer together with 60 vol % of saccharose were put on a 45 °C warm silicon wafer. The silicon wafer was polished on both sides and had 1000 nm of SiO_2 with 40 nm CrNi (20% Cr and 80% Ni) evaporated on top which increased the infrared absorption 15-fold. The infrared laser was fed through the silicon chip which is transparent at this wavelength. After covering the liquid gel with a glass slide, both fluids spread into the air-filled chamber space, forming an interface between each other. In the gel at the bottom of the image, 100 μM of a 30 kDa dextran with a fluorescein

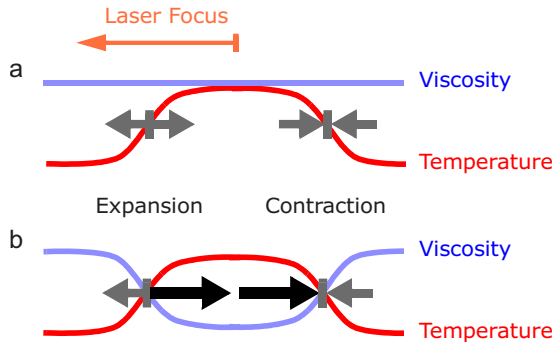

FIG. 2. (Color online) Basic mechanism for pumping fluid with a moving laser focus. (a) A warm temperature spot moving to the left generates thermal expansion in its front and contraction in its wake, shown with dark gray arrows. These local fluid movements cancel out each other at constant viscosity. (b) The temperature dependency of the fluid's viscosity breaks this symmetry and results in a net liquid flow to the right (black arrows). If the fluid expands upon heating and shows a decreased viscosity, this flow is directed against the movement of the spot as indicated by the black arrows.

dye (D1844, Molecular Probes) was dissolved. Before the fluid was pumped with repetition rate $f=3$ kHz, the spot was moved at $f=0.5$ kHz for 0.8 s to melt the pump channels into the gel. The gelation is kinetically hindered and subsequent pumping can be performed at reduced temperature in the premolten, stable channel structures. The overall protocol time was 15 s.

C. Finite element calculations

Finite element calculations were performed using the industrial Comsol FEMLAB 3.1 solver. The Navier–Stokes equations were calculated in various geometrical settings and different stages of approximation, typically in the comoving frame of the warm spot. The simulation files are provided as supplemental material.[20]

III. RESULTS AND DISCUSSION

A. Basic mechanism

We sketch the basic physical principles in Fig. 2 before we enter a detailed theoretical treatment. Let us consider a moving warm spot of enhanced temperature that moves to the left [Fig. 2(a), red]. At its front, the fluid is heated. In its wake it cools down again. The heating triggers thermal expansion and thus a diverging fluid flow in the front of the spot (gray arrows). The fluid contracts again upon cooling in the wake of the spot. For a constant viscosity, both movements are antisymmetric and cancel out each other.[21] However, since the viscosity of the fluid typically drops with temperature, the expansion and contraction movements take place in a gradient of viscosity [Fig. 2(b), blue] and lead to a net fluid movement to the right. Qualitatively, the net flow results from the fact that thermal expansion feels less friction to the solid walls when it moves fluid towards than away from the spot. Due to the sign change of the viscosity gradient at the front as compared to the wake of the spot, we find a net fluid movement to the right from both expansion and contraction (black arrows).

For extended thermal waves we have discussed a similar effect in the past.[22] However, here we found that the movement of a single focus spot gives a much simpler implementation of the effect. Furthermore, with a single spot we can reach pump velocities exceeding 150 μm/s for maximal spot temperatures of $\Delta T_0=10$ K above the background chamber temperature. Under these conditions, thermal waves could only trigger a fluid flow of 5 μm/s along a circular geometry.

B. Analytical solution

The above qualitative illustration can be derived quantitatively from first principles. Let us consider the stationary solutions of the Navier–Stokes equations:

$$-\rho\frac{\partial \mathbf{u}}{\partial t}-\rho(\mathbf{u}\cdot\nabla)\mathbf{u}+\nabla\cdot\eta[\nabla\mathbf{u}+(\nabla\mathbf{u})^T]=\nabla p,$$

$$\frac{\partial\rho}{\partial t}+\nabla\cdot(\rho\mathbf{u})=0, \tag{1}$$

in the moving frame of the temperature spot. Variables are the fluid velocity $\mathbf{u}=(u,v,w)$ for the x, y, and z directions. The velocity of the warm spot along the x direction is denoted by u_{spot}, the pressure by p, density by ρ, and viscosity by η. We describe the fluid flow in the frame of the temperature spot which moves along the x axis with a temperature increase of $\Delta T=\Delta T(x-tu_{\text{spot}},y)$. Due to stationarity, the time derivatives $\partial u/\partial t$, $\partial v/\partial t$, and $\partial\rho/\partial t$ are replaced by convective terms $-u_{\text{spot}}u_x$, $-u_{\text{spot}}v_x$, and $-u_{\text{spot}}\rho_x$ in the moving frame. Furthermore the lubrication approximation for thin films is used as follows. The velocities u and v describe the average film velocity along the x and y axes. Assuming a parabolic fluid profile, friction terms $12u\eta/d^2$ and $12v\eta/d^2$ arise from the integration over the film in the z direction with d being the fluid thickness. With the nomenclature $u_x=\partial u/\partial x$, the momentum balance of the Navier–Stokes equations becomes

$$\rho u_{\text{spot}}u_x-\rho(uu_x+vu_y)=\frac{\partial}{\partial x}[p-2\eta u_x]-\frac{\partial}{\partial y}[\eta(u_y+v_x)]+12(u+u_{\text{spot}})\eta/d^2,$$

$$\rho u_{\text{spot}}v_x-\rho(uv_x+vv_y)=-\frac{\partial}{\partial x}[\eta(v_x+u_y)]+\frac{\partial}{\partial y}[p-2\eta v_y]+12v\eta/d^2. \tag{2}$$

The inertial terms on the left side of Eq. (2) are negligible due to a small Reynolds number of typically around $\mathrm{Re}=0.02$. One can assume that thermal expansion is equilibrated since the speed of sound in water (1400 m/s) is much faster than the movement of the laser spot ($u_{\text{spot}}=0.2$ m/s). As result, we do not explicitly implement the expansion dynamics with an equation of state for water but we insert the change in density directly into the continuity equation using $\rho=\rho_0(1-\alpha\Delta T)$ with the thermal expansion coefficient $\alpha=(1/\rho)(\partial\rho/\partial T)$. Inserting the convective terms and the thermal expansion term $\rho_x(u+u_{\text{spot}})=\rho_0\alpha u_{\text{spot}}\Delta T_x+\rho_x u_{\text{spot}}$ we find for the continuity equation

$$\rho(u_x+v_y)+\rho_0\alpha u_{\text{spot}}\Delta T_x+\rho_y v=0. \tag{3}$$

We assume that the temperature spot is wider than the thickness of the water film ($d=10\ \mu$m). Thus friction within the fluid layer becomes smaller than the friction towards the boundaries of the film: $\eta v_{xx} \ll 12 v\eta/d^2$. As seen above, the change in density only plays a role in the $\rho_x u$ term. For all other terms, we keep the density constant and substitute with $\rho \to \rho_0$. We checked numerically that the dynamics in the y direction does not contribute to the final pump velocity. Since the fluid flow from thermal expansion is much slower than the spot velocity ($v \ll u_{\text{spot}}$) we can drop the term $\rho_y v$. We can now transfer back to the resting frame of reference of the chamber walls with $u+u_{\text{spot}} \to u$. As a result, Eqs. (1) and (2) are greatly simplified mostly due to the treatment with low Reynolds numbers:

$$p_x + 12u\eta/d^2 = 0,$$

$$p_y + 12v\eta/d^2 = 0,$$

$$u_x + v_y + \alpha u_{\text{spot}} \Delta T_x = 0. \tag{4}$$

To apply the identity $p_{xy}=p_{yx}$, we combine the two top momentum equations by subtracting the y derivative of the first from the x derivative of the second, leading to $(u_y - v_x)\eta + u\eta_y - v\eta_x = 0$. No net pumping perpendicular to the spot movement (y direction) is expected since thermal expansion and thermal contraction are located in an equal gradient of the viscosity. Only along the x direction thermal expansion faces a gradient of viscosity which is inverted upon later thermal contraction. We thus drop all terms with velocity v and find

$$u_y \eta + u\eta_y = 0,$$

$$u_x + \alpha u_{\text{spot}} \Delta T_x = 0. \tag{5}$$

We make the viscosity temperature dependent with $\eta = \eta_0(1-\beta\Delta T)$ and temperature coefficient $\beta = (1/\eta)(\partial\eta/\partial T)$. The second line can be readily integrated along x and inserted into the first, leading to $u_y + \alpha\beta u_{\text{spot}} \Delta T \Delta T_y = 0$ which is again readily integrated along y to yield

$$u = -\frac{\alpha\beta}{2} u_{\text{spot}} \Delta T^2. \tag{6}$$

We move the spot repeatedly over the same location with frequency f. Each passage of the spot makes the fluid center shift by Δx. This shift can be inferred from the integration of the peak fluid velocity $3u/2$ over time for a full passage of the warm spot. The peak fluid velocities can be inferred from average fluid velocities by multiplying with a factor of $3/2$ due to the parabolic flow profile along the z direction:

$$u_{\text{flow}} = f\Delta x = \frac{3f}{2}\int_{-\infty}^{\infty} (u + u_{\text{spot}})dt = \frac{3f}{2}\int_{-\infty}^{\infty} \frac{u + u_{\text{spot}}}{u_{\text{spot}}} dx. \tag{7}$$

The time integral is transformed to the space coordinates of a fixed frame of reference with the substitution $dx/dt = u_{\text{spot}}$. For thermal spot velocities slower than the thermal equilibration time, dynamic heating and cooling do not deform the temperature spot geometry and we can assume a Gaussian temperature distribution $\Delta T = \Delta T_0(y)\exp[-(x-u_{\text{spot}}t)^2/(2b^2)]$ with spot width b. Only for faster velocities do we find experimentally by imaging the temperature spot with stroboscopic illumination that the lagging cooling in the wake of the spot creates an asymmetric temperature spot. In these cases, adapted temperature distributions were used to describe the experimental results. Notably, the temperature changes by less than 15% along the z axis according to steady state calculations of the heat equation with the respective water and glass materials. Therefore, although a drop in the z direction towards the chambers is necessary to cool the water, it has a minor contribution to the resulting pump velocity. For the case of a Gaussian temperature distribution without z dependence, we find a flow velocity of

$$u_{\text{flow}} = -\frac{3\sqrt{\pi}}{4} f\alpha\beta b \Delta T_0^2. \tag{8}$$

For other shapes of the temperature spot, the prefactor from the integration will change. The negative sign indicates that for positive α and β the flow velocity u is directed oppositely to the spot movement. So we have found that pumping is only found for nonzero thermal expansion ($\alpha \neq 0$) and a temperature dependent viscosity ($\beta \neq 0$). The fluid velocity u_{flow} depends linearly on the repetition rate f of the spot movement. It raises quadratically with the applied temperature increase ΔT_0, as expected by combining linear expansion with a linear temperature dependent viscosity. Apparently the thickness of the water film does not enter Eq. (8) which is also found experimentally for small repetition frequencies f. However, only for thin chambers can the temperature spot be moved at high repetition rates f without deformation of the geometry of the temperature field, which makes the method most effective for chamber sizes below about 50 μm.

We insert numbers for water. The thermal parameters at room temperature are $\alpha = 3.3\times10^{-4}/\text{K}$ and $\beta = 0.021/\text{K}$. With a spot frequency of $f=5$ kHz, a width of the temperature spot $b=27\ \mu$m, and a peak temperature $\Delta T_0 = 9$ K, we find from Eq. (8) a peak flow velocity of $u_{\text{flow}} = 100\ \mu\text{m/s}$. We applied the above conditions in an experiment inside a $d=6.5\ \mu$m thin film of water. We find a peak flow velocity of $u_{\text{flow}} = 95\ \mu\text{m/s}$, in good agreement with the theoretical model.

C. Numerical solution

The above analytical solution was checked against the numerical solution of Eqs. (2) and (3) using a commercial finite element solver program (Comsol, FEMLAB) in both three and two dimensions (Fig. 3). The boundary conditions imposed fluid velocity in accordance to the moving frame of reference. From the left ($-x$), the fluid flow is introduced with $u=-u_{\text{spot}}$ and freely flows out of the simulated area on the right side (x) with a pressureless outflow boundary condition. The top ($+y$) and bottom ($-y$) boundaries are kept neutral at a sufficient distance to not hinder the flow dynamics around the spot. Results are plotted by adding the spot velocity u_{spot} to the calculated flow field to show the fluid

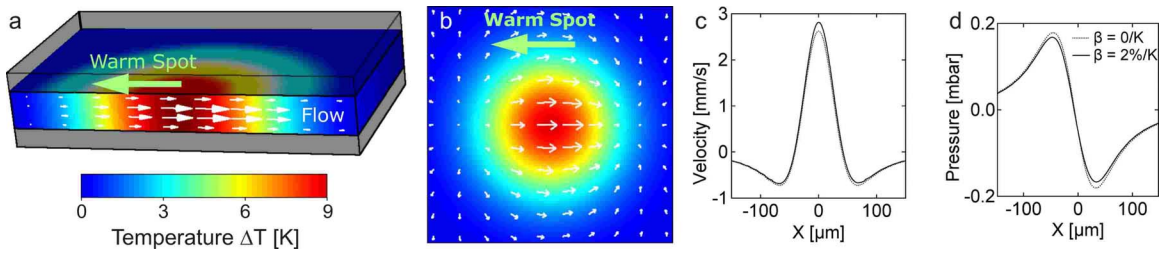

FIG. 3. (Color online) Numerical finite element calculation of thermoviscous pumping. (a) A temperature spot (color coded), is moving to the left and results in an expansion in its front (left) and a contraction in its wake (right). The resulting fluid flow to the right is calculated in three dimensions and indicated by white arrows. The resulting flow has a parabolic flow profile, allowing its description with a thin film approximation. (b) Pumping velocities calculated using the thin film approximation in two dimensions. The average velocity is viewed from top and calculated in the coordinate system of the moving spot. The fluid flow is shown as white arrows, color coded is the temperature $\Delta T(x,y)$. [(c) and (d)] Velocity and pressure profile in the spot along the x-axis. The integral over the velocity is only nonzero for $\beta \neq 0$ due to extended tails in the positive and negative x-directions. The pressure profile is positive in front of the spot as result of the thermal expansion and negative in its wake. Friction reduces for $\beta \neq 0$. Calculations were made using FEMLAB. The simulation files can be found in the supplementary materials.

flow in the resting frame of the chamber. Additional simulation parameters were the density $\rho_0 = 1000\ \mathrm{kg/m^3}$ and the viscosity $\eta_0 = 0.64 \times 10^{-3}$ Pa s for water at room temperature. The numerical calculation allowed to confirm the applied approximations in detail.

The numerical solution for the velocity around the focus is plotted in three dimensions in Fig. 3(a) and in two dimensions in Fig. 3(b). The spot is moving from right to left. In both simulations we find that the fluid expands in the front of the spot and contracts in the tail on the right side of the temperature spot. A parabolic flow profile can be found in the three dimensional solution, confirming the lubrication approximation used in the analytical treatment. As seen by the white arrows, the fluid is pumped across the warm spot by thermal expansion in the front of the spot and thermal contraction in its back. We plot the velocity in the center of the spot along the x axis in Fig. 3(c). Due to large tails of negative velocity for large absolute values of x, the integral over the velocity vanishes if the viscosity is kept constant with $\beta = 0$ (dashed line). This is expected since the simple movement of an expansive spot does not lead to a net fluid movement. Only for temperature dependent viscosity with $\beta \neq 0$ do we find a net movement through the spot. The velocities, however, increase only slightly for $\beta = 0.02\ \mathrm{K}^{-1}$ as plotted by the solid line. This slight increase accounts for all of the found net fluid velocity. Pumping of course does not violate the momentum balance as any momentum required to move the liquid is coupled by the temperature dependent friction to the bordering glass windows. So if pumping is switched on, momentum change of the liquid will result in a tiny momentum transfer to the chamber walls.

In Fig. 3(d) we show the calculated pressure p along the x axis, with $\beta = 0$ (dashed) and $\beta = 0.02\ \mathrm{K}^{-1}$ (solid). For the latter, we find a lower pressure due to a lower friction $F \propto \eta_0(1 - \beta \Delta T)$ in the warm spot to the walls. Since the pump flows are localized to the micrometer-sized temperature spot, the maximal pressure to drive the fluid is below 0.2 mbar for above described parameters in water. This is at least five orders of magnitude below the typical pressure limitations for microfluidics which are on the order of several tens of bars. To calculate a pressure limit, we calculated the deformation for the used 170 μm thin glass material. The pressure needed to bend the glass at the spot to make room for only 10% of the additional volume from a thermal expansion by $\Delta T = 10$ K in a 10 μm chamber amounts to 240 bar (see finite element calculation in the supplementary material[20]). This comparably large pressure limit is mainly the result of the microscale spot area across which the pressure is applied. Notably, this pressure is still well below the internal pressure of water itself. Compressibility models of water typically assume that water becomes compressible upon approaching a pressure of 20 kbar.

The wavelength of the infrared laser used for heating is chosen such that it is absorbed by the water, not by the surrounding glass chamber materials. Therefore, the thermal relaxation of a micrometer thin layer of water bordered by glass windows is below the millisecond time scale. For example, the relaxation time of a 10 μm thin water sheet is on the time scale of 0.1 ms as approximated from thermal diffusion by $\tau = d^2/(\pi^2 \kappa)$ with the thermal diffusivity $\kappa = k/(c_P \rho)$, the thermal conductivity k, the heat capacity c_P, and the density ρ. Thus for spot repetition rates below 1 kHz, a Gaussian temperature profile is a good approximation. Only for faster laser spot movements, the temperature focus shows an asymmetric shape due to a delayed cooling in the tail. As noted before, pump velocities under such asymmetric spot geometries can be equally described by Eq. (8) with an adapted, asymmetric temperature profile.

An asymmetric temperature profile is not necessary to pump the water sheet. One could argue that the laser is deflected by the thermal lensing of the asymmetric spot and as a result, the light transfers momentum due to the deflected beam and pumps the liquid. However, an estimation shows that this effect would be three orders of magnitude smaller than the observed pump velocities. This model would not explain pumping from a symmetric temperature spot or the nonlinear dependence on spot temperature found in the experiments.

D. Experimental tests

We have argued that every passage of the warm spot results in a liquid step Δx opposite to the spot movement direction. The pump speed is therefore expected to increase in a linear fashion with repetition frequency of the laser spot as given by Eq. (8). This behavior was predicted by the

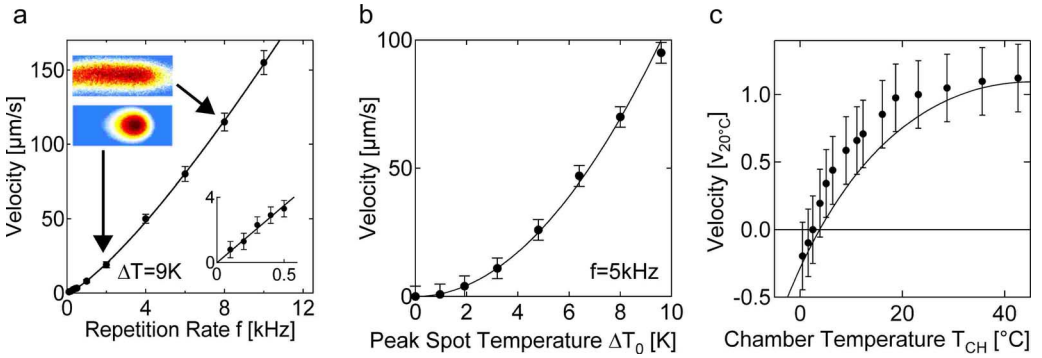

FIG. 4. (Color online) Thermoviscous pumping can be described by the analytical model of Eq. (8). (a) The pump velocity is a linear function of the repetition rate for $f<1$ kHz when the spot geometry remains Gaussian (inset: temperature image). At faster rates, the warm spot becomes elongated due to the finite thermal equilibration time of cooling. Accordingly, the pump velocity is enhanced beyond the linear prediction as the spot width b increases from 10 to 20 μm in the 5 μm thin fluid film. The solid line predicts the pump velocities based on extrapolated temperature profiles for each repetition rate f. (b) The pump velocity rises with the square of the spot temperature, confirming the linear dependence on both the thermal expansion and the temperature dependence of the viscosity. Pump velocities are predicted by Eq. (8) without fitting parameters at a spot width $b=25$ μm. (c) By changing the overall chamber temperature T_{ch}, we can probe the dependence on $\alpha(T_{ch})$ and $\beta(T_{ch})$. For $T_{CH}<4$ °C, the water contracts upon heating. As expected from Eq. (8), pump velocity reverses its direction (solid line). In all plots, error bars show standard errors (s.e.m.) from particle tracking.

theory and verified by measurements in the low frequency regime $f \ll 1$ kHz as shown in the inset of Fig. 4(a). The repetition rate f in this experiment was adjusted by scanning the laser with increased velocity along a fixed circular pump geometry. For slow frequencies, the spot temperature distribution is not deformed from its Gaussian shape. A further increase in the spot velocity results in a considerable elongated temperature spot geometry along the pump direction which increased the pump speed beyond the linear estimate using constant spot width b [Fig. 4(a)]. Examples of spot geometries as measured with stroboscopic temperature imaging are given as color coded insets. Interestingly, the nonlinear pump velocity could still be described when the elongated temperature spot geometry was taken into account with a spatial integral of Eq. (7) for each repetition rate [Fig. 4(a), solid line].

Additional experiments further support the model and the used approximations. The analytical theory predicts a linear response of the pump velocity to both the thermal expansion $\alpha\Delta T_0$ and the change in the temperature dependent viscosity $\beta\Delta T_0$ for a similar shape of the temperature spot. If the spot temperature is increased by enhanced laser power, the pump velocity increases proportionally to ΔT_0^2. The experiments fully confirmed this parabolic dependence as shown in Fig. 4(b). The solid line results from Eq. (8) without additional fitting parameters and matches the experimental data within the error bars.

We test the proportionality to the parameters α and β by changing the ambient temperature T_{ch} of the chamber. In Fig. 4(c) we changed T_{ch} by cooling the microscope stage with an external heat bath. The experiments reveal a reversal of the pump direction at fluid temperatures below 4 °C. We attribute this reversal to the sign change of the volume expansion coefficient α. The theoretical expectation of Eq. (8) again fits the experimental pump velocities as plotted against the fluid temperature within the experimental errors.

E. Pump path width

We explored the possible spatial resolution and limitations for the applied pattern shape in a number of experiments which are documented in Figs. 5 and 6. We did not derive an analytical theory for the pump velocity dependence perpendicular to the fluid flow. However, one might expect that also in this direction the velocity profile falls off with the square of the spot temperature. To test this, we independently measured the temperature profile with fluorescence and tracked the particle velocity profiles in a straight flow geometry, shown in Fig. 5(a). We found that the fluid velocity is indeed not proportional to a linear temperature profile (dashed line) but to the significantly sharper square of the temperature focus (solid line). Both profiles are compared with the measured velocities from particle tracking of 1 μm particles shown as black dots. We consequently find that the resolution of pumping is enhanced by a factor of $\sqrt{2}$ due to the quadratic nature of the nonlinear pumping mechanism.

By reducing the focus size, flow patterns on the micrometer scale could be realized. We pumped water along the letters "nim" in a 3 μm thin chamber. The paths have a minimal distance of 8 μm as shown in Fig 5(b). The movement

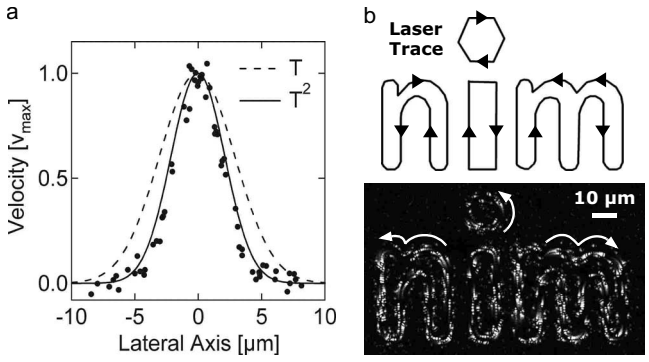

FIG. 5. Controlling fluid flow at optical resolution. (a) The measured lateral temperature of the spot (dashed line) is compared to experimental pump velocities (dots). The width of the pump path follows the significantly sharper ΔT^2-profile (solid line). As result, the resolution of the fluid flow is enhanced by a factor of $\sqrt{2}$. (b) To demonstrate the fluid flow resolution, the laser was moved along the pattern "nim" with minimal path separations of 8 μm. The resulting flow has a resolution of 1.5 μm (standard deviation) at a chamber thickness of 3 μm. As seen, the flow paths do not interfere. The corresponding movie can be found in the supplementary materials section.

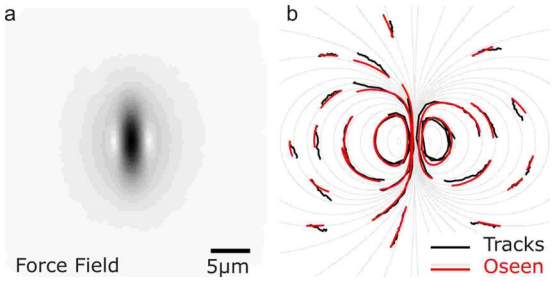

FIG. 6. (Color online) Pumping a finite-sized Oseen tensor. (a) The focus is moved along a short path by a short deflection and a subsequent flyback with the laser switched off, both implemented by the acousto-optical deflector. (b) The generated flow field is inferred from particle tracking of 1 μm beads shown for a recording interval of 7 s (black). Their movement is well described by a finite-sized Oseen tensor (red and gray, see supplementary material). Any solution of the laminar, two-dimensional Navier–Stokes equation can be generated by the superposition of Oseen tensors. Individual pump patterns can be superposed by the laser scanning. As result we can generate arbitrary solutions of the laminar two-dimensional Navier–Stokes equation on the tens of micrometer scale.

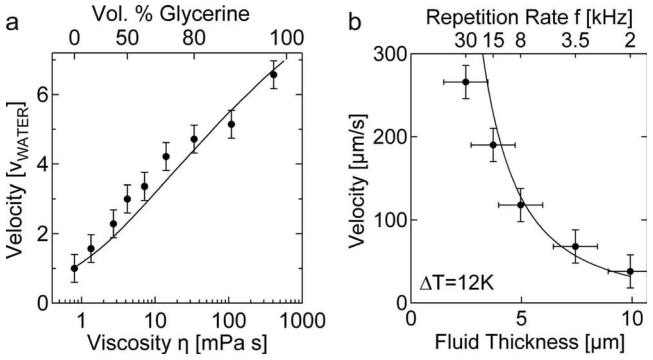

FIG. 7. Methods to enhance the pump speed. (a) Viscous fluids are pumped equally well, shown for viscous water-glycerol mixtures. The increased pump speed is the result of an increased β at a rising glycerol concentration. The parallel increase in viscosity does not quench pump velocities. (b) Pump speeds also increase for thinner chambers since the repetition rate f can be enhanced quadratically with decreasing chamber thickness.

of 500 nm tracer particles are shown by the superposition of subsequent frames. We find a flow width with a standard deviation of 1.5 μm. Note that the nearby pump paths showed no interference. It appears that further downscaling of the heating source and the chamber thickness will allow to pump fluids even well below micrometer resolution. The strength of thermal expansion will still allow to drive the fluid flow and as discussed later, pumping even becomes faster in thinner chambers due to the enhanced thermal relaxation speed.

F. Pumping an Oseen tensor

We asked if it is possible to drive any solution of the two-dimensional Navier–Stokes equation in the limit of low Reynolds numbers with micrometer resolution. To test this assertion, we benchmarked the fluid flow with a finite-sized Oseen tensor. An Oseen tensor describes the fluid flow generated from a delta-shaped application of force to the fluid. By showing that we can generate a highly localized flow in the shape of the Oseen tensor, all possible solutions of the two-dimensional Navier–Stokes equation in the limit of laminar flow can be obtained with similar resolution by superposition of the laser scanning patterns. This demonstrates that the presented light driven pump can drive two-dimensional fluids with unprecedented flexibility on the micrometer scale.

We created a finite-size Oseen flow by moving the warm spot unidirectionally over a short distance. The laser is switched off during the flyback motion. We visualized the movement of the fluid with tracer particles and compared their tracks to a finite element calculation of a finite-sized Oseen tensor (Fig. 6). As shown, a Gaussian force field with the standard deviations of 2.6 μm along and 1.2 μm perpendicular to the vertical pump direction [Fig. 6(a)] fitted the measured flow [Fig. 6(b)]. Since scan patterns can be combined, we can generate almost arbitrary solutions of the two-dimensional Navier–Stokes equation with a similar resolution (see supplementary movies).[20] No other method that we know of can drive such arbitrary solutions of the Navier–Stokes equation.

G. Toward light driven nanofluidics

Highly viscous fluids can be pumped equally well and in many cases yield a considerably faster pump speed. For example, by adding glycerol to water, the pump speed increases 7-fold at a constant spot temperature despite a 500-fold increase in the viscosity [Fig. 7(a)]. This is the result of the increase in $|\alpha \cdot \beta|$ as predicted by Eq. (8), shown as solid line. Since thermoviscous pumping in 10 μm thin water is four to five orders of magnitude away from the pressure limitation of typical microfluidic chambers, pumping liquids of even higher viscosities or in thinner chambers is possible without reduced pump velocity. Due to the local pumping mechanism, problems from large viscosity or thin chambers are much less an issue for the described light driven flow as compared to classical pressure driven microfluidics.

The thermal relaxation time τ of the cooling is provided by the chamber walls and significantly depends on the chamber height. In sufficiently thin chambers, the heat flow is predominantly perpendicular to the fluid film and the temperature dynamics can be approximated with a single exponential decay of one-dimensional diffusion with a time constant of $\tau = d^2/(\pi^2 \kappa)$ where d denotes the fluid thickness and κ the thermal diffusivity. Therefore, the warm spot retains its circular shape if the repetition frequency is scaled according to $f \propto 1/d^2$. As a consequence, the pump speed becomes quadratically faster for thinner chambers. This dependence was tested experimentally in Fig. 7(b). We varied the chamber thickness and adjusted the repetition frequency accordingly. The temperature profile of the spot remained constant with $b = 19$ μm. This was checked independently with fluorescence imaging of the spot temperature (not shown). The small deviations for thinner chambers probably can be assigned to speed limitations of the used acousto-optical laser deflector. As estimated before, pressure should not limit pumping fluids at the nanoscale, even for fluids with increased viscosity. In the experiment, the decreased light absorption by thinner fluid films was compensated by increased

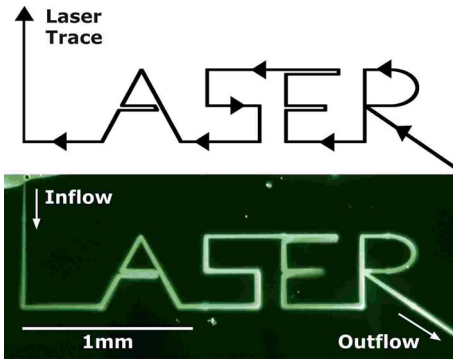

FIG. 8. (Color online) Millimeter-scale unidirectional flow of beads with 20 nm diameter along the letters "LASER." The laser focus guides the fluid with the beads through a low melting agarose gel from an aqueous reservoir on the top left through a gel and back into the aqueous reservoir on the right side of the image.

laser power. The latter poses no fundamental limitation since the light can be alternatively absorbed by nanoscale metal films on the chamber walls.

H. Light driven microfluidics in 2D fluid films

While the dynamic control of fluid flow on the micrometer scale is an interesting subject by itself, the capability to transport dissolved molecules is crucial for microfluidic applications. Traditional microfluidics use micromachined channels to hinder diffusion of molecules perpendicular to the pump direction. While our technique can also pump along such optically transparent channels, we aim at more flexible and previously impossible settings. For example, the method allows the usage of unstructured and disposable chambers. In the following, microfluidic experiments were performed by sandwiching microliter-scale fluid droplets between two microscope cover slips. We demonstrate the millimeter-scale transport of nanoparticles and the aliquotation and mixing for short DNA.

First, we pumped fast diffusing 20 nm fluorescent beads across several millimeters in a gel along the letters "LASER" (Fig. 8). The initial condition was prepared by sandwiching two droplets between glass slides: one drop contained the beads in water and the other drop initially warm low melting temperature agarose gel. At the interface, the beads were pumped into the gel which was liquefied by the heating and replaced by the bead-water solution. The gel effectively reduced lateral diffusion and allowed the microscale definition of pump channels (Fig. 8). For the future, besides using gels to hinder diffusion, the optical creation of pump paths by melting thin ice sheets appears to be a useful approach.

I. Light driven aliquotation of DNA

To show how light driven pumping can be used in microfluidic applications, we demonstrate a purely light driven fluid mixer for small biomolecules (Fig. 9). Two geometries are presented. In the first geometry, the fluorescent molecules are pumped into three pockets of different areas and mixed with the surrounding dark liquid with volume ratios of 4:1, 1:1, and 1:4 [Fig. 9(a)]. Secondly, a geometry for faster mixing into a larger number of pockets is shown in Fig. 9(b).

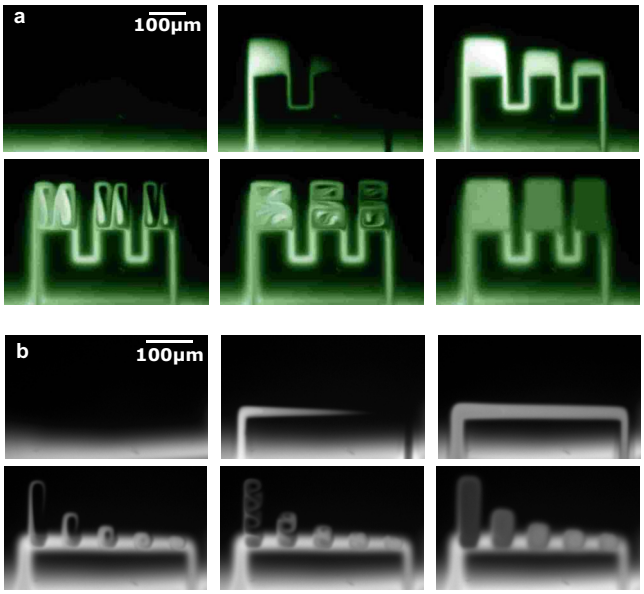

FIG. 9. (Color online) Light driven mixing of DNA hairpins in dynamically created gel pockets. (a) Two liquids are mixed with different ratios simultaneously. Fluorescein-Dextran (MW 40.000) is pumped from a liquid boundary (bottom) into three chambers of different size. It is mixed with the dye-free liquid (top) in equally sized areas at volume mixing ratios of 4:1, 1:1, and 1:4. The mixing is performed all optically without any microfluidic walls and without any contact to the liquid other than the unstructured cover slips that border the fluid film. At the used repetition frequency $f=120$ Hz the mixing sequence took 280 s. (b) A 40-base DNA Hairpin (bottom, bright) is mixed with target DNA (top, dark) at mixing ratios 1:8, 1:4, 1:3, 1:2, and 1:1. The mixing is provided from a single channel into pockets of variable size. The overall mixing time is 170 s at $f=140$ Hz. The corresponding movies are supplied as supplementary material.

From an initial channel along a straight line, a 40 base DNA hairpin (molecular beacon) is mixed with target DNA with the ratios 1:8, 1:4, 1:3, 1:2, and 1:1. Depending on the target DNA concentration, the hairpin opens up and changes the fluorescence signal. The time required for the latter mixing protocol is 170 s. In the next paragraph we present a tailored chamber material which enhances the protocol speed by more than a factor of 10.

J. Enhanced speed using light absorption layer

The repetition frequency of $f=100$ Hz used in the mixing experiments of Fig. 9 was very moderate and could be raised at least 20-fold to 2 kHz which would increase the pump speed considerably as seen in Fig. 2(b). To achieve this, we switched to a more elaborate chamber wall material with enhanced thermal conduction and a light absorbing layer at the solid-water interface. We used a 40 nm thin CrNi film on a double-sided polished silicon wafer to absorb 30% of the laser light. The enhanced power deposition is used to achieve faster repetition rates at the same spot temperatures. The resulting aliquotation and mixing experiment is shown in Fig. 10. A dilution series of biomolecules is achieved within 15 s. As before, aliquots of one liquid were first created by pumping defined volumes across a gel interface. Three chambers in the gel with different volumes (65, 40, and 20 pl) were formed. In the second step the fluid was mixed with the surrounding fluid to obtain equal volumes of 80 pl. Efficient mixing was accomplished by repeatedly

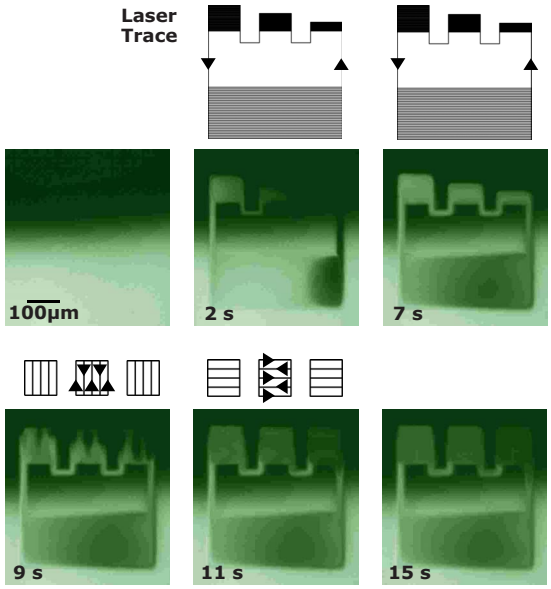

FIG. 10. (Color online) Fast light driven creation of a dilution series. Biomolecules are aliquoted and mixed from an interface of two neighboring gels. First, three volumes of 65, 40, and 20 pl are created. In a second step the fluid is mixed by repeatedly pumping rectangular ring flows with perpendicular orientation. The result is a dilution series with volume ratios of 4:1, 1:1, and 1:4 in equal volumes. Due to the light absorbing chamber wall composite material, protocol time drops to 15 s. The corresponding movie can be found in the supplementary materials section.

pumping rectangular ring flows with perpendicular orientation (see inset in Fig. 10). The resulting dilution series had final volume ratios of 4:1, 1:1, and 1:4. This example demonstrates the speed and flexibility by applying different pump patterns over time.

K. Possibilities and limitations

Light driven pumping reaches velocities of up to 150 μm/s for moderate heating. In comparison, pressure driven microfluidics typically operate with tenfold faster flow speeds. However, these fast speeds need millimeter-sized interfacial connections to outside pumps. The presented method allows for highly localized fluid actuation. We imagine to apply fluid volumes locally, for example, by spotting droplets onto inlets in close proximity of the gel. It is also possible to place ice pads near a two-dimensional ice sheet in which the light driven pumping would be performed. We want to note that adding glass formers to the solution increases the pump speed by raising the parameters α and β. For example, the glycerine-water mixture was pumped up to sixfold faster at equal spot temperature as shown in Fig. 7(a). More specialized glass formers with stronger effects are likely to exist and could be used to increase the speed of pumping considerably.

As the pump pattern is programmable in real time, pumping can be adapted to varying geometries. For example, living cells produce minute amounts of intracellular signals. Thermoviscous pumping could selectively enhance the transport of these signalling molecules from one cell to another with pump paths that are adapted in real time to the positions of the cells. Also, the pumping mechanism is not limited to be driven by optical means. Heating from a wide variety of other sources such as electrical currents will equally pump fluids, extending previously explored electrical movement strategies using electrophoresis[23] or surface acoustic waves.[24] However, the physical isolation between the light source used as fluid actuator and the chamber comprising the fluid will allow to pump inside complex chambers hosting extreme fluid pressures or temperatures. The temperature gradients that are imposed by the pump mechanism can be combined with thermophoretic effects which move molecules along a temperature gradient.[19,25] For example, thermophoretic traps for biomolecules simulating hydrothermal conditions[26,27] should become feasible at much smaller length scales, enabling fast equilibration times. Finally we want to note that pumping in three dimensions should be achievable with highly focused heating of the fluid or even two-photon heating using adequate dyes.

IV. CONCLUSIONS

We found a physical mechanism to pump liquids along arbitrary geometries with a laser scanning microscope. The fluid flow follows the movement of a warm heating spot that is created optically by light absorption. Arbitrary flow patterns can be realized with path widths close to the optical resolution. The mechanism is based on the thermal expansion in a viscosity gradient in the vicinity of a moving warm spot. This optical pumping has the potential to complement microfluidic designs with valveless, contactless, and pumpless flow at the micrometer and submicrometer scales. Supplementary information accompanies the paper.

ACKNOWLEDGMENTS

We thank Joseph Egger for help in solving the fluid dynamics, Jonas A. Kraus and Thomas Franosch for discussions, Philipp Baaske and Ingmar Schön for reading the manuscript, Klaus Stierstadt for comments, Stefan Duhr and Ingmar Schön for assistance, and Hermann Gaub for hosting our Emmy-Noether Group. This work was funded by the Emmy Noether Program of the Deutsche Forschungsgemeinschaft (DFG) and supported by the Center for Nanoscience Munich (CENS) and the Nanosystems Initiative Munich (nim).

[1] D. J. Harrison, K. Fluri, K. Seiler, Z. Fan, C. S. Effenhauser, and A. Manz, Science **261**, 895 (1993).
[2] B. H. Weigl, Science **283**, 346 (1999).
[3] T. Thorsen, S. J. Maerkl, and S. R. Quake, Science **298**, 580 (2002).
[4] J. Tian, H. Gong, N. Sheng, X. Zhou, E. Gulari, X. Gao, and G. Church, Nature (London) **432**, 1050 (2004).
[5] T. M. Squires and S. R. Quake, Rev. Mod. Phys. **77**, 977 (2005).
[6] R. B. M. Schasfoort, S. Schlautmann, J. Hendrikse, and A. van den Berg, Science **286**, 942 (1999).
[7] B. Zhao, J. S. Moore, and D. J. Beebe, Science **291**, 1023 (2001).
[8] B. S. Gallardo, V. K. Gupta, F. D. Eagerton, L. I. Jong, V. S. Craig, R. R. Shah, and N. L. Abbott, Science **283**, 57 (1999).
[9] M. G. Pollack, R. B. Fair, and A. D. Shenderov, Appl. Phys. Lett. **77**, 1725 (2000).
[10] D. Psaltis, S. R. Quake, and C. Yang, Nature (London) **442**, 381 (2006).
[11] P. Y. Chiou, Z. Chang, and M. C. Wu, Proceedings of the Micro Electro Mechanical Systems, 2003 (unpublished), p. 355.
[12] P. Y. Chiou, A. T. Ohta, and M. C. Wu, Proc. SPIE **5514**, 73 (2004).
[13] K. Ladavac and D. Grier, Opt. Express **12**, 1144 (2004).
[14] A. A. Darhuber, J. M. Davis, S. M. Troian, and W. W. Reisner, Phys.

Fluids **15**, 1295 (2003).
[15]A. Wixforth, C. Strobl, C. Gauer, A. Toegl, J. Scriba, and Z. v. Guttenberg, Anal. Bioanal. Chem. **379**, 982 (2004).
[16]A. Ashkin, Phys. Rev. Lett. **24**, 156 (1970).
[17]A. Ashkin, Proc. Natl. Acad. Sci. U.S.A. **94**, 4853 (1997).
[18]S. M. Block, L. S. B. Goldstein, and B. J. Schnapp, Nature (London) **348**, 348 (1990).
[19]S. Duhr and D. Braun, Proc. Natl. Acad. Sci. U.S.A. **103**, 19678 (2006).
[20]See Document No. E-JAPIAU-104-001823 for supplementary movies and Femlab 3.1 simulation files. For more information on EPAPS, see http://www.aip.org/pubservs/epaps.html.
[21]E. Yariv and H. Brenner, Phys. Fluids **16**, L95 (2004).
[22]F. M. Weinert, J. A. Kraus, T. Franosch, and D. Braun, Phys. Rev. Lett.**100**, 164501 (2008).
[23]A. Ros, R. Eichhorn, J. Regtmeier, T. T. Duong, P. Reimann, and D. Anselmetti, Nature (London) **436**, 928 (2005).
[24]Z. Guttenberg, H. Müller, H. Habermüller, A. Geisbauer, J. Pipper, J. Felbel, M. Kielpinski, J. Scriba, and A. Wixforth, Lab Chip **5**, 308 (2005).
[25]C. Ludwig, Sitzungsber. Akad. Wiss. Wien, Math.-Naturwiss. Kl. **20**, 539 (1856).
[26]P. Baaske, F. M. Weinert, S. Duhr,K. H. Lemke,M. J. Russell, and D. Braun, Proc. Natl. Acad. Sci. U.S.A. **104**, 9346 (2007).
[27]D. Braun and A. Libchaber, Phys. Rev. Lett. **89**, 188103 (2002).

Light driven microflow in ice

Franz M. Weinert, Max Wühr, and Dieter Braun[a)]
Department of Physics, Systems Biophysics, Center for Nanoscience, Ludwig Maximilians Universität München, Amalienstr. 54, 80799 München, Germany

(Received 4 December 2008; accepted 14 February 2009; published online 16 March 2009)

We optically pump water through micrometer thin ice sheets. The ice is locally moved with speeds exceeding 5 cm/s by repetitive melting and freezing, which occurs around a moving infrared laser spot. The minimal channel width is 10 μm. The diffusion limitation of ice allows for fast spatial biomolecule control without predefined channels, valves, or external pumps. Dye molecules are pumped across an ice-ice interface, showing the possibility of microfluidic applications. Pumping in ice is three orders of magnitude faster than the previously shown for thermoviscous pumping in water. © *2009 American Institute of Physics*. [DOI: 10.1063/1.3097206]

The ability to remotely control matter with light has unique advantages. Optical tweezers for example can remotely move microscale objects[1] and have allowed many applications in the life science.[2] Likewise, photolithography allows patterning of materials without physical contact at an ever increasing level of miniaturization.[3] A method, which can manipulate not only solids but also fluids by light is equally desirable. In the past, we have pursued nonlinear effects in thermal expansion to optothermally pump fluids.[4,5] Here we applied a similar principle to ice and found that the melting transition dynamics enhance the pump speed significantly i.e., from 50 μm/s to 5 cm/s.

Classical microfluidics provides the highly complex manipulation of small volumes[6–10] in life sciences by pumping fluids through defined channel networks.[11–15] However, a considerably complex external interfacing of the microchannels with pumps and inlets is required. Recently a method to create reconfigurable microchannels in ice by using an IR laser was shown.[16] Our work extends the approach by showing that a moving laser spot in ice yields high pump velocities and has the potential to complement channel-based microfluidics in optically driven platforms.

We create a moving spot of raised temperature by scanning a focused infrared laser through a micrometer thin ice sheet [Fig. 1(a)]. The ice melts at the laser spot and freezes again behind it. The result is a fluid flow in the molten ice in the direction of the moving spot. Since the thermal relaxation time is below milliseconds in microscale fluid or ice films, the laser spot movement can be repeated near the kilohertz regime. As a result, pump velocities of 50 mm/s can be reached along freely defined patterns at the micrometer scale. As an example, Fig. 1(b) demonstrates fluid flow along the pattern "nim."

A chamber with a 3 μm thin fluid layer is sandwiched between a bottom, double-polished silicon wafer, which is cooled by a microscope stage below 0 °C and a top glass window [Fig. 1(c)]. Imaging with a fluorescence microscope (Axiotech Vario, Zeiss) is provided from the top by a charge coupled device camera (Luca S DL-658M, Andor) and a 20× objective (UPlanSApo $NA=0.75$, Olympus), illuminated with either a xenon lamp (HXP 120, Zeiss) or a light-emitting diode (LED) (LXHL-LD3C, Luxeon). The wavelength of the heating laser (TLR-10–1940, IPG Photonics) is 1940 nm where water absorbs with an attenuation length of $a_{\text{water}}=74$ μm and ice with $a_{\text{ice}}=7$ μm. The total absorbed power ranged between 0.04–0.08 W for water and 0.7–1.3 W for ice. The laser beam is scanned from below the chamber with a galvanometer mirror pair (6200-XY, Cambridge Technology) and focused with a lens ($f=15$ mm, LA1540-C, Thorlabs) through the silicon slide, which is transparent for the used wavelength.

Consider a spot of enhanced temperature moving through a thin ice sheet [Fig. 1(a)]. The ice thaws at the front of the spot and freezes in its wake. The density change during the phase transition induces divergent flows due to mass conservation,[17] with a sink ($\text{div}\,\boldsymbol{v}<0$) at the front and a source ($\text{div}\,\boldsymbol{v}<0$) at the back. The solid ice boundaries confine the liquid flow such that movement is from the back of the molten spot to its front. We assume a parabolic flow

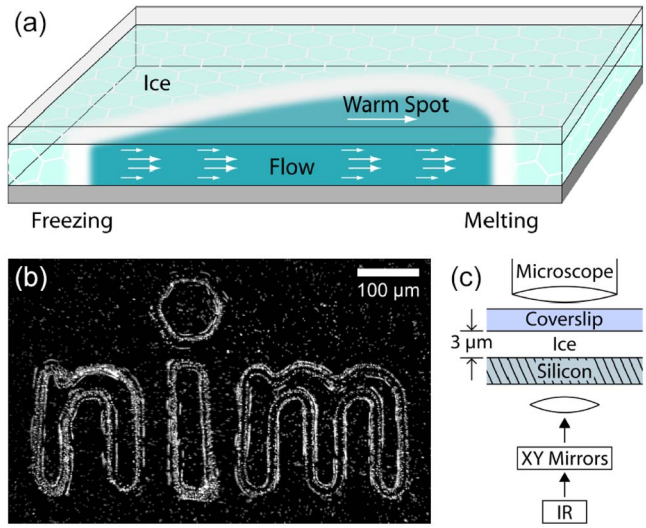

FIG. 1. (Color online) (a) An optically created temperature spot is moved to the right in a sheet of ice. The ice melts in front of the spot (right) and freezes behind it (left) and moves the fluid due to the difference in specific volume. (b) Pumping ice is possible along freely defined patterns such as the letters "nim." The heating laser spot traces the letters nim at 10 Hz. The temporarily molten channels are 25 μm wide and 3 μm thick. We visualize the flow by overlaying differences of successive pictures of fluorescent 1 μm polystyrene spheres, which are suspended in the ice. (c) The laser spot is focused from below and moved with galvanometric mirrors.

[a)]Electronic addresses: braun@lmu.de and dieter.braun@physik.lmu.de.

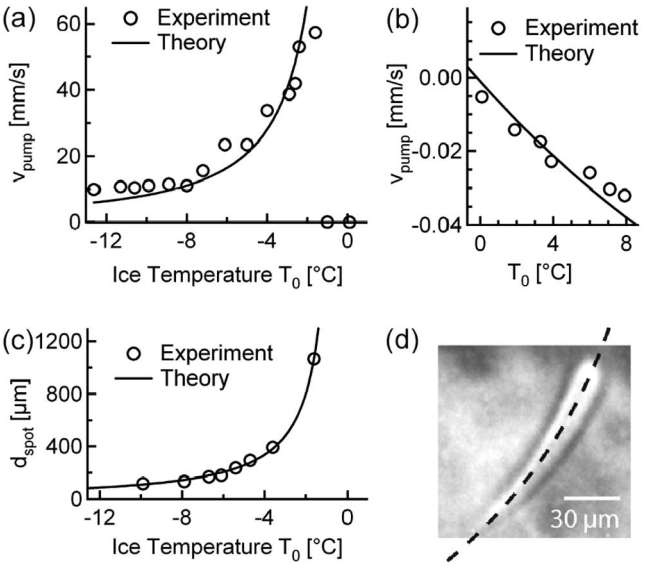

FIG. 2. (a) Pump velocities depend on the ice temperature T_0 (open circles). The theory of Eq. (3) predicts the pump velocity. (b) When the fluid does not freeze along the channel, the residual negative pump velocities can be described by the theory of thermoviscous flow (Ref. 5). (c) The length of the thawed spot becomes more elongated for higher T_0. (d) Stroboscopic image of the molten spot along a circular path, shown by the broken line.

profile perpendicular to the glass/silicon boundaries with $v_{avg}=2/3v_{water}$, where v_{water} is the peak velocity in the center of the fluid sheet. The continuity equation $\dot{\rho}+\mathrm{div}\,\mathbf{j}=0$ at the water-ice boundary is given by

$$\frac{\rho_{water}-\rho_{ice}}{\Delta t_M}-\frac{2}{3}\frac{v_{water}\rho_{water}}{\Delta x_M}=0. \tag{1}$$

With the velocity of the water-ice boundary $v_{spot}=\Delta x_M/\Delta t_M$ we find

$$v_{water}=\frac{3}{2}\frac{\rho_{water}-\rho_{ice}}{\rho_{water}}v_{spot}. \tag{2}$$

The water is molten during the passage of the spot for the time interval $\Delta t=d_{spot}/v_{spot}$, where d_{spot} is the end to end distance of the molten area and moves by the distance $\Delta x=v_{water}\Delta t$. If the spot movement is repeated with frequency f, we expect a pump velocity

$$v_{pump}=\Delta x f=\frac{3}{2}\frac{\rho_{water}-\rho_{ice}}{\rho_{water}}d_{spot}f. \tag{3}$$

It is possible to image the length of the moving spot d_{spot} by stroboscopic white light imaging. The on times of the LED of 20 μs are considerably faster than the typical spot passage time $\tau=d_{spot}/v_{spot}=0.8$ ms. A typical image of the drop-shaped molten area with $d_{spot}=120$ μm is shown in Fig. 2(d). Pumping is performed with a repetition rate of $f=650$ Hz and a chamber temperature of $T_0=-9.9$ °C. With densities $\rho_{water}=1000$ kg/m^3 and $\rho_{ice}=917$ kg/m^3 we expect $v_{pump}=9.5$ mm/s. Experimentally, we find 11 mm/s, which is inferred from tracer particles with 1 μm diameter, in agreement with the theoretical expectations.

The length of the molten spot depends on the temperature of the ice sheet [Fig. 2(c)]. At low ice temperatures, only a short spot is molten. At higher ice temperatures, the molten spot can reach lengths beyond 500 μm/s with the pump velocity exceeding 50 mm/s [Fig. 2(a)]. We fit the spot length phenomenologically with $d_{spot}=a_0(a_1-T)^{a_2}$ and inserted this result into Eq. (3), shown as a solid line in Fig. 2(a). Theory and experiment match quantitatively.

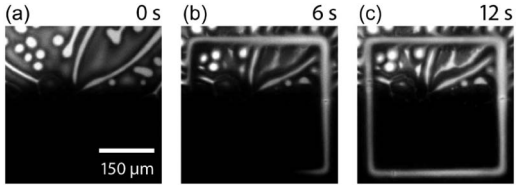

FIG. 3. Optically pumping across an ice-ice interface. [(a)–(c)] The fluorescent dye Cy5 was pumped across an ice-ice interface. The ice-ice interface was created by sandwiching 0.6 μl distilled water to a thickness of 5 μm. After cooling to −12 °C a droplet of 180 μM Cy5 in 1×SSC (150 mM NaCl in 15 mM sodium citrate) is pipetted at the chamber edge and pulled inside by capillary forces. The Cy5 solution freezes after making contact with the ice sheet and forms an interface with the frozen water. The inhomogeneous structure results from the freezing of the dye solution on a slow time scale.

For further increased chamber temperatures, the front of the thawed spot catches up with the back of the previous heating cycle. The fluid flow is not confined solely toward the front in this case and pumping stalls. A residual negative pump velocity is attributed to thermoviscous flow in liquids[4,5] and matches theoretical predictions with a temperature spot width of $b=60$ μm and a temperature raise of $\Delta T=15$ K given by

$$v_{pump}^{(fluid)}=-\frac{3\sqrt{\pi}}{4}f\alpha\beta b\Delta T^2, \tag{4}$$

using the thermal expansion coefficient α and temperature dependent viscosity β of water [Fig. 2(b)].[5]

To demonstrate microfluidic applications, we placed two frozen solution next to one another [Fig. 3(a)]. The ice at the top contains the dye Cy5 ($M_W\approx 500$ g/mol) and shows an inhomogeneous structure, probably due to grain boundaries of the slow freezing process. We pump the dye across the ice-ice interface along a rectangular pattern with repetition frequency of 50 Hz [Figs. 3(a)–3(c); $t=0,6,12$ s]. A thin air film is likely to exist between the ice-ice interface and reduces the pump velocity (see movie, supplementary material).[18] The Cy5 dye is pumped along 15 μm wide channels in the bottom ice sheet. The fast freezing process, which is on the millisecond timescale, yields homogeneous Cy5 concentrations along the channel.

The pump paths can be defined within optical resolution and can be changed dynamically within tens of milliseconds. This can be used to implement switches and valves. Ice allows the deposition of substances at any place without loosing the specimen by diffusion, while speeds are in the centimeter per second range even for small temperature steps across the melting point. We expect that the repetitive melting-freezing cycles are not very stressful to biomolecules since ice, if cooled on the millisecond time scale, remains amorphous and without gain boundaries.

The creation of vapor bubbles imposes restrictions on the pump mechanism. The density shift in the initial thawing can reduce the pressure in the chamber below the triple point of water ($p_{triple}\approx 6$ mbar) and introduce water vapor bubbles, which typically do not dissolve back into the water or ice and hinder pumping. To reduce their generation, elastic chamber boundaries could be used.

To conclude, we expanded the thermoviscuous paradigm of light driven microfluidics by switching from fluid to ice sheets. In ice the pump speed was in the cm/s regime without excessive heating. The fluid flow was quantitatively explained by a model of directed fluid flow inside a moving thawed area. Laser heating in ice allows for highly flexible fluid flow along optically definable patterns without lateral diffusion of dissolved molecules. We demonstrated the exchange of picoliter volumes across an ice-ice interface. With the results, we envisage complex light driven microfluidics in ice.

We thank Ann Fornof for reading the manuscript. The research was funded by the Emmy Noether program of the Deutsche Forschungsgemeinschaft (DFG), the LMU Innovativ Initiative Functional NanoSystems (FUNS), and the Excellence Cluster NanoSystems Initiative Munich (NIM).

[1]A. Ashkin, Phys. Rev. Lett. **24**, 156 (1970).
[2]D. M. Block, L. S. B. Goldstein, and B. J. Schnapp, Nature (London) **348**, 348 (1990).
[3]P. S. Peercy, Nature (London) **406**, 1023 (2000).
[4]F. M. Weinert, J. A. Kraus, T. Franosch, and D. Braun, Phys. Rev. Lett. **100**, 164501 (2008).
[5]F. M. Weinert and D. Braun, J. Appl. Phys. **104**, 104701 (2008).
[6]R. B. M. Schasfoort, S. Schlautmann, J. Hendrikse, and A. van den Berg, Science **286**, 942 (1999).
[7]J. Tian, H. Gong, N. Sheng, X. Zhou, E. Gulari, X. Gao, and G. Church, Nature (London) **432**, 1050 (2004).
[8]M. A. Burns, B. N. Johnson, S. N. Brahmasandra, K. Handique, J. R. Webster, M. Krishnan, T. S. Sammarco, P. M. Man, D. Jones, D. Heldsinger, C. H. Mastrangelo, and D. T. Burke, Science **282**, 484 (1998).
[9]J. W. Hong, V. Studer, G. Hang, W. French Anderson, and S. R. Quake, Nat. Biotechnol. **22**, 435 (2004).
[10]T. Thorsen, S. J. Maerkl, and S. R. Quake, Science **298**, 580 (2002).
[11]A. Manz, N. Graber, and H. M. Widmer, Sens. Actuators B **1**, 244 (1990).
[12]D. J. Harrison, K. Fluri, K. Seiler, Z. Fan, C. S. Effenhauser, and A. Manz, Science **261**, 895 (1993).
[13]S. C. Jacobson, R. Hergenroder, L. B. Koutny, and J. M. Ramsey, Anal. Chem. **66**, 1114 (1994).
[14]A. T. Woolley and R. A. Mathies, Proc. Natl. Acad. Sci. U.S.A. **91**, 11348 (1994).
[15]T. M. Squires and S. R. Quake, Rev. Mod. Phys. **77**, 977 (2005).
[16]M. Varejka, S. Piletsky, A. Woodman, A. P. F. Turner, 2006 Digest of the LEOS Summer Topical Meetings, 36 (2006).
[17]E. Yariv and H. Brenner, Phys. Fluids **16**, L95 (2004).
[18]See EPAPS Document No. E-APPLAB-94-112910 for a supplementary movie. For more information on EPAPS, see http://www.aip.org/pubservs/epaps.html.

submitted to Science

An Optical Conveyor for Molecules

Franz M. Weinert and Dieter Braun

Systems Biophysics, Center for Nanoscience, Physics Department,

Ludwig Maximilians Universität München, Amalienstr. 54, 80799 München, Germany

E-Mail: braun@lmu.de

Trapping single ions under vacuum allows for ultra precise spectroscopy in atomic physics. The confinement of biological molecules in bulk water is hindered by the lack of comparably strong forces. Molecules have been immobilized to surfaces, however often with detrimental effects on their function. Here, we optically trap molecules by creating the microscale analog of a conveyor belt: a bidirectional flow is combined with a perpendicular thermophoretic molecule drift. Arranged in a toroidal geometry, the conveyor accumulates a hundredfold excess of 5-base DNA within seconds. The mechanism does not require microfluidics, electrodes or surface modifications. The optical conveyor can be used to enhance diffusion-limited surface reactions, redirect cellular signaling, observe individual biomolecules over a prolonged time or approach single molecule chemistry in bulk water.

At small scales, Brownian motion dominates the movement of small bio-molecules, which renders their handling and positioning a difficult task in free solution [1-4]. While the relaxation time scale of mass diffusion on the micrometer scale is on the order of milliseconds, heat diffusion of water is still typically 3 orders of magnitude faster. Our idea here is to use these faster thermal fields to confine and control the position of molecules despite their thermal motion.

Thermophoresis moves molecules by a temperature gradient [5-8]. This effect is weak for

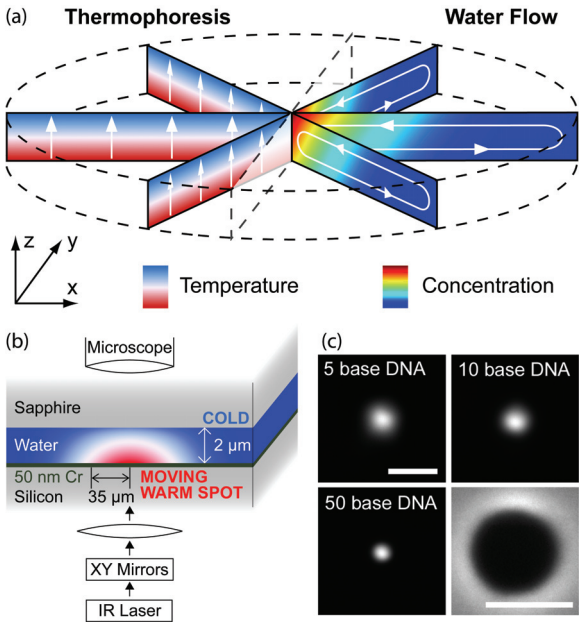

Figure 1: Conveyor trap. (a) Bio-molecules are efficiently accumulated by a combination of a temperature gradient and perpendicular bidirectional flow. Since thermophoresis predominantly locates the molecules at the colder top, the conveyor-like water flow transports the molecules to the center. (b) Both the temperature gradient and the water flow is generated by a spot of enhanced temperature at the bottom, induced by the laser absorption in a thin metal layer. The water flow is the result of the co-axial thermo-viscous pumping in radial direction. (c) Short DNA is trapped from a diameter of 200 µm within 3 seconds. Longer DNA shows a stronger confinement. The single stranded DNA oligos with lengths of 5, 10 and 50 bases are labeled with the fluorescent dye 6-carboxy-2',4,4',5',7,7'-hexachlorofluorescein,succinimidyl ester (HEX) to visualize the concentration. By reversing the fluid flow, the molecules are transported off the conveyor, shown by 1000 base pair DNA stained with the intercalating dye TOTO-1. Scalebars are 100µm.

small molecules, but can be amplified by a bidirectional flow of the fluid perpendicular to the gradient [9,10]. As a result, the molecules are pushed by thermophoresis into one side of the flow and are transported preferentially in one direction. Applied to an axially symmetric geometry, freely diffusing molecules in a fluid film are expected to accumulate to a single spot from all directions (Fig. 1a). In effect, thermophoresis pushes the molecules upward where the water flow shuttles them to the center.

Interestingly, this intricate situation of counterflow and thermal gradient can be created solely by optical means. The thermal gradient is applied by focused infrared absorption of a Cr-film below the water (Fig. 1b). The bidirectional flow is generated by a moving laser spot, based on the recently shown thermo-viscous fluid pump which uses thermal expansion [11] in thermally created viscosity gradients [12,13]. We impose an outward flow near the bottom warm side by a radial laser pattern. The counterflow at the top is ensured by mass conservation [14]. This situation allows the generation of a bidirectional flow in very thin fluid layers of only 2 µm. With a mean temperature difference of 15 K and a diameter of 200 µm this conveyor belt becomes very efficient even for small polymers with lengths down to 1.5 nm. Figure 1c shows single stranded oligonucleotides with lengths of 5, 10 and 50 bases, trapped within 3 seconds. The longer DNA molecules are accumulated to higher concentrations and are more tightly confined in the center, with an $1/e$ decay at a radius of 14 µm. By inverting the flow, the conveyor transports the molecules equally efficiently in outward direction as shown for 1000 base pair DNA in Figure 1c, 4th image.

The physics of the conveyor belt can be simulated using finite elements (Femlab, Comsol). In an axial symmetric geometry we model a bidirectional flow with a maximal speed $v_{max} = 200\,\mu m/s$ [12,13] within the trapping region $r < 100\mu m$. We add the thermophoretic

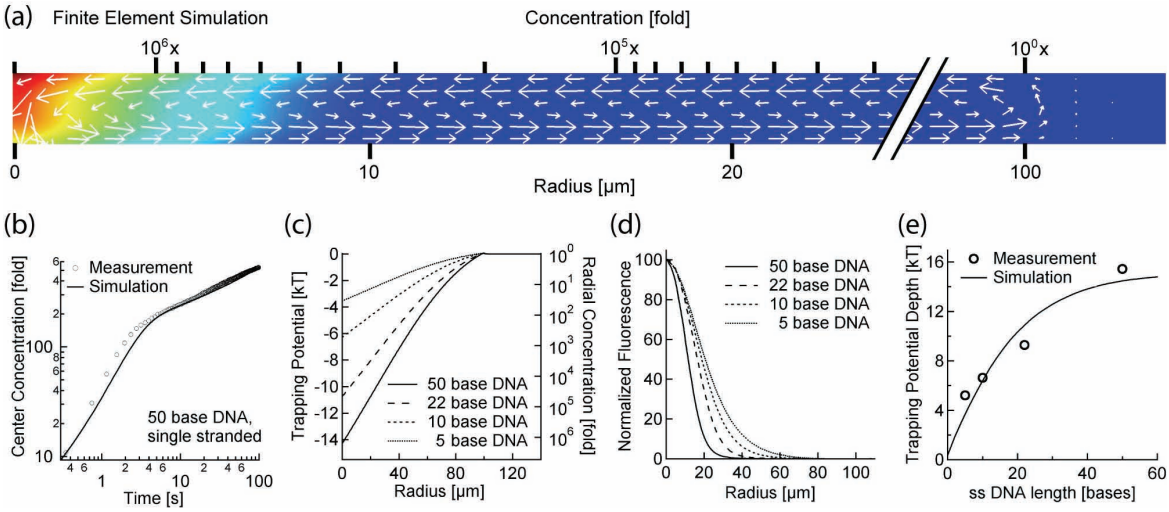

Figure 2: Theory (a) Finite Element Simulation in an axial symmetry confirms the experimental observations and predicts a steady state concentration of 2 million fold for single stranded 50 base DNA. Arrows represent the fluid flow. (b) Molecules in the trap are shuffled to the center within 3 seconds as shown by the time trace of the center concentration with $c \propto t^{1.2}$. *The successively slower concentration increase (* $c \propto t^{0.4}$ *) refers to diffusion into the region of the trap. The simulation (solid line) confirms the experimental behavior (open circles) (c) Radial distribution of the simulated trapping potential for 5, 10, 22 and 50 base DNA. (d) Measured concentration distribution of the conveyor belt. (e) Measured trapping potential depths for the DNA oligomers (open circles) match finite element simulations (solid line).*

drift $v = S_T D \nabla T$ into the diffusion equation with a temperature gradient ∇T matching temperature imaging measurements using the temperature sensitive dye Cy5 [13]. The optical conveyor is simulated for various DNA lengths. Values for the diffusion coefficient D and the Soret coefficient S_T are phenomenologically interpolated to match measurements [14]. Figure 2a shows the simulated concentration for 50 base DNA (color

scale). The simulation predicts a two million fold increase of the center concentration in the steady state.

The trapping mechanism transports the particles into the center within 3 seconds. After that period the relative concentration profile inside the trap is equilibrated. To further increase the absolute value of the center concentration, molecules have to diffuse into the region of the trap. To fill the trap up to its steady state concentration, all molecules within a radius of 10 mm would be needed to enter the trap. Figure 1b shows the measured time trace of the center concentration, compared to the simulation prediction. The two different regimes can be clearly distinguished.

The effective potential depth of the trap can be calculated by assuming a Boltzmann distribution of the DNA molecules in steady state: $U(r) = -kT \ln(c/c_0)$. Figure 2b shows the simulated shapes of the potentials for 50, 22, 10 and 5 base DNA. 5 base DNA is expected to be trapped with a potential of 5 kT referring to a 200-fold accumulation. The linear shaped potential results in an exponential distribution of the concentration over the radius of the trap.

The radial fluorescence intensity of trapped DNA molecules is shown in Figure 2d. The intensities are normalized to the center concentration to compare the accumulation efficiency by the confinement of the distribution for different polymer lengths. The concentration profile differs only in the center of the trap from the expected exponential shape. This is explained by the size of the thermal laser spot with a diameter of $d_{1/e} = 70\,\mu\text{m}$, which is used to drive the bidirectional fluid flow. In the center the laser spot overlaps and cancels out the flow. This lowers the efficiency of the trap in the center region.

The radial distribution of the measured intensity is fitted with an exponential function in the

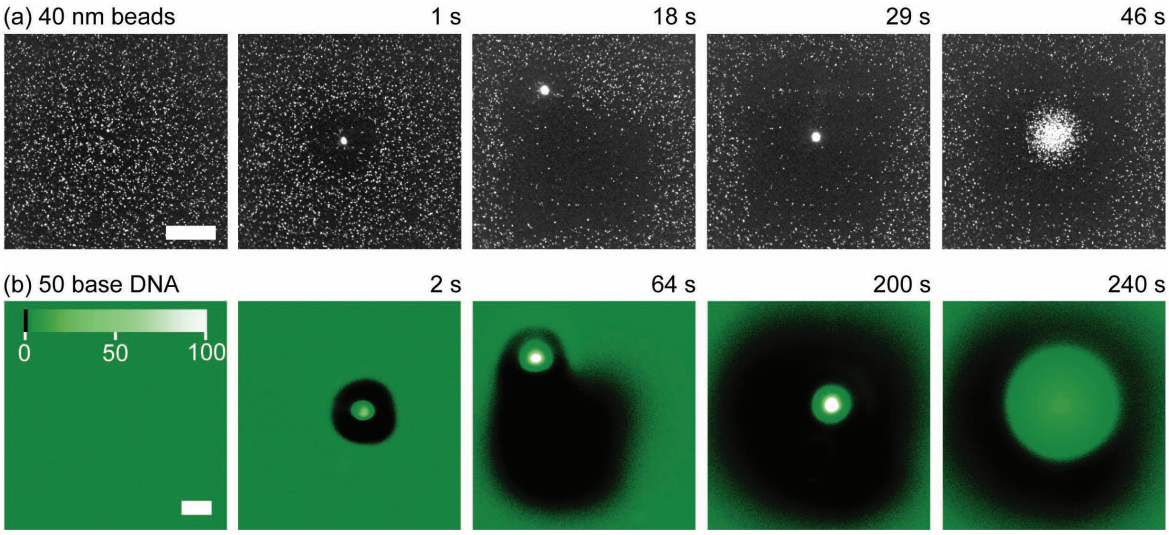

Figure 3: Moving trap. (a) Since the conveyor belt is driven entirely optically, it can be moved arbitrarily through the solution to collect polystyrene beads with a diameter of 40 nm. After the trap has switched off, the particles diffuse freely. (b) The same processing works for single stranded 50 base DNA. The color scale is highly nonlinear to visualize both the high concentration in the trapping center and the comparable low contrast between the outside concentration and the depleted area. The scale bars are 100µm. (See Movie S1, S2)

region beyond $r = 10\mu m$. The trapping potential is obtained from the intensity ratio $U_{TRAP}/kT = -\ln(c/c_0) = -\ln[I_{EXP}(0)/I_{FIT}(100\mu m)]$, where $I_{EXP}(0)$ is the measured fluorescence intensity in the center. We take the extrapolated intensity at the edge of the trapping region $I_{FIT}(100\mu m)$ where the fluorescence measurement is limited by background and the dynamic range of the camera. Figure 2e shows the measured potential depths of the molecule conveyor for single stranded DNA molecules of different lengths (open circles). The simulated data (solid line) describes the experimental results quantitatively.

Since the conveyor belt is driven entirely optically, its position can be changed easily. Instead of waiting for the molecules to diffuse into the trap, they can be collected while passing over them. Figure 3a shows 40 nm polystyrene beads. Comparable to a vacuum cleaner, the radial conveyor belt collects all particles on the trace (Movie S1). A similar protocol traps 50 base DNA molecules (Fig. 3b, Movie S2).

Discussion. The shown opto-fluidic approach allows the assembly of molecules with sizes on the order of a few nanometers from an area of hundreds of micrometers. The principle is related to thermogravitational columns [15,16] which were initially used to separate isotopes in gases [17]. While thermogravitiational columns drive the fluid flow by gravity, we enforce the flow by thermoviscous expansion [12,13]. As a result, we shrink the geometry 100-fold, leading to 10,000-fold faster equilibration times.

To trap smaller molecules such as salts or single fluorescence dyes, one can for example increase the radius of the trap and exponentially raise the steady state molecule concentration in its center. Interestingly, the conveyor becomes more efficient for thinner chambers at a constant radius. For example, a 10-fold thinner chamber (200nm) requires a 10-fold faster convection flow which can be triggered by an equally 10-fold faster scanner [13]. As a result, the trapping potential depth is enhanced 10-fold and the steady state concentration of 5 bases of DNA for example would raise from 200-fold to hypothetical 10^{23}-fold levels. Such conditions would induce a potential for a single fluorescent chromophore with a depth of 8 kT. The pressure difference from the fluid viscosity in a thinner chamber does not deform the chamber and is not limiting the flow speed [13]. The thermal relaxation of such a chamber is on the order of 5 microseconds, still faster than the laser deflection. However faster laser deflections are hard to achieve and

the shown experiments are at the speed limit of acousto-optical deflectors. Therefore, although the optical driving is very attractive due to its flexibility, electrical surface heating might be useful to reach the physical limits of the molecular conveyor.

The presented approach complements and extends previous methods to manipulate and trap small objects. Cohen and Moerner showed a fluorescence feedback trap based on microstructured electrophoresis [3]. This technique proved successful in trapping single molecules down to the size of a few nanometers [18]. For this method, the position of a trapped object has to be obtained in real time. Optical tweezers [1,19-21] have been employed to grab and move objects on the microscale under physiological conditions. However the trapping is restricted to the area of the optical focus at the 1 µm scale and limited to particle sizes not much smaller than 100 nm since the optical power for trapping scales cubically to the reciprocal diameter [19]. In comparison, thermophoresis scales with the particle surface [8].

Conclusions. We show an optical conveyor belt for small molecules in bulk water. Unlabeled molecules with the size of 1.5 nm are transported directionally and accumulated against the Brownian motion to a single spot on the micrometer scale.

Acknowledgments. The authors thank Ann Fornof for reading the manuscript and Ingmar Schön for chip preparations. The work was supported by the Emmy-Noether Program of the Deutsche Forschungsgemeinschaft (DFG), the LMU Innovative Initiative Functional NanoSystems (FUNS) and the Excellence Cluster NanoSystems Initiative Munich (NIM)**.**

References:

1. A. Ashkin, Phys. Rev. Lett. 24, 156 (1970).
2. D. Rudhardt, C. Bechinger and P. Leiderer, Phys. Rev. Lett. 81, 1330 (1998).
3. A. E. Cohen and W. E. Moerner, PNAS 103, 4362 (2006).
4. C. Hertlein, L. Helden, A. Gambassi, S. Dietrich and C. Bechinger, Nature 451, 172 (2008).
5. C. Soret, Arch. Sci. 3, 48 (1879).
6. J. Rauch and W. Köhler, Phys. Rev. Lett. 88, 185901 (2002).
7. H. Brenner, Phys. Rev. E 74,036306 (2006).
8. S. Duhr and D. Braun, PNAS 103, 19678 (2006).
9. D. Braun and A. Libchaber, Phys. Rev. Lett. 89, 188103 (2002).
10. S. Duhr and D. Braun, Phys. Rev. Lett. 97, 038103 (2006).
11. E. Yariv and H. Brenner, Phys. Fluids 16, L95 (2004).
12. F. M. Weinert, J. A. Kraus, T. Franosch, and D. Braun, Phys. Rev. Lett. 100, 164501 (2008).
13. F. M. Weinert and D. Braun, J. Appl. Phys. 104, 104701 (2008).
14. Materials and methods are available as supporting material on Science Online.
15. M. M. Bou-Ali, O. Ecenarro, J. A. Madariaga, C. M. Santamaria and J. J. Valencia, J. Phys.: Condens. Matter 10, 3321 (1998).
16. P. Baaske, F. M. Weinert, S. Duhr, K. H. Lemke, M. J. Russell and D. Braun, PNAS

104, 9346 (2007).

17. K. Clusius and G. Dickel, Naturwissenschaften 26, 546 (1938).

18. A. E. Cohen and W. E. Moerner, Phys. Rev. Lett. 98, 116001 (2007).

19. A. Ashkin, J. M. Dziedzic, J. E. Bjorkholm and S. Chu, Opt. Lett. 11, 288 (1986).

20. A. Ashkin, PNAS 94, 4853 (1997).

21. S. M. Block, L. S. B. Goldstein and B. J. Schnapp, Nature (London) 348, 348 (1990).

Supporting Online Material

www.sciencemag.org

Movies S1, S2

Materials and Methods

Supporting Online Material

Movie S1: Conveyor_40nm.avi

Movie S2: Conveyor_50baseDNA.avi

The movies can be temporarily downloaded from the following hidden directory:

http://www.dieterb.de/dfwe9we8fr9uhefqwef098/

Materials and Methods

Chamber and infrared heating. A two micrometer thin water layer is sandwiched between a bottom silicon wafer and a top sapphire window (thickness 170 µm, diameter 12 mm). The silicon wafer (thickness 0.5 mm, polished on both sides, 1µm SiO_2, MEMC Electronic Materials Inc.) is coated on one side with a 60 nm chromium layer by vacuum evaporation followed by 60nm SiO_2 from plasma-enhanced chemical vapor deposition. An infrared laser beam (RLD-5-1455, IPGLaser, $\lambda = 1455$ nm, 5 W) is deflected by an acousto-optical deflector (AA.DTS.XY.100, Pegasus Optics) and focused from below into the water sheet with a long working distance lens (f = 40 mm, LA1304-C, Thorlabs). The laser passes through the Si and SiO_2 which are transparent to the used wavelength but heats the Cr layer by absorption. The color coded area in Figure 1b shows a finite element simulation of the water temperature in a cross section of the chip. The sapphire window at the top of the fluid sheet has a high thermal conductivity and cools the water to less than 10 % of the temperature at the bottom, resulting in a steep temperature gradient in z-direction.

The solution used in Figure 1, 2 and 3b consists of 1 µM single stranded DNA labeled with

the fluorescent dye HEX at the 5' end (Biomers, Ulm, Germany), dissolved in 10 mM TRIS buffer at pH 10.4. Surface interactions reduce the pH to about 7-8. The diffusion coefficients are measured for 50, 22, 10 and 5 base DNA by evaluating the back diffusion after thermophoretic depletion [8]. For extrapolation, the diffusion coefficients of DNA were fitted phenomenologically with the power function $D = a_1 (L+2)^{-a_2}$, where L is the number of bases, $a_1 = 1020\,\mu\mathrm{m}^2/\mathrm{s}$ and $a_2 = 0.75$. We assume an offset of two bases which have a similar diffusion coefficient than the HEX label. S_T values are expected to scale proportional with $\sqrt{L} + \mathrm{const}$ [8]. The Soret coefficient of 50 base single stranded DNA results in $S_T = 0.006\,\mathrm{K}^{-1} + 0.009\,\mathrm{K}^{-1}\sqrt{L}$, with an offset assigned to the HEX label, measured to $0.006\,\mathrm{K}^{-1}$.

Fluorescence microscope. Imaging is provided with an upright fluorescence microscope (Axiotech Vario, Zeiss) with a CCD camera (Cascade II 512, Photometrics) and a 20x objective (UPlanSApo NA=0.75, Olympus), illuminated with an LED (LXHL-LD3C, Luxeon).

Laser scan pattern. The laser spot is defocussed to a diameter of $d_{1/e} = 70\mu\mathrm{m}$ and scanned in radial direction from a radius of 100 µm towards the center point along 64 different angles with a frequency of 8 kHz per line.